Dusty, Dense, Bright, Dark, Narrow, and Broad: the Rings in our Solar System and a Few of the Things They Can Tell Us

A Dissertation
Presented in Partial Fulfillment of the Requirements for the
Degree of Doctorate of Philosophy
with a
Major in Physics
in the
College of Graduate Studies
University of Idaho
by
Robert O. Chancia

Major Professor: Matthew M. Hedman, Ph.D.
Committee Members: Jason W. Barnes, Ph.D.; Douglas P. Hamilton, Ph.D.;
Francesca Sammarruca, Ph.D.
Department Chair: Ray von Wandruszka, Ph.D.

December 2019

Authorization to Submit Dissertation

This dissertation of Robert O. Chancia, submitted for the degree of Doctorate of Philosophy with a Major in Physics and titled "Dusty, Dense, Bright, Dark, Narrow, and Broad: the Rings in our Solar System and a Few of the Things They Can Tell Us," has been reviewed in final form. Permission, as indicated by the signatures and dates below is now granted to submit final copies for the College of Graduate Studies for approval.

Advisor:	Matthew M. Hedman, Ph.D.	Date
Committee Members:	Jason W. Barnes, Ph.D.	Date
	Douglas P. Hamilton, Ph.D.	Date
	Francesca Sammarruca, Ph.D.	Date
Department Chair:	Ray von Wandruszka, Ph.D.	Date

Abstract

The observations of planetary rings acquired by the *Cassini* and *Voyager* missions and from the Earth have launched large advancements in our knowledge of planetary ring formation, evolution, and dynamics. Today, the study of the ring systems around our giant planets has evolved further into using the rings themselves as a tool to learn about their home planetary systems. In Chapter 2 we use two of the narrow rings of Uranus to probe for unseen nearby small moons who gravitationally interact with the rings and produce wake-like structures. These small moons both provide a possible solution for the confinement of their neighboring narrow rings and may represent a subset of the upper end of the ring particle size distribution. In Chapter 3 we detect the effects of a resonant induced radial mode in the Uranian η ring. The amplitude of the radial oscillations observed in the η ring allow us to estimate the mass of the perturbing moon Cressida. This is the first such measurement of small inner Uranian moon's mass and density. In Chapter 4 we track the presence and strength of periodic brightness variations in Saturn's dusty Roche Division and find that they are most likely caused by the seasonally varying planetary period oscillations of Saturn's magnetic field. This is just one of many ways in which the rings of Saturn have been found to be interacting with their magnetospheric environment.

Acknowledgments

First, I cannot emphasize enough, how truly fortunate and thankful I am to have worked with my advisor Matt Hedman. I cannot sufficiently describe here how instrumental Matt has been in all of my accomplishments. Matt has always been available to discuss anything with me whenever I needed and has shown me a constant and saintlike level of kindness, freedom, and respect. He has been accommodating of my interests and has always encouraged me to work on the projects that I liked. He has provided me with support to travel and learn and has inspired me to pursue so many unexpected projects and participation in teams at a level I don't think is normal or possible for most graduate students. With Matt as my advisor, I have always felt comfortable to pursue my graduate work at a level that was healthy for my well being. I have never felt any pressure, but only encouragement and support for whatever my future plans may be on any given day. It is incredibly difficult for me to think of an alternate situation where I complete this doctorate without Matt. I owe Matt a lot, and I hope he knows how much I appreciate the great job that he does and how good a friend and mentor he has been to me.

I'd also like to thank the other members of my committee, Jason Barnes, Doug Hamilton, and Francesca Sammarruca. Jason has been a huge influence over the years, making known many of the opportunities available in our field and encouraging all planetary science students to get involved in conferences, panels, summer schools, grant writing, and many other ways to prepare for our future careers. Jason has also provided another important guiding voice when it comes to presenting science at conferences and preparing publications. Doug has been particularly helpful in my understanding of the interactions between ring particles and both gravitational and non-gravitational forces through resonances, both in our discussions and in his many brilliant publications. Francesca provided me with the rigorous background of classical mechanics and mathematical methods necessary to tackle the complex problems in ring dynamics and was instrumental in preparing me to pass my written qualification exams, a feat I consider to be far more challenging and impressive than completing this dissertation.

Five years ago, I didn't know that a planetary science community existed. Today, I can't believe how lucky I am to be a part of it. The rings community in particular is a fascinating thing. There are so few people in the world who have worked on our solar system's ring systems over the years that you could almost name them all if you really wanted to. Probably, my favorite part about studying the rings is its own relatively small body of work, that is completely accessible and comprehensible (I guess maybe not all of the theoretical dynamics) in the timescale of a doctorate. The burst of publications after the discovery of the Uranian rings in 1977 and the following decade's progression through the Voyager 1 and 2 flybys of each of the outer planets is a remarkable historic work. Many of the folks from that time are still around, attending meetings, publishing papers, extending their academic lineages, and continuing to move the field forward. I am lucky enough to have worked with many of them along my way and to have received their advice and feedback. I must acknowledge many helpful and guiding discussions with Phil Nicholson, who is an authority on our field and its rich history. I owe a great deal to Dick French for his help and guidance in understanding the occultation data of the Uranian rings. I thank Mark Showalter for his inspirational publications and vocal excitement about my work with ring images from Voyager 2 at Uranus, Cassini at Saturn, and New Horizons at Jupiter. Also, for his dedication to preserving planetary imaging data in the planetary data system ring's node with Rob French and others. I again have to

thank Mark Showalter and Matt Tiscareno for their patient mentoring during many meetings to design and plan our observations of the rings and moons of Uranus and Neptune for the upcoming James Webb Space Telescope. I would also like to thank Maryame El Moutamid for her helpful navigation through the often intimidating and brilliant minds of the rings community.

I'd also like to credit some colleagues from the magnetosphere community. Gabby Provan, Stan Cowley, and Shengyi Ye were extremely informative and helpful in putting together a coherent message about the connection between Saturn's unique magnetosphere and dusty rings for our paper on the Roche Division. Their help prevented us from committing a number of blunders and resulted in an exciting new work connecting our two fields in the Saturnian system.

Thanks to our Physics Department secretary KarlaRose Erhard-Hudson for all of your help over the years. She always made sure I was reimbursed for travel in a timely manor and for helped to navigate the endless pointless paperwork and bureaucracy.

I'd also like to acknowledge the role of my friends in the physics department. First, my cohort from the first two years of classes, Rajani Dhingra, Lokendra Khanal, Negar Rajabi, Randy Millerson, and Shahla Nemati. I'm glad for the time we've gotten to spend together working, complaining, joking and especially for the support we've shared for each other over the years. I am especially thankful for the planetary crew I have spent many years with, particularly Shannon Mackenzie, John Ahlers, Rajani Dhingra, and Joseph A'hearn. The office discussions and jokes made my time at work bearable and the helpful feedback system, guidance, and support made EP 301 feel like a home.

I am particularly thankful for my friends Shannon Mackenzie, Michael France, and Megan Crowe and for all the beers, food, games, and adventures we have shared in and out of the Pow-louse. I really believe that good friends more than anything else have, for me, have made graduate school a breeze in the relative sense.

Thanks to my loyal friend Dom Flint, for your calls and your patience with my absence.

Thanks to my parents and family for the support you have provided. I apologize for my extended absences over the years.

A special thanks to Megan Crowe, who has been with me for this whole journey showing me her great patience and love. I almost never bother her about my work or school, nonetheless I'd like to express my thanks for listening to me complain, rant, and pontificate upon and about all of the other things I am interested in or perturbed by on a daily basis. As odd as she may find it, she is fundamental to maintaining my sanity in this strange world.

It has been a privilege to work at the University of Idaho for the last five years. I couldn't have possibly anticipated how much I would love it here in Moscow, Idaho and how many wonderful experiences I would have exploring the great outdoors of the Pacific Northwest.

Table of Contents

List of Tables

List of Figures

Chapter 1: Introduction

In the last several decades, scientists have discovered that planetary ring systems exist around all four of the giant planets in our solar system (Elliot et al., 1977a; Smith et al., 1979a; Hubbard et al., 1986). Very recently, ring systems have even been discovered around small asteroidal bodies in our solar system, orbiting between the giant planets (Braga-Ribas et al., 2014) and in the Kuiper Belt (Ortiz et al., 2017). In fact, planetary ring systems may be a ubiquitous phenomenon in the evolution of planetary bodies, soon to be determined with improved observations of planetary systems beyond our solar system (Barnes & Fortney, 2004; Aizawa et al., 2017, 2018).

The study of our planets' rings is of general interest for a number of reasons. From a more fundamental perspective, they are the most accessible analog to other astrophysical disks, such as the protoplanetary disks of gas and dust encircling newly formed stars and containing the signatures of newly formed planetesimals (Tamayo et al., 2015; Papaloizou & Terquem, 2006). Planetary rings even contain structures akin to spiral armed galactic disks (Toomre, 1964; Lin & Shu, 1964; Goldreich & Lynden-Bell, 1965), albeit on a much smaller scale. Studying our planetary ring systems at close range, along with improving physical simulations, can more clearly reveal the behavior of these many particle disk systems.

The giant planets' rings of our solar system have been observed from close range and in some cases over an extended period of time, allowing for a better understanding of their current structure and evolution. The *Cassini* mission in particular observed Saturn's rings, our most extensive and complex disk system, for 13 years of time variable study (Spilker, 2019). These high resolution observations allowed for a many faceted study of rings, including small scale wake structures created by the self-gravity of the constituent ring particles (Julian & Toomre, 1966; Salo, 1995; Salo et al., 2004), propeller structures created by large unseen ring particles (Tiscareno et al., 2006, 2008), complete gaps with irregular wavy edges sculpted by the largest embedded moonlets (Cuzzi & Scargle, 1985; Showalter, 1991; Weiss et al., 2009; Grätz et al., 2018; Seiß et al., 2010; Chancia & Hedman, 2016), resonant spiral density waves launched by more distant and larger moons (Goldreich & Tremaine, 1978a,b, 1980; Tiscareno et al., 2007; Tiscareno & Harris, 2018) or by commensurate oscillations of the planetary interior (Hedman & Nicholson, 2013, 2014; French et al., 2019b; Hedman et al., 2019; Mankovich et al., 2019), and even dusty ring interactions with solar radiation (Hedman et al., 2010a, 2013) and electromagnetic forces associated with the planet's magnetosphere (Burns et al., 1985; Schaffer & Burns, 1992; Hamilton, 1994; Chancia et al., 2019). The study of planetary rings has also revealed their intimate connection to the evolution of their home planetary systems and most notably to their relation to the formation or fragmentation of their moons (Duncan & Lissauer, 1997; Charnoz et al., 2010, 2011; French & Showalter, 2012; Tiscareno et al., 2013; Ćuk et al., 2016).

In addition to Saturn's famed ring system, planetary rings have been discovered around Uranus (Elliot et al., 1977a), Jupiter (Smith et al., 1979a), and Neptune (Hubbard et al., 1986). These discoveries, combined with a stream of unparalleled data and images from the *Voyager* 1 & 2 flybys (Smith et al., 1979a,b, 1981, 1982, 1986, 1989), gave birth to a vast advancement in the understanding and theory of planetary rings between the late 1970s and early 1990s. Our knowledge of these systems has progressed with continued observations of all the giant planets with the Hubble Space Telescope (Karkoschka, 2001a; Showalter & Lissauer, 2006; Showalter et al., 2006, 2019) and Keck Observatory (de Pater et al., 2007,

2013; de Kleer et al., 2013), the *Galileo* (Ockert-Bell et al., 1999) and *Cassini* (Porco et al., 2005; Tiscareno et al., 2019) orbiters around Jupiter and Saturn, and the *New Horizons* (Showalter et al., 2007) flyby of Jupiter. As our pictures of these planetary ring systems has improved we have sought to address many fundamental questions about the rings themselves. Why do all of the giant planets have rings? Why do all of the ring systems not look the same? How did the rings form? When did they form? How long will they last? None of these questions have simple and satisfying answers across the board, but we can cite compelling evidence that leads us toward a likely answer in some cases. This thesis does not directly answer these fundamental questions about the rings, but rather addresses some of the things we can learn about planetary systems using the rings themselves as a tool to probe their environment and establish connections between the various components in the system. This includes using the rings to probe for small unseen moons, to measure the mass of a moon for the very first time, and to quantify magnetic field fluctuations.

Saturn and Uranus in particular harbor the most diverse sets of rings among the giant planets. The broad dense main rings of Saturn are perhaps the most well recognized planetary phenomenon. However, Saturn also hosts vast spans of dusty rings best viewed when looking back towards our Sun from beyond the rings themselves (Showalter, 1996; Hedman et al., 2007, 2009a; Murray et al., 2008; Hedman et al., 2009b, 2012). Uranus is also better known for its denser rings, but they are extremely narrow (Elliot et al., 1978) and dark (Karkoschka, 1997) in comparison to Saturn's familiar broad and bright rings. Extensive dusty rings also span from inside these dense narrow rings, between them, and then beyond amongst the small inner moons (Murray & Thompson, 1988; Showalter & Lissauer, 2006; de Pater et al., 2006a,b). For context, I present schematics of the Saturnian and Uranian ring-moon systems in Figures 1.1 and 1.2, where the orbital radii of the ring features and moons are to scale. The size of the moons in each figure are displayed with a logarithmic scale based on their respective hill radii. While these systems share similarities, they are different on a fundamental level and likely have a different history and fate. Extensive sets of rings, such as these, are ripe for the exploration of interactions among their constituent ring particles and with other components of the planetary system. In fact, we now know that planetary rings respond to perturbations from many external forces. These include the planet itself and its interior (Hedman & Nicholson, 2013), the many moons orbiting the planet (Tiscareno & Harris, 2018), and even the planet's magnetic field and magnetospheric environment (Hedman et al., 2009a). By uncovering and characterizing new ring structures that are interacting with these various components of the system we can begin to unravel the many ways in which the planetary system is interconnected and in some cases gain insights of otherwise unknown physical parameters.

In the case of the Uranian rings, most of the available data pertain to its ten dense narrow rings. The manner in which these rings remain persistently narrow is still unsatisfactorily determined. Initially, the most widely accepted solution was that small moons should orbit on either side of each ring to gravitationally shepherd the ring particles into narrowly confined orbits (Goldreich & Tremaine, 1979). However, an extensive campaign of images obtained during the *Voyager 2* flyby revealed only two such moons straddling just the outermost ring (Smith et al., 1986). In total, only five of twenty ring edges can convincingly be explained away by appropriately located shepherding resonances with the known moons (Porco & Goldreich, 1987; Goldreich & Porco, 1987). Until recently, definitive measurements of these five

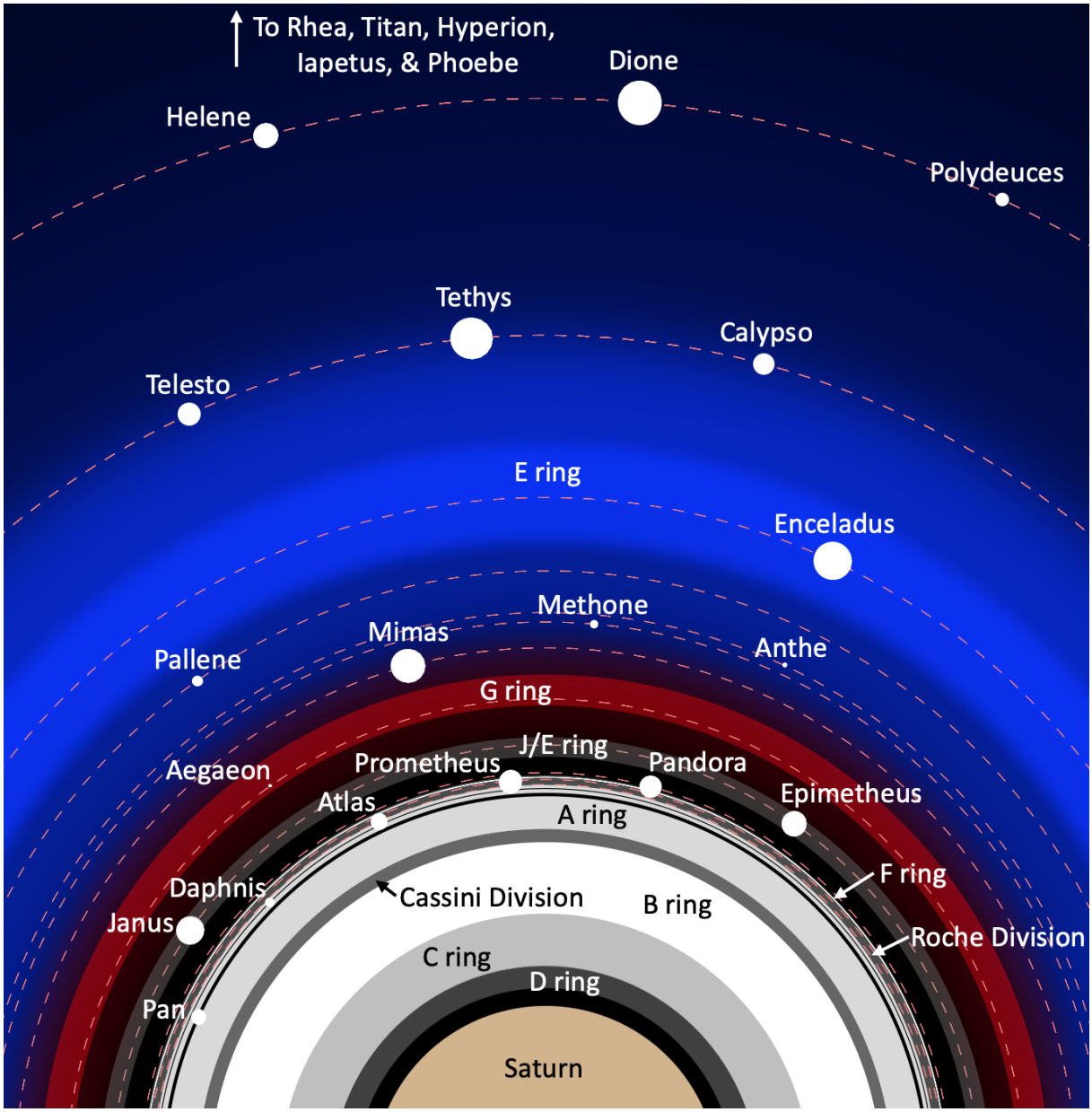

Figure 1.1: The inner Saturnian ring-moon system shown here contains 19 moons, 3 bright dense rings, and 6 fainter ring regions. The lighter white colored rings correspond the opaque A, B, and C rings easily visible from the Earth. The darker grey and transparent rings are the dusty rings best viewed from high-phase-angles. The Roche Division, located between the F ring and the A ring, is of particular significance to this work. The E ring and G ring spectral slopes are represented with blue and red, but this slope is due to their relative particle sizes, the E ring being composed sub-micron sized dust grains. The moons are represented by circles scaled logarithmically by using the moons' hill radii.

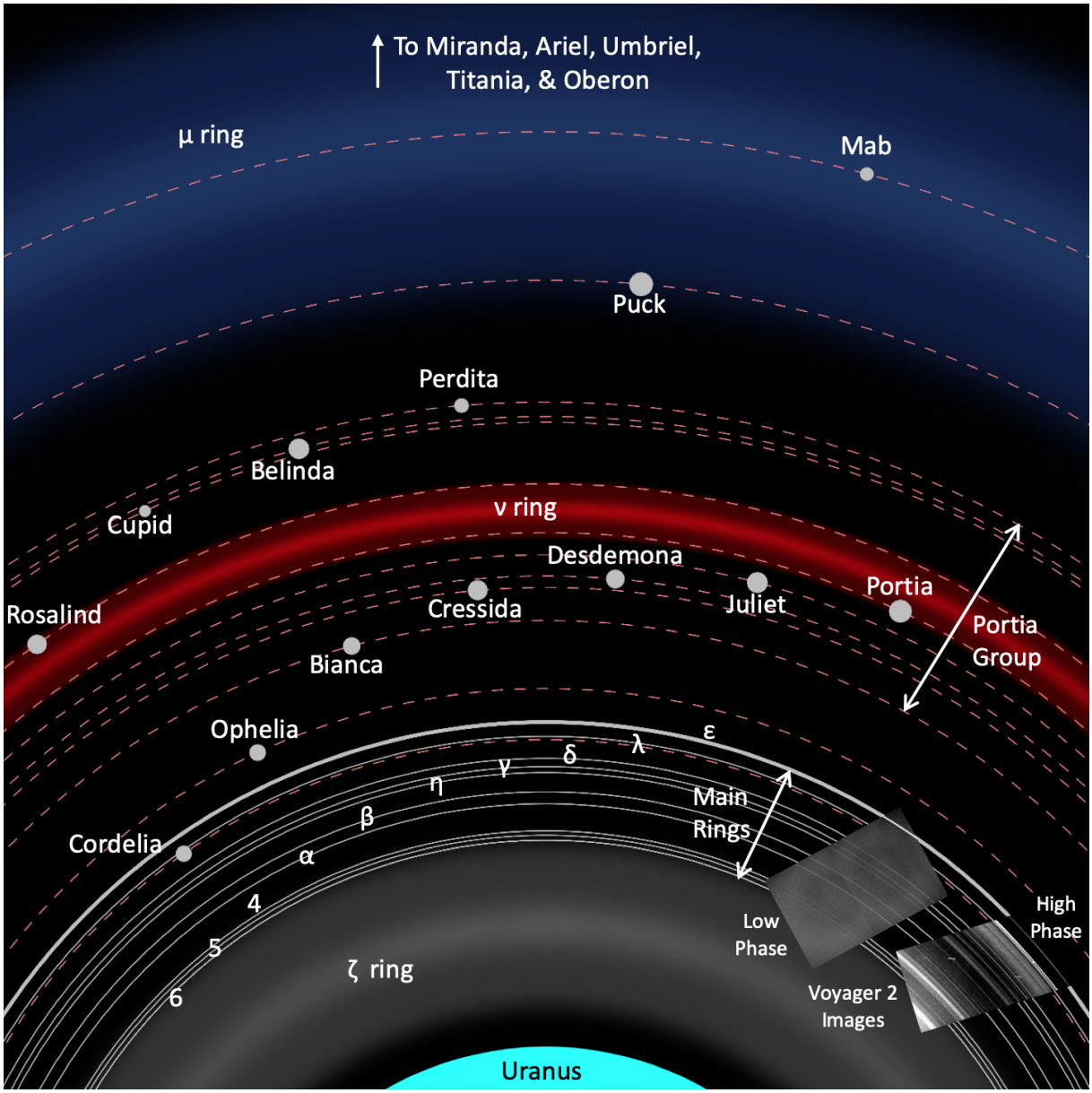

Figure 1.2: The inner Uranian ring-moon system shown here contains 13 moons, 10 dark dense rings, and 3 dusty ring regions. Two *Voyager 2* images are inset matched up with their location in the rings. The high-phase-angle image shows the poorly understood bands of dust that appear brighter than the narrow dense rings from this favorable lighting geometry. The blue and red again represent the spectral slopes of the two outer dusty rings, the μ ring being the only ring besides the E ring that features a blue spectral slope. The moons are represented by circles scaled logarithmically by using the moons' hill radii. The Portia Group consist of nine small inner moons that orbit within a radial range of less than $18,000$ km, making the most tightly packed system of moons in our solar system.

resonances' effects on the rings' shape, brightness, and orientation were largely unpublished, appearing only in a small number of presentation abstracts (French & Nicholson, 1995; Showalter, 2011).

The mystery of narrow rings has now spread to the Saturn system, where *Cassini* observations have unveiled a number of similarly narrow, sharp edged, and noncircular ring features (Nicholson et al., 2014a; Hedman et al., 2014; Nicholson et al., 2014b; French et al., 2016a). In determining the properties of these ring features we have learned about the different ways in which ring-moon interactions can be manifested through various classes of resonances and we are beginning to understand the complexity of freely precessing normal modes and axisymmetric structures produced in conjunction with perturbed rings and edges (Hedman & Nicholson, 2019). Aside from a better understanding of planetary rings, these studies have also revealed new connections with the interior oscillations of Saturn (French et al., 2016b), and can even provide constraints on the planets pole direction and zonal gravity harmonics (French et al., 2017; Nicholson & Porco, 1988). In some cases we may also obtain estimates of the masses of perturbing satellites (Weiss et al., 2009). This feat is particularly remarkable when applied to Uranian ring-moons, whose masses and compositions are entirely unknown.

The Uranian system is structured such that its dense main rings are found within the Roche limit, loosely defined as the radial location beyond which the ring material of a presumed critical density will accrete and form a moon (Tiscareno et al., 2013). In fact, the innermost moon, Cordelia orbits just interior to the ϵ ring providing solid evidence for the location of this transitional zone between rings and moons. The inner ring-moon system around Uranus is particularly tight, hosting eleven known moons inside of the planet's corotation radius, nine orbiting within a radial range of less than $18,000$ km. This configuration is contrary to the Saturn system, where the corotation radius is in the middle of the dense B ring and interior to the Roche limit near the outer edge of the A ring. Thus, the dynamical evolution of the Uranian ring-moon system should be very different. While the tightly spaced moons of Uranus tidally migrate inwards from the corotation radius they may gravitationally interact with neighboring moons through resonances, chaotically collide and form temporary rings, cross resonances with the existing rings and be torqued outwards, or possibly migrate inside the Roche limit and eventually produce a more massive Uranian ring (Showalter & Lissauer, 2006; French & Showalter, 2012; Tiscareno et al., 2013; French et al., 2015; Hesselbrock & Minton, 2019). These scenarios differ from the Saturn system, where all moons are located beyond the corotation radius and are both tidally migrating away from the rings and being torqued away from the rings through their many resonances with the massive A and B rings. To fully understand the dynamical processes at work in the Uranian system and its unique history and formation we require a full inventory of small inner moons and better estimates of their masses and compositions. Until better observations can be obtained from a new mission to the planet or from improved Earth-based telescopes, we can exploit the data we currently have to characterize all of the detectible ring structures and provide constraints on the existence and mass of all associated perturbing moons.

Turning to the Saturnian rings, one major recent advancement in ring science prompted by data from *Cassini* was the analysis of patterns within the rings that are perturbed by oscillations inside Saturn itself (Hedman & Nicholson, 2013). This allowed for more advanced modeling of the planetary interior through seismology, an unlikely feat for a gas giant planet (Mankovich et al., 2019). Along with the discovery

of these patterns are the detections of slower moving density wave structures perturbed by something moving near the rotation rate of the planet itself (Hedman et al., 2009a; Hedman & Nicholson, 2014). In this case, multiple physical phenomena associated with Saturn's rotation can be interacting with the rings simultaneously. Gravity measurements obtained during *Cassini's* grand finale revealed significant mass anomalies in Saturn's equatorial jet (Iess et al., 2019) or at other latitudes rotating around the planet in range of Saturn's zonal wind speeds (García-Melendo et al., 2011). Such anomalies may produce resonances in the rings similar to a massive satellite (Sicardy et al., 2019). Other structures may be in resonance with the bulk planetary rotation rate (Mankovich et al., 2019) or the differential rates of a cylindrically layered planetary interior (El Moutamid et al., 2018). Additionally, a number of periodic brightness variations in Saturn's dusty D ring and Roche Division were found to be in sync with the rotational modulation of Saturn's kilometric radiation (Hedman et al., 2009a). This association became of greater significance as the *Cassini* mission progressed and several periodic phenomena associated with the magnetosphere were found to drift in sync with Saturn's seasonal magnetospheric periods (Ye et al., 2018). Our study of these dusty ring structures and the time variable forces exerted upon them explores a new mechanism for the shaping of dusty rings by their magnetic field and reveals the unexpectedly long range propagation of resonant structures in dusty rings, drawing connections to Saturn's mysterious spokes (Porco & Danielson, 1982; Mitchell et al., 2006, 2013).

The treasure trove of giant planet data obtained by the *Voyager* and *Cassini* spacecraft has truly revolutionized our ability to study planetary rings. We have begun to reach beyond the basic questions of planetary ring dynamics and consider the complex behavior of the many interrelated components of the giant planetary systems. In Chapter 2 I explore the ring occultation observations obtained by *Voyager 2* during the Uranus flyby and identify structures akin to satellite wakes in the α and β rings that may point to the presence of two tiny moonlets, undetected in the *Voyager 2* images. I investigate a comprehensive set of ground-based occultations of the Uranian rings in Chapter 3 and detect a new structure in the η ring that allows us to measure the mass of the small moon Cressida for the first time. In Chapter 4 I survey images of Saturn's dusty Roche Division taken over the course of the entire *Cassini* mission and model the influence of small oscillations of Saturn's magnetic field that vary in frequency over the course of the mission. Finally, in Chapter 5 I summarize the significance of the work in this thesis, make note of the preliminary and future projects related to this work, and anticipate new planetary ring data from future missions.

Chapter 2: Are there moonlets near the Uranian α and β rings?

Chancia, R.O., Hedman, M.M."Are there moonlets near the Uranian α and β rings?" *The Astronomical Journal, 152, 211, 2016*

In this work I began my investigation of rings. The project reported here was not specifically anticipated in the proposal seeking to use an extensive set of Uranian occultation data, obtained by decades of ground-based campaigns and from spacecraft, to explore ring dynamics and place constraints on the planet's internal structure. However, at the time of my initial investigations, we only had access to the public data on the Planetary Data System's (PDS) rings node, which includes the Voyager 2 occultations and images, but not the decades of ground-based occultation data that are needed for the primary goal of the investigation. The Voyager 2 occultation data contains the only information we have about the Uranian rings' internal structure. Thus, the goal of my initial investigation was to use newly developed data analysis tools, used to great success with the Cassini occultations, to re-examine the older Voyager 2 data. This re-examination of data included a new set of eyes armed with tools that were not developed when the data were initially obtained and analyzed several decades ago. The key targets were the ϵ, δ, and γ rings, where we hoped to analyze the signatures of density waves launched at resonances on the rings' edges. While interesting features do exist there, I also found periodic variations in ring material on the edges of the α and β rings that are more reminiscent of satellite-wakes than of the variations of a density waves produced in long range satellite resonant interactions.

These signatures in the α and β rings can be explained by small satellites orbiting just outside the orbits of each ring. Estimates of their masses place them below the detection limit of the Voyager 2 images. If the moons are discovered in the future they may be used as evidence that a single nearby moon can shepherd a narrow ring through angular momentum flux reversal over the entire narrow ring. A very recent reconstruction of the raw radio science subsystem occultation data was presented at the Division on Dynamical Astronomy 2019 meeting (French et al., 2019a) and shows the wake structures in the wavelet transforms of the α ring at even greater radial resolution than in the PDS data.

2.1 Abstract

The *Voyager 2* Radio Science Subsystem occultations of the Uranian α and β rings exhibit quasi-periodic optical depth variations with radial wavelengths that vary with longitude. These patterns may be wakes from small moonlets orbiting exterior to these rings. Based on the observed structures in the rings, we estimate that the moonlets would need to be located ~ 100 km exterior to the rings' semimajor axes (106^{+22}_{-12} km for α and 77^{+8}_{-4} km for β) and be $2-7$ km in radius. Such moonlets could help keep the rings confined. Due to their small radii and presumed low albedo, the expected brightness of these moonlets is on the order of the noise in *Voyager 2* images.

2.2 Introduction

The Uranian ring system was the second to be discovered in our solar system, thanks to multiple ground-based stellar occultation observations of Uranus on 1977 March 10 (Elliot et al., 1977b). The nine classical rings of Uranus (named $6, 5, 4, \alpha, \beta, \eta, \gamma, \delta$, and ϵ) are narrow ringlets with widths between 1 and 100 km (French et al., 1986a). These rings eluded discovery for so long both because they are narrow and because they are composed of extremely dark particles with geometric albedos around 0.05 (Karkoschka, 2001a). Many of the rings are also eccentric, with radial deviations from circular as large as several tens to hundreds of kilometers, and inclined by as much as 0.06° (French et al., 1988). Various theories have been proposed to explain the overall architecture of this ring system, which are best summarized in Elliot & Nicholson (1984) and French et al. (1991). The proposed solutions include a system of shepherd satellites with appropriate resonances at each ring edge, as well as embedded satellites within the rings (Dermott et al., 1979).

While the ground-based occultation data obtained since 1977 have provided the rings' orbital elements and widths, they do not have sufficient resolution to reveal the rings' fine-scale interior structure. The only data regarding this structure come from the three occultation experiments performed during *Voyager 2's* flyby of Uranus in January of 1986. Details regarding the *Voyager 2* occultations are found in Holberg et al. (1987) (Ultraviolet spectrometer—UVS), Gresh et al. (1989) (Radio Science Subsystem—RSS) and Colwell et al. (1990) (Photopolarimeter Subsystem—PPS). These high-resolution observations enabled the structure of these narrow rings to be examined in more detail. For example, Porco & Goldreich (1987) used the orbital elements determined by Owen & Synnott (1987) for the small moons Cordelia and Ophelia and the orbital elements of the ϵ ring (French et al., 1986a) to show that the moons' eccentric resonances located on the inner and outer edges of the ϵ ring could be keeping the ring radially confined. They also showed that other resonances with these moons could confine the outer edges of the δ and γ rings. Forty years after the rings' discovery, these two shepherd satellites remain the best evidence for moonlets confining narrow rings. However, the search for additional moons to shepherd the remaining ring edges has not been successful (Murray & Thompson, 1990).

Here we will use the high-resolution *Voyager* data to analyze the interior structure of the α and β rings, both of which exhibit quasi-periodic optical depth variations. These structures are unusual in that their radial wavelengths vary with longitude, even after accounting for the observable changes in the ringlet's width. Such longitudinally variable wavelengths are a characteristic of wakes generated by nearby moons, and so we explore that possibility in depth in this paper. Showalter et al. (1986) developed a model of such moonlet wakes to determine the location of the small moonlet Pan in the Encke Gap of Saturn's A ring using occultation data. We use their model to determine the possible location of a tiny moonlet just exterior to the β ring and of another moonlet possibly perturbing the α ring. These moons have locations and masses that are consistent with existing limits and dynamical constraints, and they could help confine these rings.

In Section 2 we describe the *Voyager 2* RSS occultations used for this analysis. In Section 3 we summarize the theoretical background of the narrow ring problem and moonlet wakes. Section 4 shows the application and results of our ring occultation scan analysis and the resulting estimates of the α

Table 2.1: Geometry of Radio Science Subsystem (RSS) occultations

Ring	Occ.	True Anom. (deg)	Mid-time (hr:min:s)	Mid-rad. (km)	Mid-long. (deg)	Inner Edge (km)	Outer Edge (km)
α	RSSI	124.4	19:55:58.385	44,736.75	342.1	44,731.45	44,742.04
	RSSE	340.2	22:39:26.294	44,686.59	198.1	44,684.48	44,688.70
β	RSSI	13.9	19:54:07.459	45,640.74	342.5	45,637.22	45,644.25
	RSSE	228.9	22:41:26.104	45,673.33	197.7	45,667.73	45,678.92

The appended labels of I and E stand for ingress and egress. The true anomaly of each ring at the time of their respective ring intercept mid-times is calculated from the inertial longitudes provided and updated precession rates provided by R. G. French and summarized in Table 2.2. Mid-times listed are the times of ring intercept measured in seconds after UTC 1986 January 24 00:00:00, when the RSS microwaves intercepted the mid-ring radius. The corresponding mid-radii are explicitly calculated as halfway between the two edge radii and may differ slightly from those of other sources whose mid-radii refer to a location weighted on the equivalent depth of the occultations scans. Mid-longitudes similarly correspond to mid-ring radii and mid-times.

and β moonlet orbits and masses. In Section 5 we show that these moonlets could plausibly have avoided detection in the *Voyager 2* images. Lastly, we present our discussion and conclusions in Section 6. Appendix A describes our method of calculating the RSS α ingress wavelength, while Appendix B discuses an analysis of the PPS occultations.

2.3 Occultation Data

The data for this investigation consist of occultations obtained by the RSS instrument on board the *Voyager 2* spacecraft, available on NASA's Planetary Data System Ring-Moon Systems Node website.[1] RSS generated a complete ingress and egress occultation of the rings (separated longitudinally by $\sim 145°$) by transmitting microwave radiation of wavelengths 3.6 cm (X band) and 13 cm (S band) through the rings to ground stations on Earth (Tyler et al., 1986; Gresh et al., 1989). These radio wavelengths are not to be confused with the ring density wavelength of the rings' wake structure to follow. Note that the PPS stellar occultation of β Persei (Algol) is of higher spatial resolution but lower signal-to-noise ratio than the RSS occultations (Colwell et al., 1990; Graps et al., 1995), and the UVS performed the same occultations as the PPS, but at a lower resolution. We find that these stellar occultations do not have sufficient signal-to-noise to provide further evidence for or against the idea that these rings may contain moonlet wakes. Our analysis of the PPS occultations is included in Appendix B.

Table 2.1 provides a summary of the RSS occultation data set used here, giving mid-times, inertial longitudes and radii, and true anomalies for the α and β rings at the time of the ingress and egress occultations, as well as our estimated positions of the ring edges, consistent with Gresh et al. (1989). Figure 2.1 shows both the ingress and egress RSS occultations of the α and β rings (for occultation scans of all rings with all instruments see French et al., 1991). We show the ring profiles scaled so that the rings appear to have a common width. This provides a better view of the internal structure of the rings and enables direct comparisons of the ring scans with different true anomalies and widths. The outer

[1] http://pds-rings.seti.org

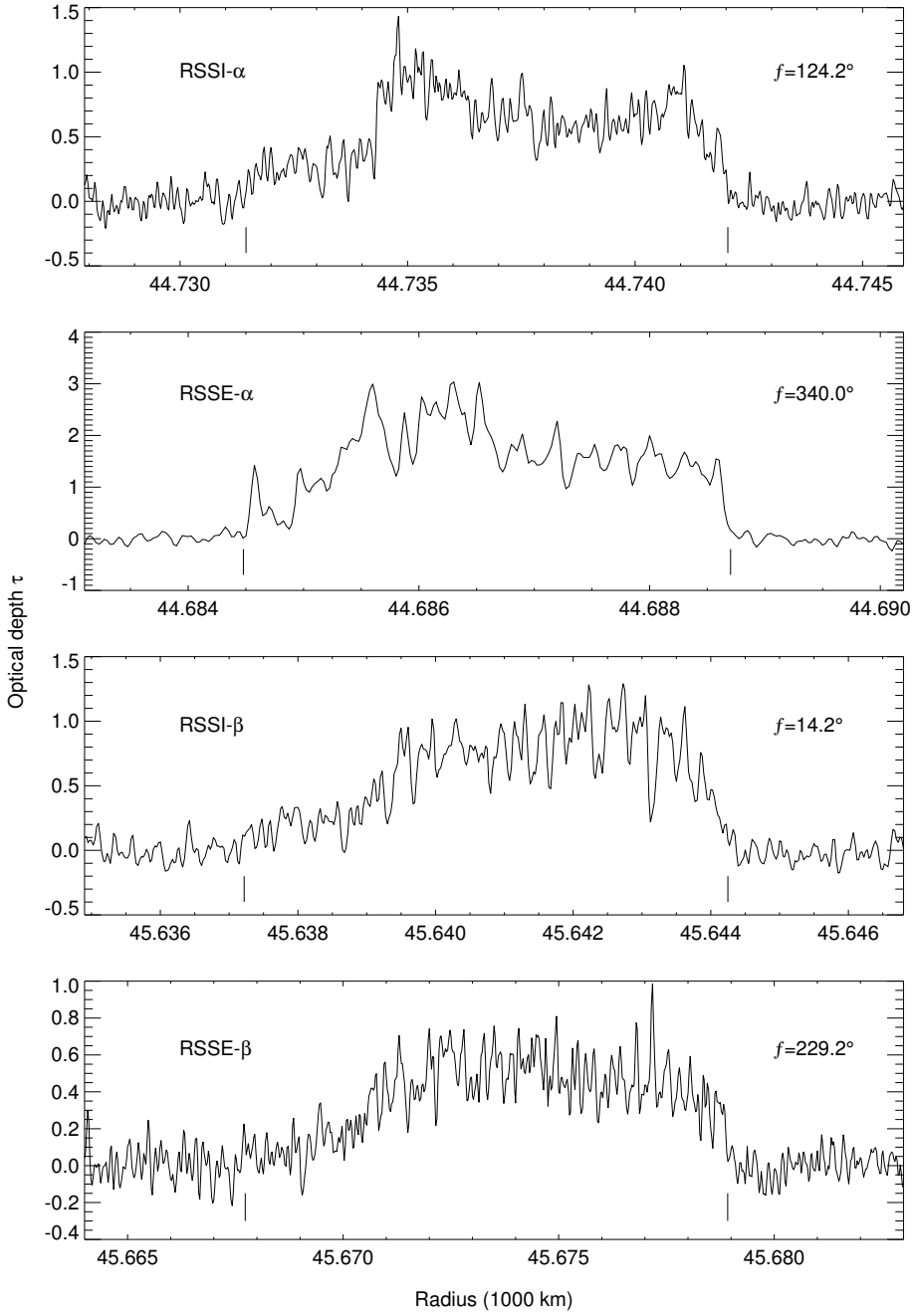

Figure 2.1: RSS occultation scans of the α and β rings. Note the varying scales of both optical depth and radius for each plot. The plots are stretched with these varying scales to a common width to allow comparison of features in their radial structure. This stretching is most apparent in the RSSE-α scan, whose actual width is only 4.22 km, compared to the RSSE-β scan, whose actual width is 11.19 km. Ring edge radii from Table 2.1 are marked with single dashes below the data. The true anomaly of each scan is provided in the upper right. The two β scans have different wavelengths of quasi-periodic optical depth variations near their outer edges. The α egress scan also shows a periodic structure near its outer edge, and some narrow evenly spaced dips are in the ingress scan.

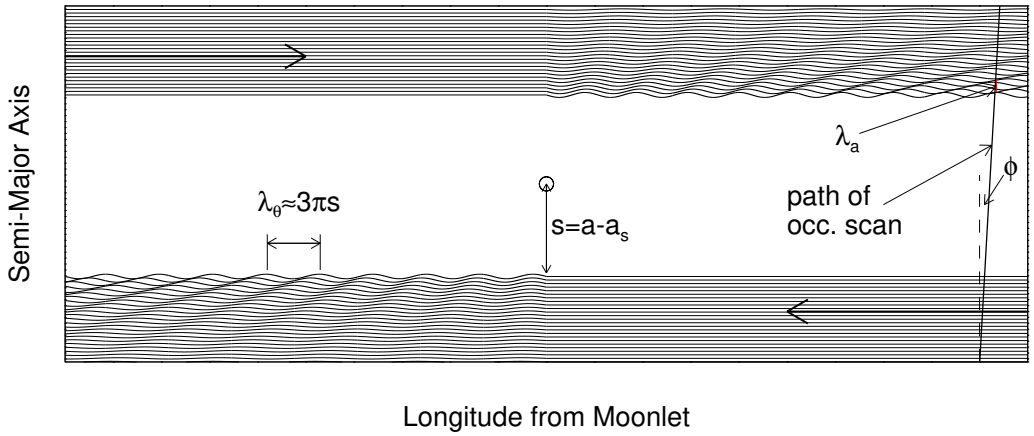

Figure 2.2: Schematic of the ring–moon wake interaction, in a reference frame centered on the moon. Ring material closer to the planet in the lower half of the figure is moving faster than the moon and passes it to the left, and the ring material in the upper half is moving slower and is passed by the moon. The diagonal line on the right side is meant to simulate the path of an occultation scan through the rings.

Table 2.2: Ring orbital elements

Ring	a (km)[a]	ae (km)[b]	ϖ_0 (deg/day)	$\dot{\varpi}$ (deg)	q_e	q_ϖ
α	$44,718.96 \pm 0.13$	34.01 ± 0.10	332.75 ± 0.35	2.18542 ± 0.00009	0.57	$+0.07$
β	$45,661.39 \pm 0.11$	20.15 ± 0.09	223.30 ± 0.55	2.03115 ± 0.00012	0.27	$+0.003$

[a] Provided by R. G. French. Listed longitude of pericenter, ϖ_0, corresponds to the epoch: UTC 1977 March 10, 20:00:00.

[b] $q_e = a\delta e/\delta a + e$ and $q_\varpi = ae\delta\varpi/\delta a$ are from Table VII of French et al. (1991) and are determined only from the *Voyager 2* RSS data.

region of each ring contains a series of dips and peaks, most obviously seen in the α and β egress scans. In both ringlets, these periodic structures do not have the same wavelength in the ingress and egress scans. Such longitudinally variable wavelengths are atypical of many ring features, like density waves, but are characteristic of moonlet wakes, and so we hypothesize that these structures are caused by nearby perturbing moonlets.

2.4 Theoretical Background

Over time, the continuous dissipation of energy through inelastic particle collisions in a dense ring will cause it to spread out radially (Goldreich & Tremaine, 1982; Stewart et al., 1984). In standard models, an unperturbed, narrow ringlet should spread on timescales of only a small fraction of the age of the solar system, $\sim$ 2500 yr for rings comparable to the α and β rings (Murray & Dermott, 1999, p. 497). One possible mechanism for confining ring edges is through the gravitational perturbations of a nearby satellite (Goldreich & Tremaine, 1982; Borderies et al., 1984). Such moons should produce observable

structures in a ring in the form of wavy edges and moonlet wakes. Indeed, Showalter (1991) was able to find Saturn's small moon Pan in *Voyager 2* images after determining its orbital elements based on optical depth variations observed in occultation scans of the surrounding A ring (Showalter et al., 1986).

To understand this mechanism, consider a ring particle on a circular orbit at semimajor axis, a, slowly passing by a moonlet at semimajor axis $a_s > a$. While passing by the moonlet, the ring particle gains a net gravitational acceleration in the radial direction toward the moonlet and thus a small component of velocity in the radial direction, v_r. This radial velocity puts the ring particle on a slightly eccentric orbit with an apoapsis located one-quarter of its orbit downstream from the moonlet–ring interaction. As additional ring particles from the original circular ringlet pass by the moonlet, they undergo the same interaction. The gradually shifting apoapsis location induced in the ring particle orbits forms a wavy edge to the ring with azimuthal wavelength, $\lambda_\theta(a) \approx 3\pi\,|s|$ (Cuzzi & Scargle, 1985), where $s = a_s - a$. The wavy edge appears ahead of the moonlet if the ring is interior to the moon and trails the moonlet if the ring is exterior (see Figure 2.2). A moonlet a few kilometers wide would only produce variations in the edge position of around 20 m (calculated from Cuzzi & Scargle, 1985, Equation (3)), which would be undetectable in the *Voyager 2* data. However, the azimuthal wavelength's dependence on s causes it to vary significantly over the width of a ring, with ring particle streamlines farther from the moonlet exhibiting a longer wavelength. Over a number of periods these adjacent streamlines start to go out of phase. This crowding of the streamlines results in a pattern with alternating areas of higher surface density and areas of lower surface density. We observe this as quasi-periodic optical depth variations in the occultation scans of the ring downstream from the moonlet, known as a moonlet wake.

Showalter et al. (1986) developed a model precisely for the purpose of finding the location of a moonlet given measurements of these wake wavelengths at multiple longitudes. They found the wavelength in a linear scan to be

$$\lambda_a \approx 3\pi \frac{s^2}{a_s\,|\theta|}\left[1 - \left|\frac{s}{a_s\theta}\right| \tan(\phi)\right]. \tag{2.1}$$

Here θ is the angle of azimuthal separation between the moonlet and the longitude of the occultation scan, and ϕ is the angle the occultation scan makes with the radial direction. This wavelength increases as s^2 and decreases inversely with azimuthal separation from the moonlet. We should note here that the wavelength, λ_a, is specifically referring to the wavelength of optical depth variations in a radial occultation scan of a circular ring. Because the Uranian rings are actually eccentric and their widths vary systematically with their average radius, the wavelength we measure in our occultations is not representative of the actual wavelength the moonlet would produce using this model. We therefore convert all of our occultation scans to 'semimajor axis space' using the formula

$$da = \frac{dr}{(1 - q_e\cos(f) - q_\varpi \sin(f))}, \tag{2.2}$$

adapted from French et al. (1991), where q_e and q_ϖ are the eccentricity and pericenter gradients of the ringlet (see Table 2.2) and f is the true anomaly (see Table 2.1). This allows us to translate the observed optical depth profiles into semimajor axis space and thus compute the appropriate wavelength of the wake λ_a. If ϕ is small, as it is for the RSS occultations (see Figure 2 of French et al., 1991), we can

neglect the second term on the right-hand side of Equation 2.1 and solve for a_s as a function of θ:

$$a_s \approx a + \frac{\lambda_a |\theta|}{6\pi} \pm \sqrt{\frac{\lambda_a^2 \theta^2}{36\pi^2} + \frac{a\lambda_a |\theta|}{3\pi}}. \tag{2.3}$$

We can therefore plot a curve $a_s(\theta)$ giving the possible locations of a moon that could be responsible for producing an observed value of λ_a. These positions can further be expressed in terms of an absolute longitude of the satellite in an inertial reference frame (θ_s), by subtracting the appropriate longitude of the occultation data. We compare the location curves of multiple scans (after shifting their longitudes to a common epoch) and look for a common location as cause of the optical depth variations. Based on the location and amplitude of the optical depth variations, we can determine the mass of the putative moonlet (see Section 4 below).

2.5 Occultation analysis

To determine the wavelength of the optical depth variations in each occultation scan, we use a combination of wavelet and localized Fourier transformations. Wavelet transforms provide maps of the strength of periodic structures as a function of radius and wavelength and have proven useful for studying a variety of structures in dense rings (e.g. Tiscareno et al., 2007). The extent of the optical depth variations in the α and β rings is only a few kilometers at most, so we do not expect the wavelength to vary with radius by more than ∼1-5%. However, the spatial aspect provided by a wavelet transform illustrates where the periodic signal is detectable and demonstrates that it has different wavelengths in the two scans. Once the appropriate regions are identified through wavelet analysis, more precise wavelengths are determined via a Fourier transformation of the relevant ring regions.

We compute the wavelet transform for each profile with the standard wavelet routine in the IDL language (Torrence & Compo, 1998) using a Morlet mother wavelet with $\omega_0 = 6$. Figures 2.3 and 2.4 show the resulting wavelet transforms for each RSS α and β profile as a function of semimajor axis and wavenumber. Here the occultations' radii have been translated to effective semimajor axes so that we can obtain the appropriate λ_a wavelengths. The darker regions show the locations where the periodic signal is strongest. The most obvious periodic pattern is seen in the outer half of the α ring's egress scan between semimajor axes of 44,719 to 44,723 km, where the wavelength is 0.59 km. The β ring wavelets show similar periodic optical depth variations near the ring's outer edge (semimajor axes between 45,663-45,664 km) with different wavelengths in each scan, 0.45 km for ingress and 0.31 km for egress. In order to obtain precise estimates of the patterns' wavelengths, we compute over-resolved Fourier transforms of the above regions, which are shown in Figure 2.5. Note that we actually determined the wavelengths from gaussian peak fits of the Fourier power versus wavenumber and then converted to wavelengths. This was done because the peaks in the power spectrum are more symmetric in wavenumber space. The wavelengths derived from these methods are given in Table 2.3, along with their uncertainties $\sigma = \sqrt{2}\delta r/N$ (Hedman et al., 2007), where δr is the occultation scan's radial resolution and N is the number of wavelengths that extend across the radial region where the wavelength is measured.

Compared with the other occultations, the wavelet transform of the α ring ingress profile shows much

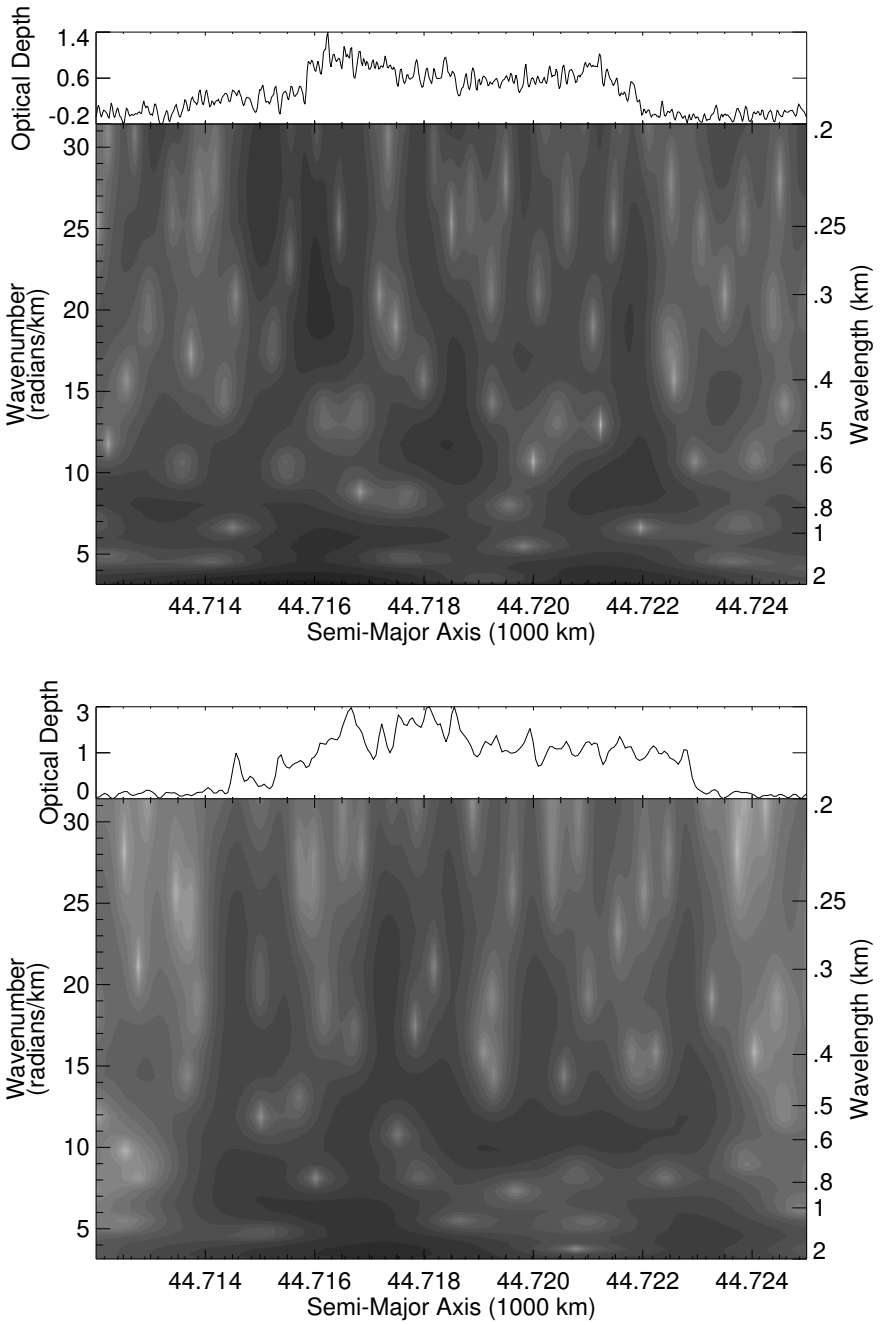

Figure 2.3: We use wavelet transforms to determine the wavelengths of the quasi-periodic optical depth variations of the α ingress (top) and egress (bottom) occultation scans. The strength of the periodic signal for a given radius and wavenumber are shown in the contour map, where darker corresponds to a stronger signal. The egress wavelet shows a strong sinusoidal periodic structure from 44719-44723 km with a wavelength of 0.59 km. The ingress scan is composed of periodic sharp dips and peaks that do not produce clear signals at one wavelength in these transforms.

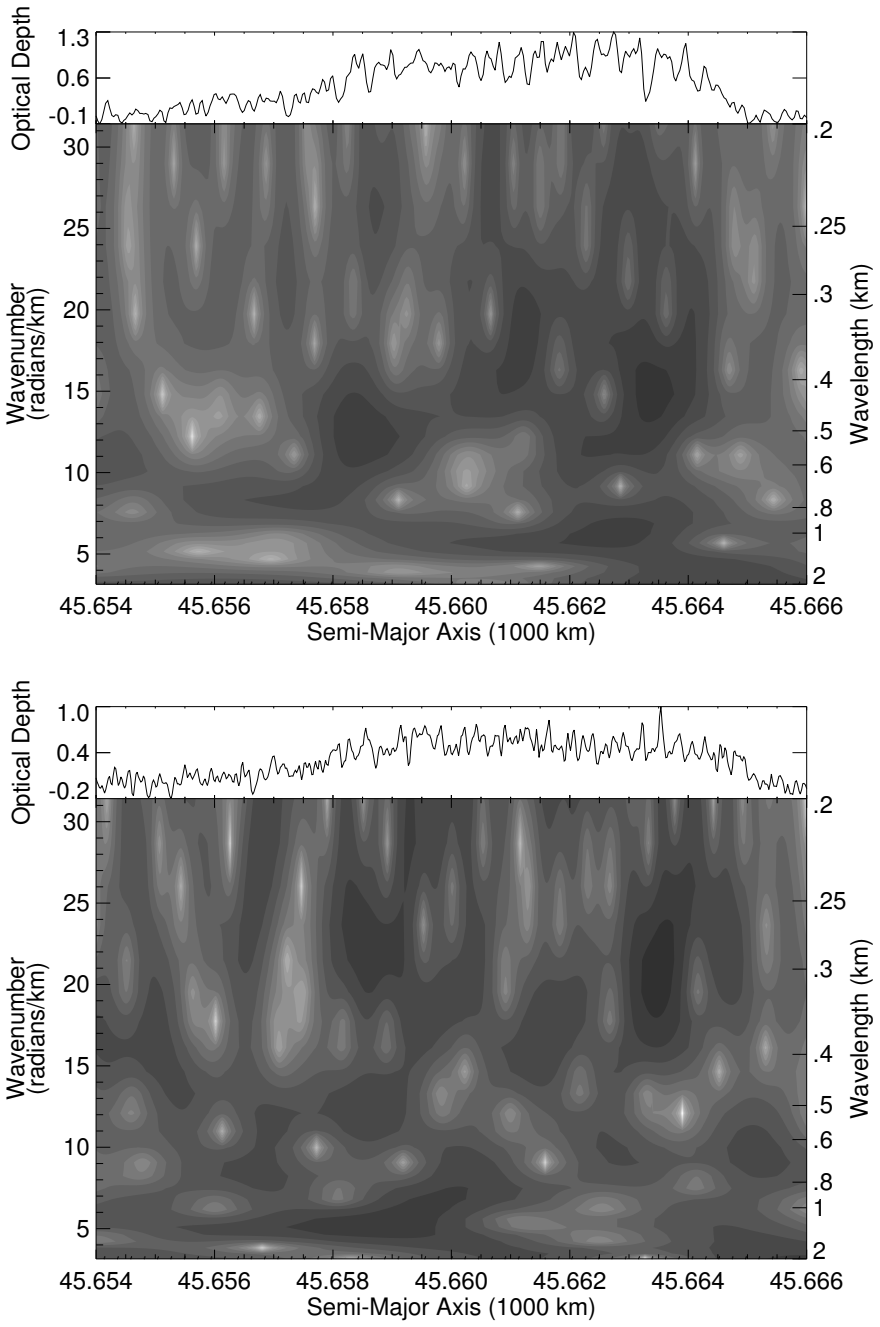

Figure 2.4: The β ring wavelet transforms detect different wavelengths of the optical depth variations seen near the outer edge of the ring in each scan. From 45663-45664 km we find a wavelength of 0.45 km for the ingress scan and 0.31 km for the egress scan. Fourier transforms of these radial regions are shown in Figure 2.5.

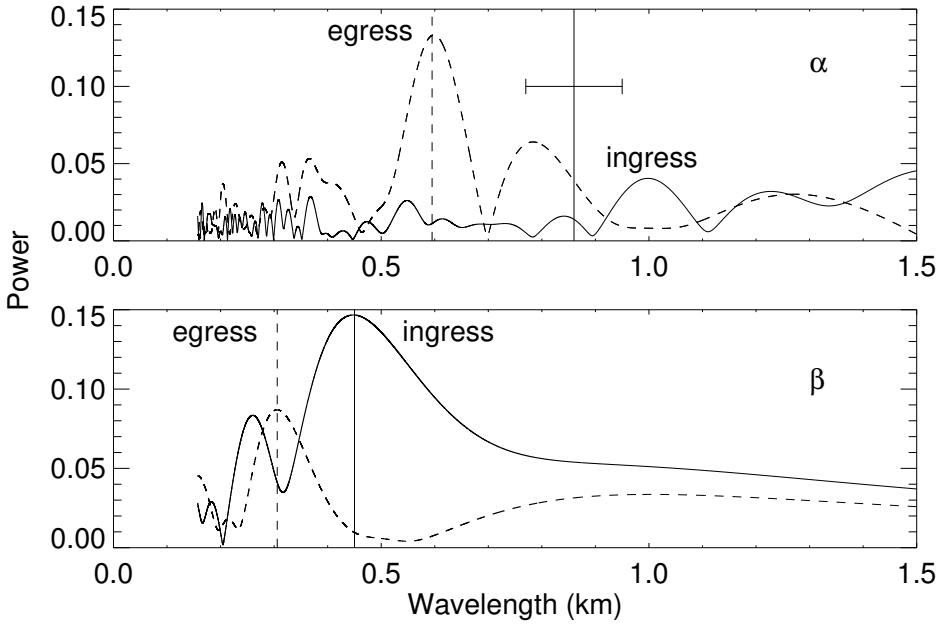

Figure 2.5: Localized Fourier transforms of regions identified in the wavelet transforms from Figure 2.3 and 2.4 for the α (top) and β (bottom) rings. The top plot contains the transforms of the α ring scans from $a = 44,719$ to $44,723$ km. The α ingress scan wavelength, shown with its larger error bar (uncertainty of other scan wavelengths is small), was not determined from this Fourier transform; see Appendix A. We did not consider the bump at ~ 1 km in the α ingress Fourier spectra to be significant. If it did happen to be the real wavelength, it also produces a solution consistent with a small moonlet of about 2 km in radius. The β ring plot contains the transform of both scans from $a = 45,663$ to $45,664$ km. We plot transforms of the ingress scans with solid lines and the egress scans with dashed lines. Exact wavelength values and uncertainties are summarized in Table 2.3. We believe that the smaller bump at ~ 0.25 km in the β ingress transform is a harmonic of the actual wavelength.

Table 2.3: Moonlet Locations

Ring	λ_I (km)	λ_E (km)	a_s (km)	$\theta_s(^\circ)$	s (km)
α	0.86 ± 0.09[a]	0.59 ± 0.01	44825^{+22}_{-12}	182^{+45}_{-99}	106^{+22}_{-12}
β	0.45 ± 0.01	0.31 ± 0.01	45738^{+8}_{-4}	186^{+18}_{-40}	77^{+8}_{-4}

[a] The wavelength for the α ingress scan was determined by visual inspection of the series of dips rather than through wavelet and Fourier analysis. Its larger error is the standard error of the mean wavelength calculated in Appendix A.
Moonlet semimajor axis, a_s, inertial longitude at the epoch of the ingress occultation scan (see Table 2.1), θ_s, and ring–moon radial separation, s, relative to the rings' semimajor axes in Table 2.2, determined using the ingress and egress wavelengths, $\lambda_{I/E}$, of the quasi-periodic optical depth variations near the outer edges of the rings (λ_a).

more disorganized signals. This is most likely because the periodic structure in this profile seems to consist of periodic narrow dips, rather than a sinusoidal wave. The variations in the morphology of the α ring patterns are similar to those seen in a density wave located within the Maxwell ringlet in Saturn's rings. Indeed, French et al. (2016a) found that the detailed morphology of the optical depth variations associated with this wave varied systematically with the ringlet's true anomaly. While at many true anomalies the optical depth variations were sinusoidal, when the true anomaly was close to 90° (i.e. similar to the α ingress scan), the optical depth variations in the wave become very narrow dips and peaks, similar to those seen in the α ingress profile. The lack of a sinusoidal periodic structure made Fourier-transform-based estimates of the pattern wavelength problematic, and so we found it more effective to estimate the wavelength of the α ingress scan by visual inspection and determination of the separation of the individual dips in optical depth (see Appendix A).

We insert the derived wavelengths, along with the rings' most precise semimajor axes contained in Table 2.2, into Equation 2.3 to generate the curves of allowed locations of moons shown in Figure 2.6. In each panel, both curves are shown in a reference frame computed at the time of the ingress scan. The location where the ingress (solid lines) and egress (dashed lines) curves cross gives the semimajor axis a_s and the inertial longitude θ_s a moonlet would need to have in order to cause the optical depth variations seen in both scans. In Table 2.3, we show the input wavelengths, λ_a, for the ingress and egress scans and moonlet locations (circles in Figure 2.6) consistent with both scans for the α and β rings. The uncertainties in the wavelengths propagate through the calculations of the moonlet locations, whose listed uncertainties are then taken from the largest deviations in each case. We find for both rings that a moonlet located about 100 km exterior to each ring could cause the optical depth variations seen in their occultation scans. This puts the moonlets orbiting outside the maximum radial extent of the rings due to their eccentricities (see Table 2.2), which are physically sensible locations.

We can estimate the mass of the moonlets based on the amplitude of the wakes using Equation (2) from Horn et al. (1996),

$$\tau(r,\theta) = \frac{\tau_0(a)}{1 + 2.24 j \mu \eta_0 \theta \cos(\eta\theta)(a_s/s)^4}, \tag{2.4}$$

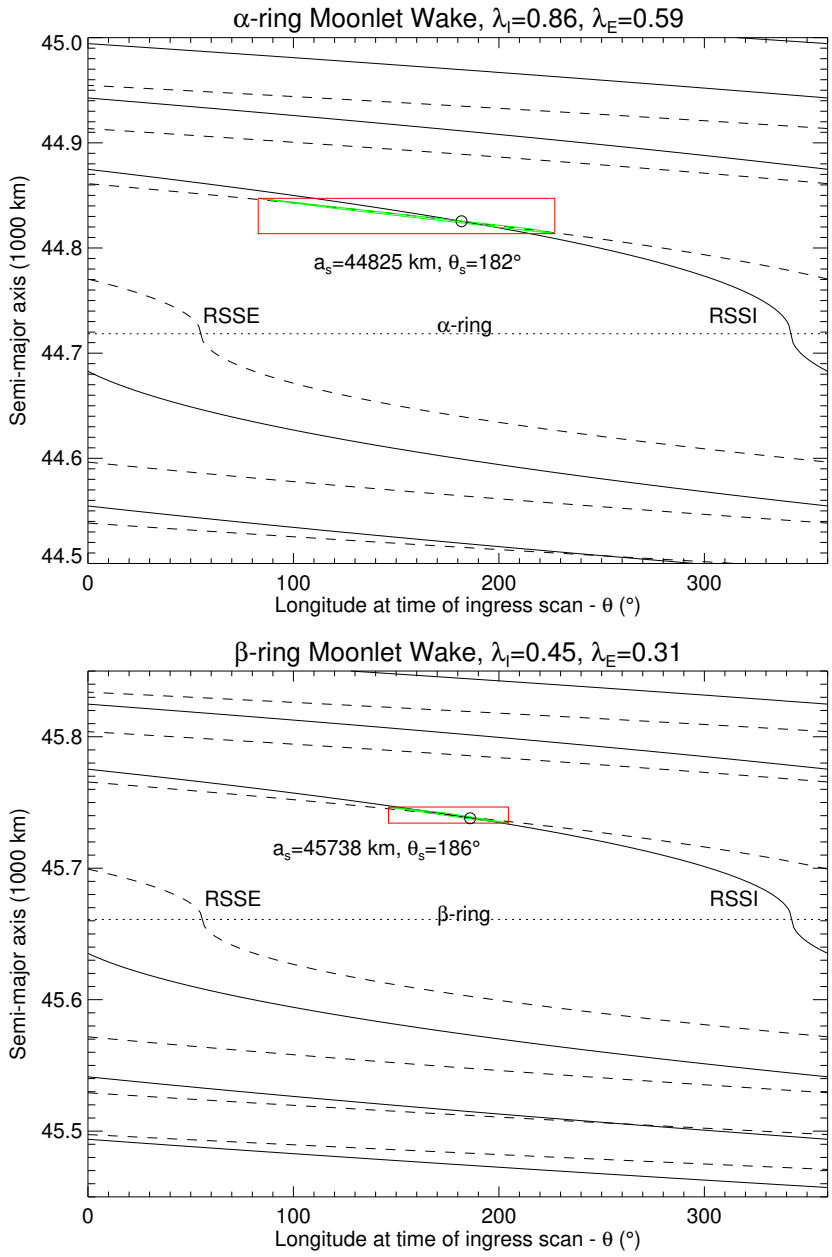

Figure 2.6: Location of the α (top) and β (bottom) moonlet determined by plotting the curves of Equation 2.3 shifted into the time frame of the RSS ingress occultation with the ingress and egress wavelengths of Table 2.3. A moonlet located where the ingress (solid) and egress (dashed) curves cross, labeled with a circle, would be able to produce the optical depth variations seen in both scans. The red box outlines the maximum extent of the uncertainties in a and θ, although this exaggerates the actual range in uncertainties for the location, shown as the very narrow green parallelogram-shaped area resulting from calculations of all combinations of wavelength uncertainties. If we consider the bump in the Fourier spectrum of the α ingress scan at ~ 1 km, the location where the curves cross, as a result of this larger wavelength, moves to a smaller semimajor axis, resulting in a moonlet slightly closer to the ring with a smaller radius (~ 2 km).

Table 2.4: Moonlet masses and radii

Ring	τ_{peakI}	τ_{0I}	τ_{peakE}	τ_{0E}	M_{sI} (kg)[a]	M_{sE} (kg)[a]	R_{sI} (km)[b]	R_{sE} (km)[b]
α	0.51[c]	0.72	1.88	1.52	$(3^{+4}_{-2}) \times 10^{14}$	$(1.0^{+18}_{-0.6}) \times 10^{14}$	4 ± 1	3^{+4}_{-1}
β	1.16	0.83	0.70	0.45	$(0.5^{+0.3}_{-0.2}) \times 10^{14}$	$(0.7^{+0.4}_{-0.2}) \times 10^{14}$	$2.1^{+0.4}_{-0.2}$	$2.4^{+0.6}_{-0.3}$

[a] Mass uncertainties are the extremes resulting from all combinations of input locations and their uncertainties. Note that the asymmetry of these error bars is due to the factor of s^4 in Equation 2.6.

[b] Radius uncertainties as above with uncertain mass inputs.

[c] τ_{peakI} is less than τ_{0I} for α because in the case of the α ingress occultation we used the optical depth dips instead of peaks; thus, the $\cos(\eta\theta)$ term in Equation 2.4 goes to -1.
Moonlet masses for each ring are determined from the optical depth variations and longitudinal separations of the ingress and egress occultation scans using Equation 2.6. Moonlet radii are calculated from the average mass of the ingress and egress scans using an estimated density of 1.3 g/cm^3.

where τ is the observed ring optical depth, τ_0 is the average (unperturbed) optical depth, j is +1 for a moonlet interior to the ring and -1 otherwise, μ is the ratio of the satellite and planet masses, and η_0 and η are azimuthal wave numbers defined in Showalter et al. (1986) such that

$$\eta = \frac{\eta_0 a_s}{s} + \eta_1 + \cdots = \frac{-\frac{2}{3} + \frac{5}{3} J_2 \left(\frac{r_p}{a_s}\right)^2 + \cdots}{s/a_s} + \frac{1}{6} + \ldots \tag{2.5}$$

The mass of the satellite can therefore be calculated as

$$M_s = \frac{M_p(\tau_0/\tau_{peak} - 1)}{2.24 j \eta_0 \theta (a_s/s)^4}, \tag{2.6}$$

where τ_{peak} is the peak (or trough) optical depth value (allowing us to reduce $\cos(\eta\theta)$ to 1 [or -1] for simplicity). While this formula may not be perfectly accurate for wakes on an eccentric ringlet, it can still provide a useful rough estimate of the moons' masses. Masses are calculated using the τ_0 and τ_{peak} of each occultation and their corresponding azimuthal separations, θ, which are determined from the difference in the moonlet's inertial longitude and the occultation geometry longitudes of Table 2.1. Table 2.4 lists the calculated moonlet masses for the two occultations and their approximate radii calculated using an assumed typical inner Uranian moon density[2] of 1.3 g/cm^3. We find that for both the α and β rings the perturbing moonlet is on the order of 10^{14} kg and $\sim 2 - 7$ km in radius, that is, less than 2% of the mass and $\sim 20\%$ of the radius of Cordelia.

2.6 Image analysis

We can attempt to find the moonlets in the *Voyager 2* images using the location estimates from the previous section. The narrow- and wide-angle camera images used for this search were obtained from the Imaging Science Subsystem on board *Voyager 2*. The images are geometrically corrected and

[2] http://ssd.jpl.nasa.gov/?sat_phys_par

Table 2.5: α and β ring imaging data

Ring	Image Name GEOMED.IMG	Mid-time (hr:min:s)	Phase angle (deg)	λ_{range} (deg)	λ_s (deg)
α	C2675402	14:55:58	15.31	99.90 - 151.23	108.44
	C2675408	15:00:46	15.29	97.85 - 150.17	112.62
	C2675438	15:24:46	15.30	98.29 - 149.95	133.57
	C2675456	15:39:10	15.36	102.82 - 151.65	146.13
	C2676225	21:38:22	15.45	97.59 - 147.87	99.59
	C2676231	21:43:10	15.43	95.05 - 146.34	103.78
	C2676243	21:52:46	15.51	101.89 - 150.68	112.16
	C2676249	21:57:34	15.49	99.73 - 149.85	116.34
	C2676255	22:02:22	15.47	97.72 - 148.93	120.53
	C2676301	22:07:10	15.44	95.22 - 147.61	124.72
	C2676313	22:16:46	15.52	101.87 - 150.54	133.10
	C2676319	22:21:34	15.49	99.09 - 150.01	137.29
	C2676331	22:31:10	15.44	94.43 - 146.24	145.67
	C2678913	19:04:46	16.58	117.28 - 149.23	142.17
β	C2675108	12:36:46	15.26	100.23 - 153.61	118.05
	C2675114	12:41:34	15.34	107.84 - 158.21	122.11
	C2675120	12:46:22	15.26	100.60 - 155.59	126.18
	C2675126	12:51:10	15.35	108.40 - 156.86	130.24
	C2675132	12:55:58	15.25	98.66 - 151.08	134.30
	C2675138	13:00:46	15.34	106.06 - 153.25	138.37
	C2675144	13:05:34	15.26	99.65 - 150.67	142.43
	C2675150	13:10:22	15.32	104.20 - 153.03	146.50
	C2675156	13:15:10	15.30	102.78 - 152.54	150.56
	C2675933	19:20:46	15.39	97.27 - 149.06	100.10

Images used in Figure 2.7. Image mid-times listed are in time after UTC 1986 January 21 00:00:00. The longitudinal scale is $\sim 0.08^\circ$ pixel^{-1}, and the radial scale is ~ 65 km pixel^{-1}. The table also includes the phase angle and range of inertial longitudes, λ_{range}, of each image. The longitude, λ_s, refers to the expected location of the moonlet in each image based on the location in Table 2.3.

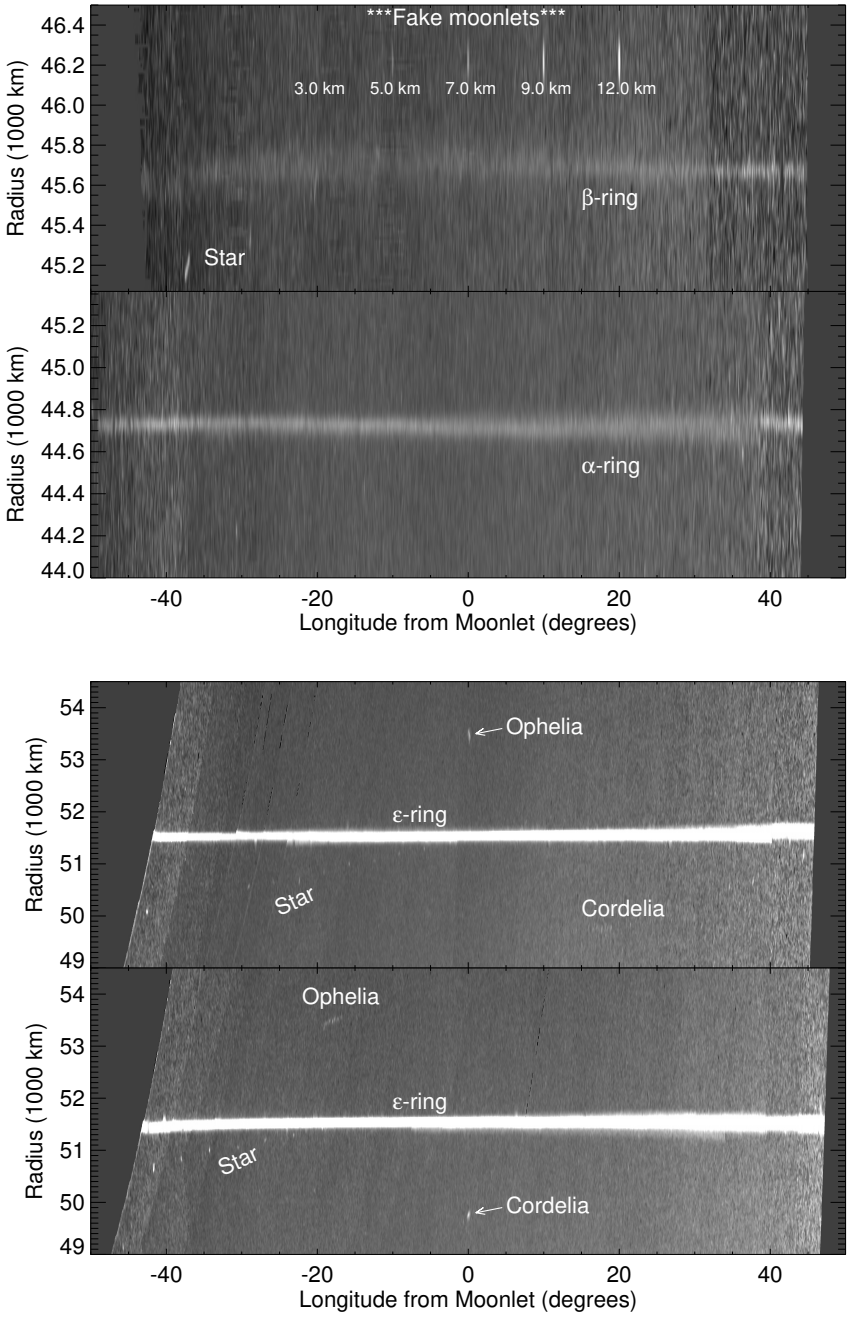

Figure 2.7: Mosaics of the β and α rings' images (top) that contain inertial longitudes within range of the predicted moonlet locations. We see no strong evidence of a moonlet just outside the β or α rings. If a moonlet were present, it would be located roughly between one and two vertical scale tick marks exterior to the rings and be roughly as bright as the 3.0 km radius fake moonlet we have inserted in the uppermost mosaic. The bottom two mosaics are a test of this technique on known moons Ophelia and Cordelia (each $\sim$ 20 km in radius). Each of these mosaics also shows the other moon drifting by due to their different mean motions, as well as a background star drifting through the images.

calibrated as documented on the PDS. Table 2.5 lists the images we chose for the mosaics, which contain inertial longitudes within the range of the expected moonlet locations and neglecting images containing significant defects. We re-project these images onto a corotating radius longitude grid (assuming moonlet mean motions of 1219.18°/day for β and 1256.66°/day for α) and co-add pixels of the appropriate images shifted such that the possible pixels of the moonlet in each image are stacked on top of one another at 0° longitude, although it could be up to several tens of degrees from this location (possibly more for the α moonlet). These mosaics, shown in Figure 2.7, do not show any clear evidence of a moonlet near the expected locations. We have verified that our codes do work for the known moons Cordelia and Ophelia (see bottom panel of Figure 2.7).

Using the moonlet radii of Table 2.4, we can determine whether the putative moonlets are too small and dim to be seen in the *Voyager* images. Assuming a geometric albedo of 0.07 (Karkoschka, 2001a), we can compute the expected brightness of moons with various sizes. At the top of Figure 2.7 we show the expected signals from moons of various radii. The fake 3.0 km moonlet is nearly indistinguishable from the many other noise features throughout the mosaic. We therefore conclude that moons with radii between 2 and 4 km are near the noise limit of the *Voyager 2* images, and so it is not surprising that the moons are not easily seen in these data. We caution the reader to appreciate the uncertainties that arise when determining the point where two square root functions intersect, and so there is substantial uncertainty in the longitudes of the moons, complicating the efforts to locate the moons in images.

2.7 Discussion

Our attempts to visually detect the moonlets are not exhaustive, but given the small predicted sizes of the α and β moonlets, a convincing detection may not be possible in the *Voyager 2* images. Future earth-based observations may be more likely to detect these moons. Regardless of the current lack of visual detection, the identification of these periodic structures in the outer regions of the α and β rings is evidence of interactions with nearby perturbers.

With their analysis of the resonances of Cordelia and Ophelia and the shepherding of the ϵ ring, Goldreich & Porco (1987) theorized that a single moon, smaller than in the standard shepherding model, orbiting near a ring edge could keep the ring confined using a mechanism called angular momentum flux reversal. The theory of this mechanism, outlined in Borderies et al. (1986), says that satellite perturbations can reverse the direction of the vicious flux of angular momentum and could possibly act over the entire width of narrow rings. Lewis et al. (2011) simulated this effect and found that collisional damping of satellite wakes caused by a small moon could keep a narrow ring confined under the right conditions. Further studies need to be done to determine whether the moonlet masses and locations found in our study are able to confine the rings.

2.8 Acknowledgements

...as they appear in the official publication.

This work was supported by the NASA Solar Systems Workings program grant NNX15AH45G. We would like to thank Mark Showalter for his valuable insights on the detection of the proposed moonlets

and Richard French for several discussions concerning the *Voyager 2* occultation observations and updates on the Uranian ring orbital elements. We also thank Wes Fraser for his helpful review to improve this manuscript.

Chapter 3: Weighing Uranus' moon Cressida with the η ring

Chancia, R.O., Hedman, M.M., French, R.G. "Weighing Uranus' moon Cressida with the η ring" *The Astronomical Journal, 154, 153, 2017*

For this project I developed a routine to fit normal mode radial oscillations in the Uranian rings using over 30 years of ground-based and spacecraft occultation data. The goal of this work was to search for new modes, previously undetected in studies of smaller data sets, and to remove the effects of the known dominant modes and search for weaker structures in the residuals that might be connected to resonances with moons. I quickly found the known $m = 1$ mode of the ϵ, α, β, 4, 5, and 6 rings, the $m = 2$ of δ, and $m = 0$ and $m = 1$ for γ. The η ring is nearly circular and has never been fit well by anything but a low eccentricity $m = 1$ mode. η, along with δ and γ also had the largest remaining radial residuals, so they were targets to search for previously untested or undiscovered modes.

After searching these rings for normal modes with all $|m| < 25$ I found that an $m = 3$ structure for the η ring stood out. Looking back into the literature, I found that Porco & Goldreich (1987); Goldreich & Porco (1987) reported on the 3:2 inner Lindblad resonance (ILR) with the moon Cressida located a few kilometers interior to the η ring where it was unlikely to effect the ring. No other mentions of this resonance exist in the literature. After plotting the radial variations in a longitude system relative to the longitude of Cressida we found that the low amplitude $m = 3$ structure's pericenter was in fact aligned with Cressida as the ring dynamics would suggest. I then calculated the mass and density of Cressida using the theoretical formulations of resonant ring dynamics where the primary inputs are the ring's radial oscillation amplitude and radial distance from the exact resonance. This resulted in a reasonable result for the small moon's mass and density. Next, I determined the expected radial amplitude produced by all possible 1st-order Lindblad resonances likely to affect the Uranian rings to better assess where this particular resonance stood among them. Under the speculated range of possible moon masses, the Cressida 3:2 ILR should actually be the strongest resonance affecting any of the Uranian rings. This calculation also points to the resonances on either edge of the ϵ ring as being the next likely target of investigation. The other resonances should produce radial oscillations with amplitudes approaching the noise level of the occultation data, and are much less likely to be detected.

Our measurement of Cressida's mass is the first of any of the thirteen small inner Uranian moons. The measured density is notably lower than previous estimates, possibly pointing to the dark ring material being primarily water ice with just a thin veneer of unknown dark material. This measurement has significant consequence for the dynamical stability of the tightly packed Uranian moon system. The system is expected to be unstable on short timescales compared to the age of the solar system.

3.1 Abstract

The η ring is one of the narrow rings of Uranus, consisting of a dense core that is 1-2 km wide and a diffuse outer sheet spanning about 40 km. Its dense core lies just exterior to the 3:2 Inner Lindblad Resonance of the small moon Cressida. We fit the η ring radius residuals and longitudes from a complete set of both ground-based and Voyager stellar and radio occultations of the Uranian rings spanning 1977-2002. We find variations in the radial position of the η ring that are likely generated by this resonance, and take the form of a 3-lobed structure rotating at an angular rate equal to the mean motion of the moon Cressida. The amplitude of these radial oscillations is 0.667 ± 0.113 km, which is consistent with the expected shape due to the perturbations from Cressida. The magnitude of these variations provides the first measurement of the mass and density of the moon Cressida ($m = 2.5 \pm 0.4 \times 10^{17}$ kg and $\rho = 0.86 \pm 0.16$ g/cm^3) or, indeed, any of Uranus' small inner moons. A better grasp of inner Uranian satellite masses will provide another clue to the composition, dynamical stability, and history of Uranus' tightly packed system of small moons.

3.2 Introduction

In March of 1977, Elliot et al. (1977a), Millis et al. (1977), and Bhattacharyya & Kuppuswamy (1977) discovered nine narrow rings around the planet Uranus by measuring the light blocked by each ring before and after Uranus occulted the star SAO158687. Since then, the Uranian rings have been studied extensively with ground based stellar occultations (Millis & Wasserman, 1978; Nicholson et al., 1978; Elliot et al., 1981b,a; Nicholson et al., 1981; French et al., 1982; Sicardy et al., 1982; Elliot et al., 1983, 1984; French et al., 1986b,a; Elliot et al., 1987; French et al., 1988, 1996). Occultations provide very precise radial locations of the rings at different longitudes in their orbits around Uranus. French et al. (1988) found that the main rings of Uranus consist of six measurably eccentric rings (6, 5, 4, α, β, and ϵ) and three nearly circular rings (η, γ, and δ). In the past, measurements of the η ring's radius have not shown the ring to be anything but circular. The η ring also features a broad low optical depth sheet extending approximately 40 km exterior to its narrow core (Elliot et al., 1983).

During the Voyager 2 flyby of Uranus Smith et al. (1986) discovered ten new small inner moons, but no one has ever measured their masses or densities. Nine of the moons orbit within a radial range of 20,000 km, making the group one of the most tightly packed systems of interacting satellites in our solar system. Lissauer (1995) estimated the masses of the inner moons assuming densities equal to that of the larger moon Miranda (Jacobson et al., 1992) and shapes estimated with photometry (Thomas et al., 1989), but stated that at least some of Uranus' small inner moons are significantly less massive than these estimates. The lifetime of this system is highly sensitive to the masses of the individual satellites (French et al., 2015). In fact, prior to the knowledge of the even less stable moon Cupid (Showalter & Lissauer, 2003; French & Showalter, 2012), Duncan & Lissauer (1997) showed that Desdemona could collide with either Cressida or Juliet within the next $4 - 100$ million years, depending on the masses of the satellites involved. The discovery of the dusty ν and μ rings (Showalter & Lissauer, 2006), near the orbits of Portia/Rosalind and Mab respectively, hints at the possibility of an evolving inner ring-moon

system dominated by accretion (Tiscareno et al., 2013). Kumar et al. (2015) also argue that anomalies in Mab's orbital motion may be explained by a ring-moon system that is undergoing re-accretion after a recent catastrophic disruption.

Here we investigate a complete set of Uranian η ring occultation observations spanning their discovery in 1977 to 2002. We find that the η ring's radii exhibit a 3-lobed structure rotating around Uranus at the mean motion of the moon Cressida. We argue that this structure is a result of the η ring's close proximity to Cressida's 3:2 inner Lindblad resonance (ILR). One of the maxima in the ring's radius aligns with Cressida, as expected for the stable ring structure located exterior to the resonant radius. The measured radial amplitude of this ring structure and its distance from the resonance allow us to estimate Cressida's mass, and thus obtain the first gravity-based mass measurement of any inner Uranian moon.

We have only been able to find three previous mentions of the Cressida 3:2 ILR and its association with the η ring. Porco & Goldreich (1987) identified the most relevant resonances in the Uranian ring-moon system and made a case for Cordelia and Ophelia shepherding the outermost ϵ ring through torques generated by the Lindblad resonances located appropriately on the ring's inner and outer edges (Goldreich & Porco, 1987). They also note single resonances that could be perturbing the γ and δ rings. Finally, they state: "The only isolated first-order satellite resonances which fall near any of the remaining rings are located interior to the η ring." Porco & Goldreich (1987) list both the Cressida 3:2 and the Cordelia 13:12 resonances, located at $a = 47171.6 \pm 0.3$ km and $a = 47173.0 \pm 0.3$ km respectively. These resonances fall $3 - 5$ km interior to the η ring. They calculate the widths of both resonances to be ~ 1 km and dismiss the possibility that either resonances is perturbing the η ring. Murray & Thompson (1988) later marked the location of the Cressida 3:2 ILR in their figure displaying a radial scan of a high phase image of the Uranian rings acquired by Voyager 2. Subsequently, Murray & Thompson (1990) noted that this resonance needs to be re-examined using updated satellite parameters. At the time, with a smaller data set, there was no detection of either an $m = 3$ or an $m = 13$ mode in the η ring, nor any other modes due to resonances with known satellites having observed effects on any of the other previously noted rings' edges (French et al., 1988). Thus, it was only sensible to dismiss these resonances, and it is reasonable that they have not been of interest since. We are only able to make this discovery now because we have a larger set of occultation data extending from 1977 through 2002.

We present the data used in this analysis in Section 2, and describe our ring particle streamline model and our mode detection methods in Section 3. In Section 4, we report the parameters of our fit to the η ring and calculate the mass and density of Cressida. Finally in Section 5, we discuss potential implications for the dynamical stability of the tightly packed system of inner Uranian moons and the possible composition of Cressida.

3.3 Observational Data

The observational data used for this analysis consist of 49 individual occultation observations of the η ring. In the appendix, Table C.1 contains each occultation's ring intercept time, inertial longitude, and mid-radius determined using a simple square-well model for profile fitting, developed by Elliot et al. (1984) and used in later orbit determinations of the Uranian rings (French et al., 1986b,a, 1988, 1991). Of

these 49 observations, 46 are Earth-based stellar occultations, two are Voyager 2 Radio Science Subsystem (RSS) radio occultations, and one is a Voyager 2 Photopolarimeter Subsystem (PPS) stellar occultation. Several of the observations are ingress and egress pairs from the same occultation of Uranus and its rings.

For each Earth-based occultation, an instrument recorded the brightness of the background star as a function of time. As the Earth moves relative to Uranus the rings can block the star's light, leaving each ring's mark as a sharp decrease in the recorded brightness of the star for some amount of time related to the width of the ring. Typically the observations were detected with an InSb photometer in the 2.2 μm band, using the K filter, where Uranus is fainter than the rings. Most observations provided limited information about the radial structure within the rings, and here we are making use only of the estimate of the radius of the mid-point of each ring occultation profile. Interested readers should see Elliot (1979) for a review of stellar occultation studies of the solar system and Elliot & Nicholson (1984) for a review of this observation method specific to the rings of Uranus.

To identify possible Uranus occultation opportunities Taylor (1973) compared positions of Uranus to stellar positions in the Smithsonian Astrophysical Observatory (SAO) catalog. Once the rings were discovered, it became more appropriate to utilize dimmer stars that are bright in the 2.2 μm band. Thus, Klemola & Marsden (1977) searched for stars on photographic plates containing star fields ahead of Uranus and created a list of ideal future occultation observations. Additional lists of this type were compiled by Klemola et al. (1981), Mink & Klemola (1982, 1985), Nicholson et al. (1988), and Klemola & Mink (1991).

The Voyager 2 PPS stellar occultation only detected the η ring on egress (Lane et al., 1986; Colwell et al., 1990). In the case of the Voyager 2 RSS occultations, the RSS instrument illuminated the rings at 3.6 cm and 13 cm wavelengths in the direction of Earth once beyond the ring plane. Stations on Earth detected the diffracted signal and relative phase change, to later be reconstructed into high-resolution radial optical depth profiles after the removal of diffraction effects (Tyler et al., 1986; Gresh et al., 1989). Presently, ground based occultation opportunities are rare because Uranus has passed out of the dense Milky Way background, drastically reducing the density of appropriate background stars. The rings are also no longer as open to our view from Earth as they were in the 1980s because the apparent aspect of the ring plane as viewed from Earth changes over time.

3.4 Ring Particle Streamline Model and Fitting Method

The procedure used here follows that of French et al. (1986b, 1988, 1991) for the Uranian rings, more recently employed by Hedman et al. (2010b), Nicholson et al. (2014a,b), and French et al. (2016b) for analyses of Saturn's non-circular narrow rings, gaps, and edges. After taking account any inclination relative to the equatorial plane, the majority of narrow rings are well-fit by simple precessing Keplarian ellipses whose radii are described by:

$$r(\lambda, t) = \frac{a(1-e^2)}{1+e\cos f}, \tag{3.1}$$

where the true anomaly $f = \lambda - \varpi_0 - \dot{\varpi}(t-t_0)$. Here, the radius of the ring will vary with longitude λ and time t, where a and e are the ring's semi-major axis and eccentricty, ϖ_0 is the ring's longitude of periapsis at the time t_0, and $\dot{\varpi}$ is the ring's apsidal precession rate. We can approximate a nearly circular

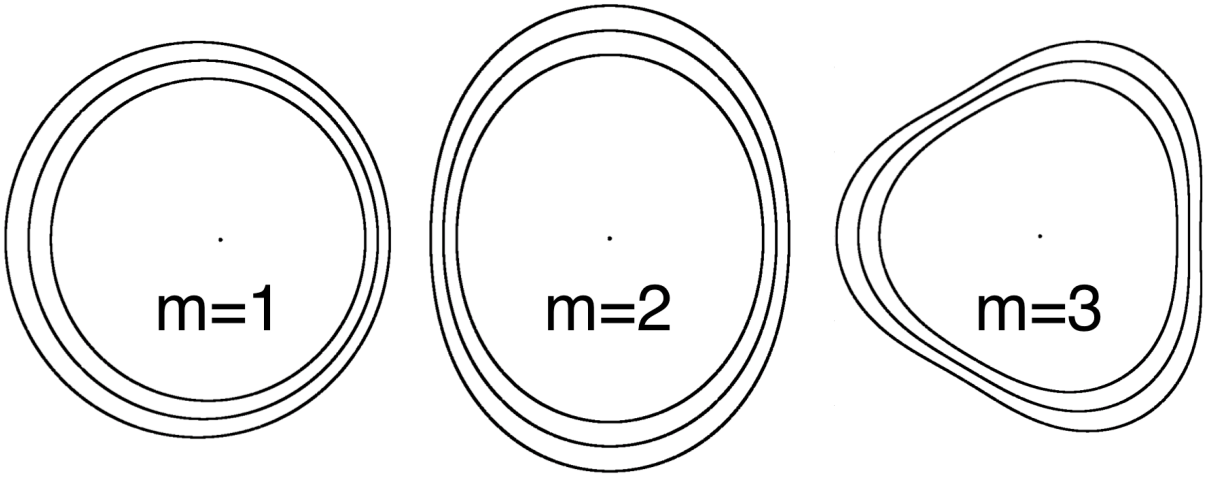

Figure 3.1: The above shapes are an exaggerated representation of the m-lobed ring streamlines we detect in the Uranian rings. For each case of m, we have shown 3 streamlines with slightly different semi-major axes and a positive eccentricity gradient. Our addition of an eccentricity gradient results in a narrower ring width at periapsis, as is the case for several of the Uranian rings.

($e \simeq 0$) ring's radii as $r \simeq a(1 - e\cos f)$.

Additionally, several rings are found to contain forced radial oscillations and in a few cases there are even rings whose structure is dominated by free normal mode oscillations. In these cases, the structures are distinct from circles or ellipses and their radii are described by:

$$r(\lambda, t) \simeq a - A_m \cos(m\theta), \tag{3.2}$$

where $\theta = \lambda - \Omega_p(t - t_0) - \delta_m$, following the formalism of Nicholson et al. (2014a,b) and French et al. (2016a). Here, the systematic radial oscillations of the rings form a $m-$lobed figure rotating around their planet at a pattern speed Ω_p with a radial amplitude A_m and phase δ_m. We show some exaggerated models of m-lobed ring streamlines, resulting from both free normal modes and Lindblad resonances, in Figure 3.1. While individual particles follow normal elliptical orbits, described by Equation 3.1, the ring as a whole consists of streamlines with m azimuthally symmetric radial minima and maxima rotating around the planet with the frequency

$$\Omega_p \simeq \frac{(m-1)n + \dot{\varpi}_{sec}}{m}. \tag{3.3}$$

Here, the mean motion n and apsidal precession rate $\dot{\varpi}_{sec}$ are functions of the semi-major axis a of the ring, and m can be any positive or negative integer. If we consider the case of $m = 1$ we find that $\Omega_p = \dot{\varpi}_{sec}$, $A_1 = ae$, and $\delta_1 = \varpi_0$, so that r is equivalent to the approximation of Equation 3.1 above.

In the case of a free normal mode oscillation, the pattern speed will be equal to the expected pattern speed obtained by evaluating Equation 3.3 at the semi-major axis of the ring. However, if the ring is perturbed by a satellite through a first-order Lindblad resonance, then the ring structure will have a

forced pattern speed matching the mean motion of the perturbing satellite $n_s = \Omega_p$ and will differ from the expected pattern speed slightly based on the ring's separation from the exact radius of the resonance $|a - a_{res}|$. The ring is perturbed by the satellite due to the near commensurate ratio of the ring particles' orbital periods and the period of the perturbing satellite. As such, first-order Lindblad resonances are defined by $|m| : |m - 1|$, where for every $|m|$ orbits of the ring particle, there are $|m - 1|$ orbits of the corresponding satellite. In the majority of cases, the perturbing satellite lies at a larger semi-major axis than the ring ($a_s > a$). The relevant resonances in this case are called inner Lindblad resonances (ILR) and are assigned positive values of m. In the rare case of a satellite located interior to the rings it is possible to have both ILR and outer Lindblad resonances (OLR) at locations within the rings, allowing for negative values of m.

The condition for a first-order Lindblad resonance is that the resonant argument:

$$\varphi = m(\lambda - \lambda_s) - (\lambda - \varpi) \tag{3.4}$$

is constant in time. Here λ and λ_s refer to the longitudes of a ring particle and the satellite respectively and ϖ is the longitude of periapsis of the ring particle. If we consider a conjunction of the ring particle and the satellite ($\lambda - \lambda_s = 0$) occurring when the ring particle is also located at its longitude of periapsis ($\lambda - \varpi = 0$), then the condition that φ is constant implies that all future conjunctions will occur when the ring particle is near periapsis. In general, this means that the ring particle will always be in the same phase of its orbit when it passes longitudinally close to the satellite. This allows the perturbing satellite to force the eccentricity and periapsis locations of streamlines located near the resonance. In Figure 3.2 we show a cartoon model of the resulting streamlines surrounding a 3:2 ILR in the co-rotating frame of the perturbing satellite. Interior (exterior) to the resonant radius, marked with the dashed line, the streamlines are stable when oriented such that one of the three periapses (apoapses) is aligned with the satellite.

In short, our procedure is a search for patterns in the varying mid-radii measurements of the rings. Each ring occultation observation provides the ring's radius at a particular longitude and time. To search for patterns in each ring we need the observed parameters, an m value to test, and the resulting expected pattern speeds for that m value. For each test of m, we compute the expected patten speed for the semi-major axis of the ring using Equation 3.3 and create an array of $100,000$ pattern speeds, evenly spaced in increments of $0.00001°$/day, surrounding the expected pattern speed. Using each pattern speed we calculate $m\theta$, for every ring observations' longitude λ and time t, using an initial epoch time t_0 of UTC 1977 MAR 10 20:00:00.00. We can then compute the observed ring radii r vs. $m\theta$ mod 360° and fit the data to a single sinusoid. The resulting fit parameters are a, A_m, and δ_m, allowing us to compute model values of r using Equation 3.2. We compute the RMS deviation of the observed radii and the model radii for each m's $100,000$ test pattern speeds and look for a RMS minimum to identify the best fitting pattern speed.

We first checked our algorithms by searching for known structures in the Uranian rings. In several rings ($6, 5, 4, \alpha, \beta$, and ϵ) we can easily detect RMS deviations that drop to nearly zero (sub-km) with the proper pattern speed and m input. These are the rings that largely follow classical Keplerian ellipses

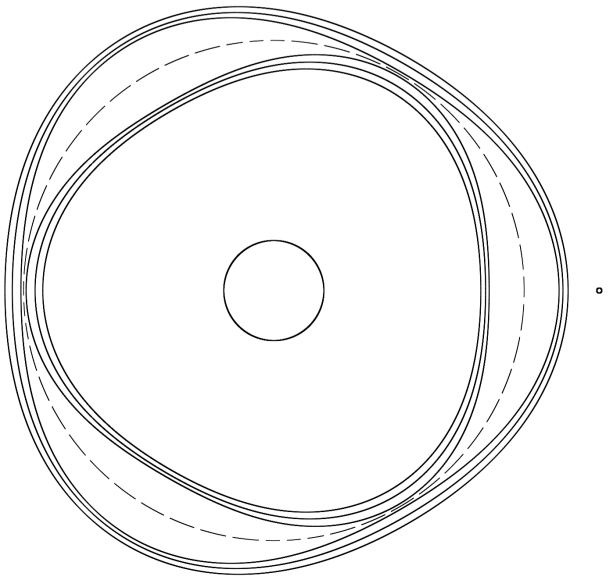

Figure 3.2: An exaggerated cartoon model of ring particle streamlines around a planet and near a 3:2 ILR with an exterior moon, in the co-rotating frame of the moon. We've marked the resonant radius with a dashed line and included three ring particle streamlines on either side of the resonance. This shows the stable configuration on either side of the resonance, where a periapse (apoapse) is aligned with the moon interior (exterior) to the resonance.

($m = 1$) and whose pattern speeds equal the rings' apsidal precession rate, $\Omega_p = \dot{\varpi}_{sec}$. The η, γ, and δ rings are nearly circular and their residuals are relatively larger when fit with a low amplitude $m = 1$ ellipse. We are also able to identify the known $m = 2$ structure of the δ ring and the combination of $m = 0$ and $m = 1$ for the γ ring (French et al., 1986b).

We decided to identify the strongest resonances in the Uranian rings to have a better idea of the resonantly forced modes that are the most likely to be detected. To quantify the 'strength' of the resonances in the system we chose to compare the expected forced radial amplitude on rings near each of the possible resonances in the main ring system. We use Equation 10.22 from Chapter 10 of Murray & Dermott (1999),

$$A_m = \frac{2\alpha a^2 (m_s/m_p)|f_d|}{3(j-1)|a - a_{res}|} \tag{3.5}$$

where A_m is the forced radial amplitude of a ring particle in the vicinity of a Lindblad resonance (Porco & Nicholson, 1987; Goldreich & Tremaine, 1982). This amplitude is a function of the ratio of the perturbing satellite and central planet masses m_s/m_p, the radial separation of the ring and the resonance $|a - a_{res}|$, the ratio of the ring and satellite semi-major axes $\alpha = a/a_s$, and the Laplace factor f_d, that depends on j, the integer coefficient of the satellites longitude in the resonant argument, which is equivalent to m in the case of a first-order Lindblad resonance. As shown in Figure 10.10 of Murray & Dermott (1999), $\frac{2\alpha|f_d|}{j-1}$ varies between 1.5 and 1.6, depending on j. Note that Equation 3.5 isn't necessarily applicable for all cases. If $|a - a_{res}|$ is smaller than the resonance half-width, then A_m calculated using Equation 3.5 is not a good estimation of the radial amplitude produced by the resonance because in this regime

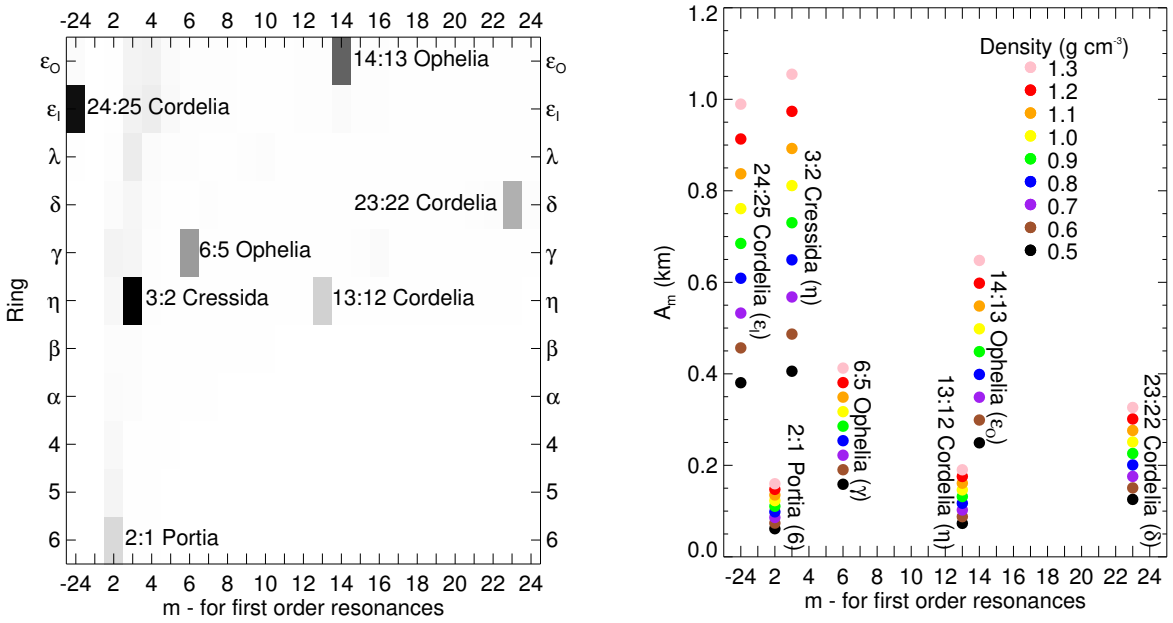

Figure 3.3: The left mosaic shows the relative forced amplitude (darker = larger amplitude) of all first-order resonances of inner moons out to Perdita interacting with the Uranian rings assuming the moons each have a density of 1.3 g/cm^3. The largest amplitude resonances are labeled, while the fainter patches in the mosaic are evidence of resonances within the system that do not fall close enough to any rings and would have much smaller amplitudes. The actual values of the significant resonances are plotted on the right side to compare with the mosaic, but with the addition of a range of moon densities (0.5 to 1.3 g/cm^3), calculated using Equation 3.5.

neighboring streamlines will cross and collisional dissipation cannot be ignored.

In Figure 3.3 we display the forced amplitude on all 10 rings (inner and outer edges for the ϵ ring) due to all possible first-order Lindblad resonances of all Uranian moons out to Perdita. For the estimated mass of each moon, we use the radius measurements of Karkoschka (2001b) and Showalter & Lissauer (2006) and consider a range of densities from 0.5 to 1.3 g/cm^3. In the left half of Figure 3.3 all resonances mentioned by Porco & Goldreich (1987) are apparent in addition to a previously unexplored 2:1 ILR with Portia in the proximity of the 6 ring. In the right side of Figure 3.3 we compare the amplitudes of the strongest resonances over a range of moon densities. The fainter patches in the left side of Figure 3.3 are due to resonances inducing much weaker amplitudes due to their large distance from the rings. Despite the separation in semi-major axis of the η ring from the Cressida 3:2 ILR the η ring is expected to be the most perturbed of all the Uranian rings in this framework. The next largest expected amplitudes are the Cordelia 24:25 OLR and the Ophelia 14:13 ILR that are thought to play a roll in shepherding the ϵ ring. If this is a realistic estimation of the strength of the resonances in the system, in the future we may be able to detect the $m = -24$ mode on the inner edge of the ϵ ring, which was previously detected by French & Nicholson (1995) with occultation data and by Showalter (2011) with images showing the ring's longitudinal brightness variations. Detecting the ϵ ring edge modes will first require determining the ring's edge positions and the removal of the larger amplitude $m = 1$ normal mode which dominates its structure. Our analysis of these ring residuals as well as those for the other rings, whose structure is dominated by previously known normal modes, is ongoing and will be presented in a subsequent publication.

3.5 Results

After searching mode values from $m = -25$ to 25 of all the rings, the strongest new feature we've found is an $m = 3$ structure of the η ring consistent with the expectations discussed above. In Figure 3.4 we show the shallow minimum in RMS for our η ring $m = 3$ fits. The top plot shows the RMS deviations of the model radii from the observed radii at each pattern speed for $m = 3$, zoomed in on the minimum. Listed are the best fitting pattern speed, the semi-major axis of the Cressida 3:2 ILR, and the expected pattern speed for an $m = 3$ normal mode marked by the dashed line. Note that the best fitting pattern speed and the expected pattern speed for the semi-major axis of the η ring are offset because this is not a normal mode oscillation, but is instead the effect of a resonance with a satellite whose perturbations force the pattern speed to match the satellite's mean motion. We further refine our best fit solution and formal errors by applying the best fit parameters (a, A_m, δ_m, and Ω_p) as a set of starting parameters for MPFIT, a non-linear least squares fitting IDL function (Markwardt, 2009). We've initially assumed an uncertainty of 1 km in each of the 49 observed radii of the η ring, but found a reduced chi-squared of $0.308 << 1$. We fit again to obtain the listed errors using the standard deviation per degree of freedom (σ/ν) as a rescaled uncertainty in our observed radii which better represents the error of these data. The bottom plot shows the best fitting model radius curve on top of the observed radial separations from the fit semi-major axis of the ring, $\Delta r = r - a$. We've listed the final fit parameters and chi-squared analysis in Table 3.1.

The best fitting pattern speed for this mode, 776.58208 $\pm$0.00169 °/day, is strikingly close to the

Table 3.1: η ring $m = 3$ best fit

Parameter	Final fit and scaled errors
a (km)	47176.447 ± 0.086
A_3 (km)	0.667 ± 0.113
δ_3 (°)	58.81 ± 6.12
Ω_p (°/day)	776.58208 ± 0.00169
$n_{Cressida}$ (°/day)	776.582789 ± 0.000059[a]
$n_{Cressida}$ (°/day)	776.582414 ± 0.000022[b]
$n_{Cressida}$ (°/day)	776.582447 ± 0.000022[c]
χ^2	13.861
χ^2/ν	0.308
σ/ν (km)	0.555
N	49
# of parameters	4

Listed on top are the four fit parameters and their formal 1-σ errors resulting from our final fit, where we have assumed an error of 0.555 km for each of the observed radii of the η ring. We also list three published mean motions of Cressida for comparison with our pattern speed. The chi-squared and reduced chi-squared below are from the initial fit assuming an error of 1 km for each radii. The unscaled errors of the parameters in the initial fit are roughly double the scaled errors from the final fit, in which we have used the standard deviation per degree of freedom as a universal error in the observed radii. The degrees of freedom $\nu = N - \#$ of fit parameters.

[a] From Showalter & Lissauer (2006)

[b] From Jacobson (1998)

[c] From Pascu et al. (1998)

published mean motion of Cressida, the fourth moon from Uranus. Most recently Showalter & Lissauer (2006) listed Cressida's mean motion as $776.582789 \pm 0.000059°$/day. All three of the measurements of Cressida's mean motion listed in Table 3.1 are well within the uncertainty of our detected pattern speed, supporting the proposed connection between this $m = 3$ structure of the η ring and Cressida.

To solidify that the $m = 3$ structure is real and is a result of perturbations from Cressida, we have inspected the alignment of the structure with Cressida. In this case, the η ring ($a = 47176.447$) is located exterior to the resonance ($a_{res} = 47171.51$), and the dynamical model predicts that one of the three outer radial extents should track the motion of Cressida. That is, as the $m = 3$ structure and Cressida both rotate around Uranus at $n_{Cressida} \simeq \Omega_p$ one of the apoapses is constantly aligned with Cressida. This can be confirmed by noting that the $m = 3$ structure has a phase offset $\delta_3 = 58.81 \pm 6.12°$ (this is the longitude of one of the 3 periapsis), which is roughly 60° offset from Cressida's longitude (359.50°) at the epoch of the fit. We show this alignment more precisely in Figure 3.5, where we have determined the offset of each occultation scan longitude relative to Cressida's longitude at the observation time,

Table 3.2: Mass and Density of Cressida

A_3 (km)	Radius (km)	a (km)	a_{res} (km)	$m_{Cressida}$ (kg)	$\rho_{Cressida}$ (g cm^{-3})
0.667 ± 0.113	41 ± 2	47176.447 ± 0.086	47171.51 ± 0.03	$2.5 \pm 0.4 \times 10^{17}$	0.86 ± 0.16

We list the variables needed to solve for the mass of Cressida using Equation 3.5. For the calculation of $m_{Cressida}$ we used $GM_{Uranus} = 5793951.3 \pm 4.4$ km^3 s^{-2} from Jacobson (2014) and $G = 6.67408 \pm 31 \times 10^{-11}$ m^3 kg^{-1} s^{-2} from `http://physics.nist.gov/cgi-bin/cuu/Value?bg`. Also note $\frac{2\alpha|f_d|}{j-1} \simeq 1.545$ when $j = m = 3$ for the case of the Cressida 3:2 ILR. The listed radius needed to calculate the density of Cressida comes from Voyager 2 photometry (Karkoschka, 2001b).

$|m|(\lambda - \lambda_{Cressida})$. The apoapse of the phase-wrapped structure lags the longitude of Cressida by only $6 \pm 11°$ (Cressida's longitude is 0° and the fit sinusoid's largest radial excursion occurs at 354°). This suggests that the perturbations on the η ring are due to its proximity to the 3:2 ILR with Cressida.

Perhaps the most significant result of this work, shown in Table 3.2, is a determination of Cressida's mass using Equation 3.5. Given $A_3 = 0.667 \pm 0.113$ km we find $m_{Cressida} = 2.5 \pm 0.4 \times 10^{17}$ kg. We use the effective radius for Cressida of 41 ± 2 km from Karkoschka (2001b) to calculate a density of 0.86 ± 0.16 g/cm^3 for Cressida.

For our purposes, the η ring is outside the width of Cressida's 3:2 ILR and the resulting estimation of A_m is reasonable, but we note that this is not necessarily the case for all of the other rings and resonances. Curious readers should note, to test the applicability of Equation 3.5, we've calculated a resonance half-width of ~ 3.5 km for Cressida's 3:2 ILR using Equation 10.23 from Murray & Dermott (1999) along with our newly determined mass of Cressida. The other relevant variable inputs can be found in Tables 3.1 and 3.2. This half-width is less than the 5 km separation of the resonance and ring, confirming we are justified in using Equation 3.5. Note that the ~ 1 km resonance half-width quoted in the introduction was estimated by Porco & Goldreich (1987) and results from an approximation of the resonance half-width equation as well as a different satellite mass.

3.6 Discussion

Since the Voyager 2 flyby of Uranus in 1986, several dynamicists have explored the stability of the inner Uranian moons. The moons Bianca, Cressida, Desdemona, Juliet, Portia, Rosalind, Cupid, Belinda, and Perdita are members of the most tightly packed system of moons in our solar system. Nicknamed the 'Portia group' for their largest member, these satellites are thought to be unstable on short timescales compared to the age of the solar system. The stability of the Portia group is known to be highly sensitive to the masses of the individual satellites (French et al., 2015), which are not well constrained. In fact, the mass we provide for Cressida is the first direct measurement of an inner Uranian satellite's mass. Past simulations (Duncan & Lissauer, 1997; French & Showalter, 2012; Quillen & French, 2014; French et al., 2015) have relied on treating a range of possible masses for the inner Uranian satellites and suggest that Cressida will cross orbits with Desdemona in under 10^6 years (French & Showalter, 2012), given our mass density. Incorporation of our mass for Cressida should further constrain the timescale of satellite orbit crossing (collisions) and allow a future work to determine the masses of some of the other satellites through their resonant interactions. Strictly speaking, our density measurement does not necessarily

represent a common density of the inner moons. However, a lower average satellite density will generally result in collisions occurring in the more distant future.

Karkoschka (2001a) and Dumas et al. (2003) detected a possible water ice absorption feature in Hubble Space Telescope near-infrared photometry of the largest inner moon Puck. Combining this with the previously mentioned size estimates has formed the presumption that Cressida and the other inner Uranian moons are likely composed of mostly water ice with at least a veneer or contamination of dark material to explain their low albedo and flat gray spectra. The range in densities of the larger Uranian moons, determined from mass (Jacobson et al., 1992) and radius (Thomas, 1988) measurements, have provided a presumed upper limit on the densities of the inner moons, usually with reference to the least dense major moon Miranda (1.214 ± 0.109 g/cm^3)[1]. In Figure 3.6 we plot our average density of Cressida versus radius along with other satellites in our solar system, after Hussmann et al. (2006). Cressida is about 50% denser than the inner icy moons of Saturn with comparable radii. It may be that Cressida, and the Uranian rings/moons in general, have either a lower porosity than these Saturnian analog or they have higher amounts of non-icy contaminants, as inferred by Tiscareno et al. (2013). The contamination of denser and darker material may not be as high as previously expected, but it is substantial regardless.

This analysis shows that there is still information about Uranus' rings and moons found in historical and ground based data. Still, the best means of obtaining the Uranian moon masses and compositions, determining the ultimate fate of the Portia group, and understanding the intricate structure of the rings is of course a Uranus orbiter mission.

3.7 Acknowledgements

...as they appear in the official publication.

We would like to thank Phil Nicholson for his insights regarding ring occultation observations and both Phil Nicholson and Pierre-Yves Longaretti for several fruitful discussions concerning the forced radial amplitudes of ring particles orbiting near Lindblad resonances. We'd also like to thank our anonymous reviewer for helpful suggestions and comments, ultimately improving the clarity of this work. This work was supported by the NASA Solar System Workings program grant NNX15AH45G.

[1] `https://ssd.jpl.nasa.gov/?sat_phys_par`

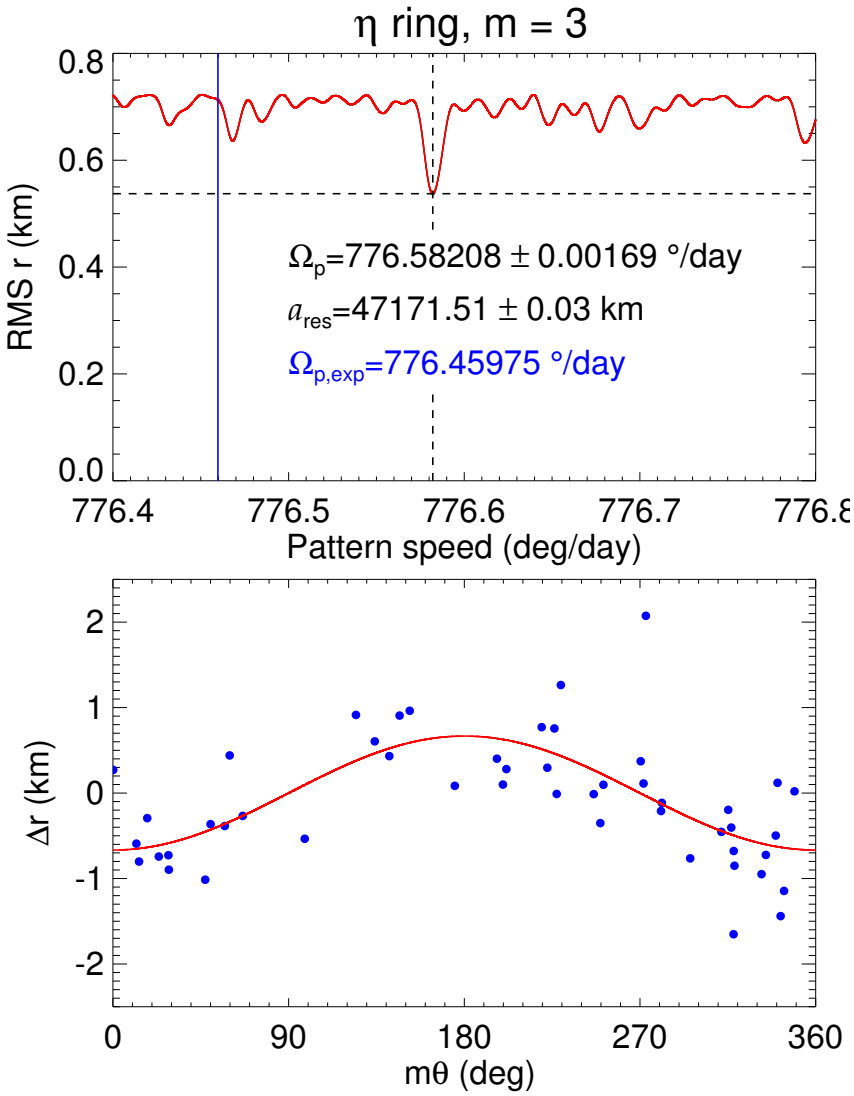

Figure 3.4: The upper plot shows the RMS deviations of the observed radii, r, and the model fit (Equation 3.2) for a range of pattern speeds, Ω_p. Listed in the top plot are the best fitting pattern speed and the corresponding radial location of the resonance, a_{res}. The blue line refers to the expected pattern speed for an $m = 3$ normal mode oscillation. The lower plot shows the best fitting model (red line) and observed radii plotted vs. $m\theta = m[\lambda - \Omega_p(t - t_0) - \delta_m]$ after subtracting the semi-major axis of the ring ($\Delta r = r - a$).

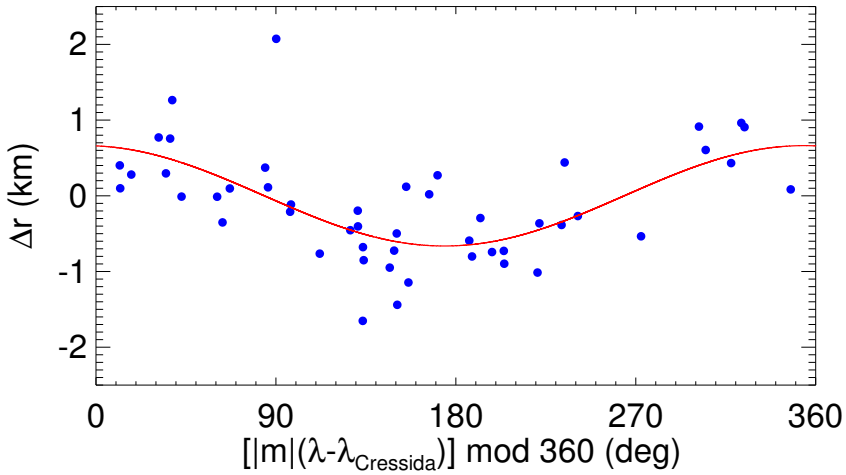

Figure 3.5: This plot shows the η ring structure in a reference frame tied to Cressida. One of the three outermost radial extents actually tracks Cressida, the others are located $\sim 120°$ apart. We obtained longitudes of Cressida at various times using the ura091.bsp and ura112.bsp SPICE kernels, available at `https://naif.jpl.nasa.gov/pub/naif/generic_kernels/spk/satellites/`.

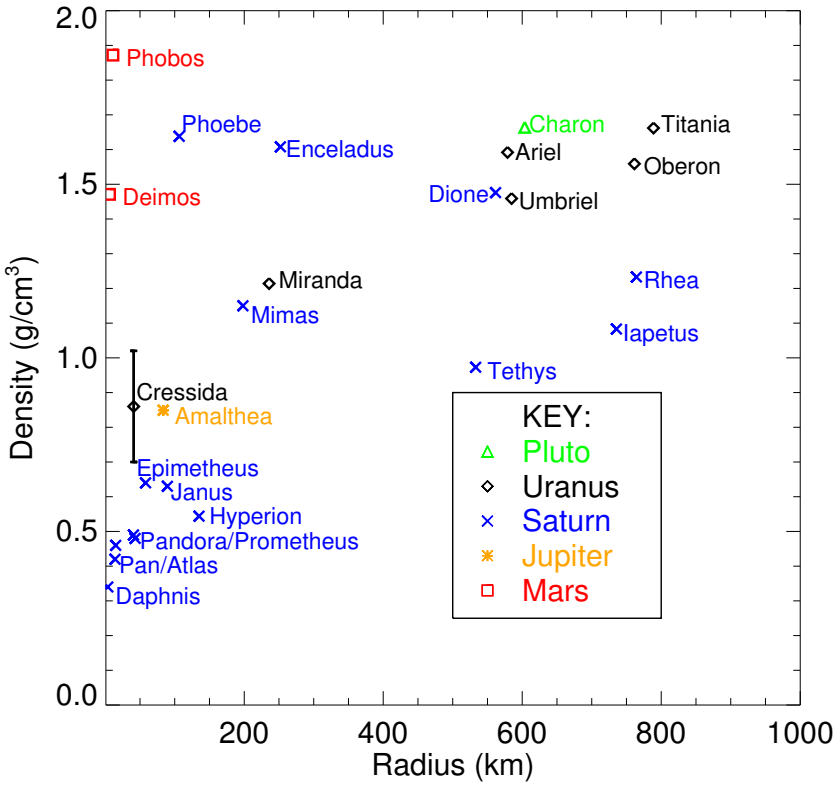

Figure 3.6: The known densities of selected satellites in the solar system are plotted versus their radii. We represent the individual moons associated with particular planets using the point styles and colors labeled in the lower right of the plot.

Chapter 4: Seasonal structures in Saturn's dusty Roche Division correspond to periodicities of the planet's magnetosphere

Chancia, R.O., Hedman, M.M., Cowley, S.W.H., Provan, G., Ye, S.-Y. "Seasonal structures in Saturn's dusty Roche Division correspond to periodicities of the planet's magnetosphere" *Icarus, vol. 330, 2019, pp. 230-255*

This work was motivated by the initial findings of Hedman et al. (2009a) in images of the dusty D ring and Roche Division from 2006 and 2007. They found that brightness variations in the D ring and Roche Division were located at a resonance with Saturn's kilometric radiation, which is rotationally modulated by Saturn's planetary period oscillations (PPO). When I began investigating these rings in 2016 there were nearly ten years of mostly unreduced images of both ring regions available to explore. My goal was to track the behavior of the brightness variations in the rings over the course of the mission. First, we realized that over time the appearance of both the D ring and the Roche Division changed significantly. In fact, the brightness variations in the Roche Division were absent in all observation after 2007. This made some sense, because Saturn's two hemispherical PPO were also found to be drifting in rotational frequency over the course of the mission. The southern hemisphere PPO rate actually increased so much that its resonance in the Roche Division drifted inwards into the dense A ring edge where ring particles are too massive to be significantly influenced by electromagnetic forces. It wasn't until the summer of 2016 that we again detected the brightness variations in the Roche Division, after the northern hemisphere PPO slowed and allowed for a resonance in the dusty Roche Division once again.

At this point, we knew that the connection between these dusty rings and Saturn's enigmatic magnetosphere was definitive. I then developed a model based on the theory of Lorentz resonances and of resonant perturbations in dusty rings to determine the forces necessary to cause the structures we observed. I found that with reasonable estimates of the ring particle charge to mass ratio, that an oscillating B_θ magnetic field component of a few nanotesla was needed to produce the ring structures, consistent with observations made by the magnetometer team of the magnetic field PPO. In fact, our observations of the Roche Division from several years apart show that the structures are in sync with the PPO phases measured by the magnetometer and radio and plasma waves teams.

This work shows the intimate connection between Saturn's rings and magnetosphere. It also helps to motivate further interdisciplinary studies of the giant planets and missions concepts, like a ring skimmer.

4.1 Abstract

We identify multiple periodic dusty structures in Saturn's Roche Division, a faint region spanning the $\sim$ 3000 km between the A and F rings. The locations and extent of these features vary over *Cassini's* tour of the Saturn system, being visible in 2006 and 2016-2017, but not in 2012-2014. These changes

can be correlated with variations in Saturn's magnetospheric periods. In 2006 and 2016-2017, one of the drifting magnetospheric periods would produce a 3:4 resonance within the Roche Division, but in 2012-2014 these resonances would move into the A ring as the magnetospheric periods converged. A simple model of magnetic perturbations indicates that the magnetic field oscillations responsible for these structures have amplitudes of a few nanotesla, comparable to the magnetic field oscillation amplitudes of planetary period oscillations measured by the magnetometer onboard *Cassini*. However, some previously unnoticed features at higher radii have expected pattern speeds that are much slower than the magnetospheric periodicities. These structures may reflect an unexpectedly long-range propagation of resonant perturbations within dusty rings.

4.2 Introduction

The Roche Division is a sparsely populated region of Saturn's rings located between the outer edge of the A ring and the F ring. Burns et al. (1983) first noted the presence of tenuous ring material between the A and F rings in a high phase angle *Voyager 2* image of the region. At the time, it was referred to as the Pioneer Division, following *Pioneer 11*'s discovery of the F ring (Gehrels et al., 1980). *Cassini* has since imaged the Roche Division many times, and Figure 4.1 provides an overview of this region. The image shows several diffuse bands of dust populating almost the entire Roche Division. The Roche Division is also home to two of Saturn's innermost moons, Atlas and Prometheus, which stir up and provide a source of dust in their vicinity. The outermost dust band, at approximately $139,400$ km from Saturn's center, is typically the brightest feature in the region. Hedman & Carter (2017) showed that this ringlet is in a co-orbital 1:1 resonance with Prometheus, but strangely precesses with the F ring. During *Cassini's* Saturn orbit insertion, the *Cassini* imaging team found two regions in the Roche Division with higher concentrations of dust than their surroundings (Porco et al., 2005). These apparent dusty ringlets were designated R/2004 S1 (Porco & Cassini Imaging Science Team, 2004) orbiting near Atlas at 137,630 km and R/2004 S2 (Porco, 2004) interior to Prometheus at 138,900 km. In Figure 4.1 we can see additional fainter dust bands between these two. Hedman et al. (2009a) used image sequences taken in 2006 to determine that R/2004 S1 does not form a true closed ringlet, but a periodic structure composed of alternating diagonal bright and dark streaks. The structure is consistent with a dusty-ring's response to a strong resonance with a pattern speed near Saturn's rotation rate. The Roche Division is largely made up of tiny micron-sized particles that are sensitive to perturbations from non-gravitational forces. This led Hedman et al. (2009a) to suspect that there is likely a connection with the magnetic field and/or radio emissions which were observed to be rotationally modulated at a rate commensurate with the Roche Division structure's pattern speed.

Despite the perfect axisymmetry of Saturn's internally-generated magnetic field to within measurement accuracy (Dougherty et al., 2018), modulations near the ~ 10.5 h planetary rotation period termed "planetary period oscillations" (PPOs) are ubiquitously observed throughout the magnetosphere. Such modulations are observed in the magnetic field (Espinosa & Dougherty, 2000; Andrews et al., 2010b; Hunt et al., 2014; Bradley et al., 2018), plasma properties and boundaries (Gurnett et al., 2007; Clarke et al., 2010; Arridge et al., 2011; Ramer et al., 2017; Thomsen et al., 2017), energetic particle and associated

energetic neutral atom fluxes (Carbary & Krimigis, 1982; Carbary et al., 2009, 2011; Carbary, 2017), plasma waves (Gurnett et al., 2009b; Ye et al., 2010), auroral ultraviolet and infrared emissions (Nichols et al., 2010; Badman et al., 2012; Bader et al., 2018), and auroral radio emissions (Desch & Kaiser, 1981; Gurnett et al., 2011b; Lamy et al., 2011, 2013). Analysis of the auroral radio emissions, specifically of Saturn kilometric radiation (SKR), provided the first evidence that two such modulation systems with slightly different periods are present (Kurth et al., 2008; Gurnett et al., 2009a), one associated with the northern polar ionosphere and the other with the southern, and that these periods vary slowly over Saturn's seasons by up to $\sim \pm 1\%$ about a period of ~ 10.7 h (Galopeau & Lecacheux, 2000; Gurnett et al., 2010). Subsequently, the remotely sensed SKR emissions were used to derive the varying northern and southern PPO periods over the whole interval of the *Cassini* science mission from January 2004 to end of mission in September 2017 (Lamy, 2011, 2017; Gurnett et al., 2011a; Ye et al., 2016, 2018). The periods and phases of the related magnetospheric magnetic perturbations have also been derived from *Cassini* magnetometer (MAG) data from shortly after orbit insertion in mid-2004 to the end of mission (Andrews et al., 2008, 2012; Provan et al., 2013, 2016, 2018), apart from a few intervals when the perturbations due to one or other of the two PPO systems became too weak to be discerned. Comparison of the results derived independently from these data sets generally shows very good agreement (Andrews et al., 2010a; Provan et al., 2014, 2016, 2018), as expected if both phenomena result from the same rotating magnetosphere-ionosphere current systems generated in the two polar ionospheres (Jia et al., 2012; Southwood & Cowley, 2014). Specifically both SKR and MAG results show that the southern PPO system was the stronger under Saturn southern summer conditions at the start of the *Cassini* mission, and had a longer period ~ 10.8 h ($800^\circ \mathrm{day}^{-1}$) than that of the northern system ~ 10.6 h ($815^\circ \mathrm{day}^{-1}$). The two periods then converged towards a common value ~ 10.7 h ($808^\circ \mathrm{day}^{-1}$) around Saturn equinox in mid-2009, and after an interval of complex variable behavior, finally enduringly reversed in mid-2014 prior to northern solstice in mid-2017, with the stronger northern PPO system moving to a period of ~ 10.8 h while the southern system period remained near ~ 10.7 h. The magnetic oscillations of few nano-Tesla amplitude associated with the PPOs form a likely source of perturbations in the Roche Division.

The inner Roche Division structures discovered by Hedman et al. (2009a) were associated with the stronger longer period southern system in 2006. The Roche Division's microscopic ring particles are very effective at scattering incident sunlight in the forward direction and so are more easily observable in high-phase-angle (low scattering-angle) images. In this work we perform a comprehensive investigation of the high-phase-angle image sequences of the Roche Division obtained by the *Cassini* Imaging Science Subsystem (ISS). Due to *Cassini's* orbit geometry, the observations useful to this study are clumped into 3 distinct periods: 2006, 2012-2014, and 2016-2017. We find that the presence of periodic structures in the Roche Division is time variable. The structures are present in all 2006 observations as reported by Hedman et al. (2009a), but are not detected during any of the observation sequences from 2012-2014. The structures reappeared at some time before July of 2016, and are present in all later observations. This provides further evidence that the structures are somehow tied to Saturn's PPOs.

We present the theoretical background of Lindblad resonances in planetary rings in Section 2, with particular emphasis on their framework in dusty rings, and our model of electromagnetic perturbations. We then report the observational data and data reduction procedures used in this analysis in Section 3. In

Section 4, we detail the relevant pattern speeds and amplitudes from each epoch and make comparisons to the results of the magnetometer and radio and plasma wave science instruments. We discuss the significance of our detected pattern speeds and strengths in Section 5. Finally, in Section 6 we summarize our findings.

4.3 Theoretical background

In this work we use the model of Lindblad resonances in faint rings developed by Hedman et al. (2009a), to quantify the periodic structures in the Roche Division over the course of the *Cassini* mission. This theory can account for ring structures produced by any periodic forcing that is commensurate with the ring particles' eccentric epicyclic motion and is not limited to classical Lindblad resonances associated with satellites. In dense rings, having sufficient mass and optical depth, Lindblad resonances produce density waves. Density waves have been studied extensively in Saturn's rings, particularly the A ring where many strong satellite resonances fall (Tiscareno et al., 2007). Strong Lindblad resonances in faint rings produce structures with a different appearance than those in dense rings. The sheets of dust in the Roche Division, with normal optical depth $\tau_n = (1-2) \times 10^{-4}$ (Showalter et al., 1998), lack the particle collision frequency and self-gravity necessary to sustain a normal spiral density wave.

However, Hedman et al. (2009a) found periodic azimuthal brightness variations in dusty rings at Lindblad resonances with Saturn's moon Mimas and with the rotation of Saturn's magnetic field.

In Section 4.3.1 we discuss the general theory of Lindblad resonances. In Section 4.3.2 we discuss the specific case of the dusty Roche Division particles responding to a Lindblad resonance. Finally in Section 4.3.3 we derive a simple model of an oscillating magnetic field component and determine the perturbed radial amplitude of the rings under particular conditions.

4.3.1 Lindblad resonances

For a ring particle in orbit around a central planet with a single satellite, the condition for a first-order Lindblad resonance is that the resonant argument:

$$\varphi = m(\lambda - \lambda_s) - (\lambda - \varpi) \tag{4.1}$$

is constant in time, $\frac{d\varphi}{dt} = 0$. The inertial longitudes of the ring particle and satellite are λ and λ_s respectively and the ring particle's longitude of pericenter is ϖ. The integer m is the azimuthal wavenumber of the resonance, and is positive (negative) for an inner (outer) Lindblad resonance, or ILR (OLR), where the ring particle is interior (exterior) to the satellite's orbit. This condition means that whenever the ring particle is in conjunction with the satellite, it will always be in the same phase of its eccentric orbit. For example, if $\lambda - \lambda_s = 0$ (conjunction) occurs at the same time as $\lambda - \varpi = 0$ (the ring particle is at periapse) then every time the ring particle approaches the satellite's longitude it will be back at its periapse. This allows the satellite's perturbations on the ring particle to build up and enhance the eccentricity of particles orbiting close to the resonance, as they always have close encounters with the perturbing moon in the same phase of their orbits.

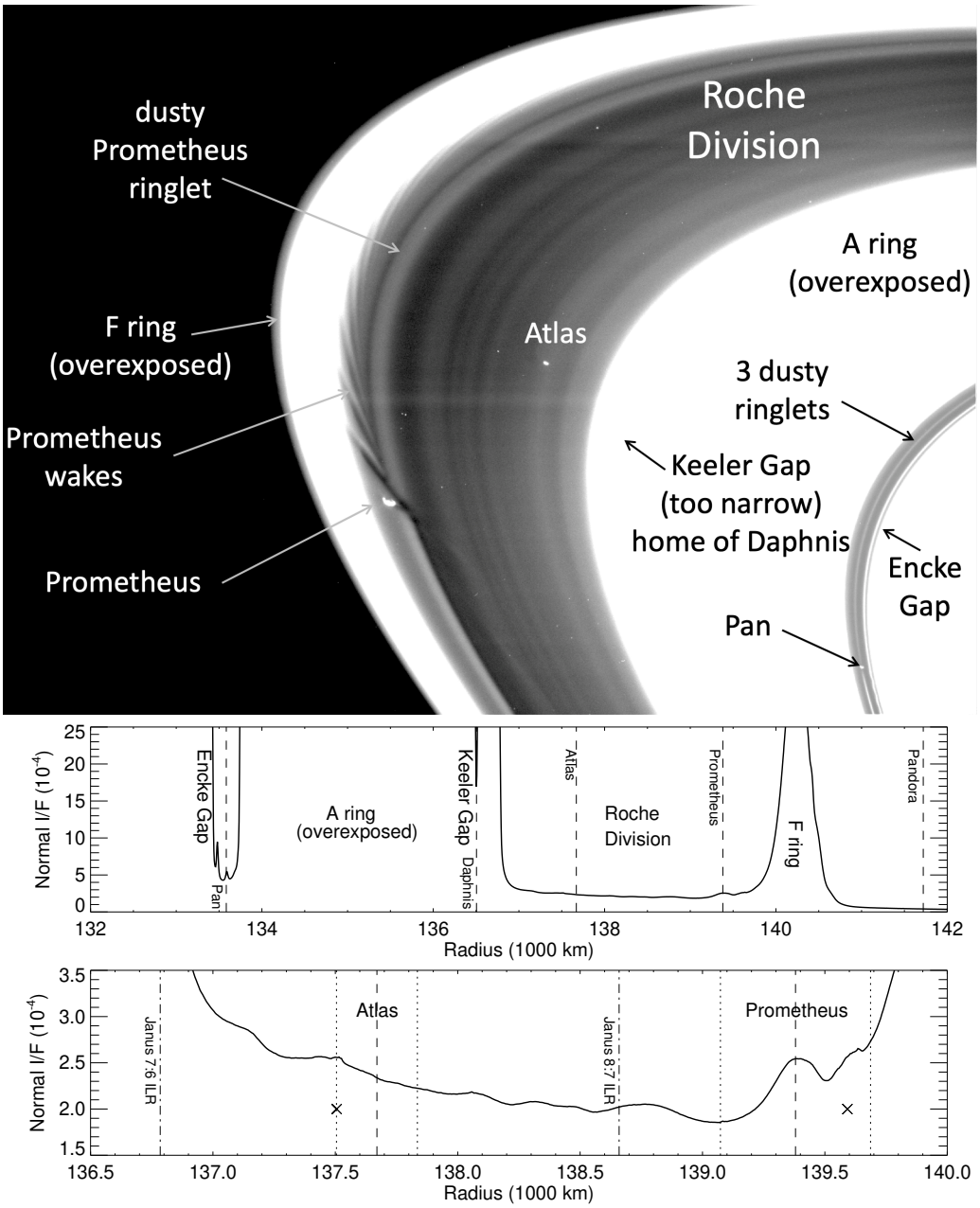

Figure 4.1: On top is a labeled image (N1870374754 from Rev 268a), with arrows noting ring features and moons. The image has been stretched to highlight faint dusty structures. Note that the narrow Keeler Gap is not visible in this image because the stray light from the A ring causes it to appear artificially bright. Below are two radial scans of the image, showing the azimuthally averaged reflectance of the rings in Normal I/F (see Section 4.4.2) vs. radial distance from Saturn's center. The lower plot is zoomed in on the Roche Division. Dashed lines mark the semi-major axes of each moon, while the dotted lines mark their pericenter and apocenter in the lower plot. Dot-dashed lines mark the locations of Janus/Epimetheus 1st order Lindblad resonances. The actual radial locations of Atlas and Prometheus at the time the image was taken are marked with X symbols.

The expected forced radial amplitude, ae_F, on ring particles with semi-major axis, a, near a 1st order Lindblad resonance at a_r is given by (Murray & Dermott (1999) Equation 10.22)

$$ae_F \approx \frac{1.6a^2(M_s/M_p)}{3|a-a_r|}, \tag{4.2}$$

where M_s and M_p are the masses of the perturbing satellite and central planet respectively. In the absence of mutual interactions among ring particles the orbits of particles near a Lindblad resonance will follow a streamline path defined by their radius as a function of inertial longitude λ and time t:

$$r(\lambda, t) = a + ae_F \cos\phi, \tag{4.3}$$

where $\phi = m(\lambda - \Omega_p(t-t_0) - \delta_m)$ is the phase of the periodic structure. In a rotating frame the streamlines form m-lobed shapes with a specific orientation relative to the perturbing satellite, where δ_m is the inertial longitude of one of the structure's m-periapses ($a < a_r$) or m-apoapses ($a > a_r$) at epoch time t_0 and is roughly aligned with the longitude of the perturber. The structure rotates with a pattern speed Ω_p equivalent to the mean motion of the perturbing satellite. In dense rings, gravitational interactions among the ring particles cause neighboring streamlines located further and further from the resonance to shift in phase relative to the satellite, creating the appearance of an m-armed spiral density wave. Alternatively, a strong resonance near a ring's edge can form an m-lobed sinusoidal pattern as is the case for the outer edges of Saturn's B ring (Mimas 2:1 ILR) and A ring (Janus/Epimetheus 7:6 ILR) (Porco et al., 1984; Spitale & Porco, 2009; Nicholson et al., 2014a). Satellite resonances can also influence the entirety of narrow dense rings. This is the case for Uranus' 2 km wide η ring which has a 3-lobed oscillation in its radius produced by the ring's proximity to Cressida's 3:2 ILR (Chancia et al., 2017).

4.3.2 3:4 Outer Lindblad Resonances in the Roche Division

The structures in the Roche Division have pattern speeds and symmetries consistent with $m = -3$ Outer Lindblad Resonances (OLR). No appropriate 1st-order Lindblad resonance with a Saturnian satellite falls within this region (for the Janus/Epimetheus 8:7 ILR see Section 4.6.2), but Hedman et al. (2009a) found that these structures were located coincident with the 3:4 resonance of the southern PPO system in 2006. By taking the time-derivative of Equation 4.1 we obtain another expression that governs Lindblad resonances and normal modes:

$$m\Omega_p = (m-1)n + \dot{\varpi} = mn - \kappa \tag{4.4}$$

where $\frac{d\lambda_s}{dt} = \Omega_p$ is the pattern speed and mean motion of the perturber, $\frac{d\lambda}{dt} = n$ is the local mean motion, κ is the local epicyclic frequency, and $\dot{\varpi} = n - \kappa$ is the local apsidal precession rate. Note that n and κ are the angular and epicyclic frequencies, corrected for the effects of an oblate central planet (Lissauer & Cuzzi, 1982). The 3-lobed structures generated by such a resonance that could occur between the outer edge of the A ring (mean radius of 136,770 km) and the orbit of Prometheus ($a = 139,380$ km) are expected to have pattern speeds of 804.64°day^{-1} to 782.11°day^{-1} respectively, or roughly 4/3 the

mean motion of ring particles orbiting in the Roche Division ($n = 604.22°\text{day}^{-1}$ to $587.27°\text{day}^{-1}$). Thus, in image-movies that span about one local orbital period we see 4/3 of the structure pass through the imaged longitudinal region. Note that if we construct mosaics in a co-rotating longitude system using the expected pattern speed of $\sim 800°\text{day}^{-1}$ we see the full 3-fold symmetric pattern.

Individual dusty ring particles will also respond to gravitational perturbations near a strong Lindblad resonance. However, in the case of dusty rings the particle streamlines appear to be "damped" to form a region of canted brightness variations straddling the resonance. Hedman et al. (2009a) created a model to explain the observed behavior of dusty ring structures in Saturn's Roche Division, D ring, and G ring by introducing a dissipative term to the equations of motion. This presumed dissipation causes a phase shift of ring particle streamlines that depends on their radial distance from the resonance and results in the observed canted brightness variations (see Figure 4.2 below).

For a low optical depth region, like the Roche Division, the fractional brightness variations are a small percentage of the overall brightness and are effectively equivalent to the local fractional surface density variations. In their model of Lindblad resonances in faint rings, Hedman et al. (2009a) found that the fractional surface density variations $\frac{\delta\rho}{\rho}$ near a resonance in a dusty ring are given by:

$$\frac{\delta\rho}{\rho}(r,\phi) = \frac{\beta}{[(\delta r)^2 + L^2]^2}[((\delta r)^2 - L^2)\cos\phi + 2\delta r L \sin\phi], \tag{4.5}$$

where δr is the radial distance from the exact resonance, β is a measure of the resonance strength, and L is a damping length. The amplitude of the brightness variations

$$A(r) = \frac{\beta}{(\delta r)^2 + L^2} \tag{4.6}$$

due to the density variations reaches a peak at the exact resonance. Additionally, this amplitude of the brightness variations is proportional to the strength of the resonance. A full derivation of the relevant equations from Hedman et al. (2009a) is reiterated in Appendix D with some corrections.

Hedman et al. (2009a) found that the G ring resonant structure straddles the Mimas 8:7 ILR, such that its maximum brightness variations do in fact peak at the exact resonance[1]. Thus, we can determine the exact resonance locations even when we do not know the exact angular frequency of the perturber and also approximate the strength of the resonance in terms of a satellite mass when we do not know the mass of the perturber. Alternatively, if these structures are generated by Saturn's magnetic field, the perturbing force is more likely the Lorentz force, and so we can estimate the amplitude of the magnetic-field variations.

4.3.3 Simple magnetic field perturbation model

As we have explained above, it is most likely that the dust in the Roche Division is perturbed at the 3:4 OLR with the rotational modulation of Saturn's magnetosphere. The case for resonances with the rotation of planetary magnetic fields, or Lorentz resonances, has been explored to explain the structure

[1]However, the reported amplitude of the variations is actually 2.5 times larger than one would expect, so the estimated value of $\beta = \frac{1.6a^2}{3}\frac{M_s}{M_p}$ overestimates the mass of Mimas by a factor of 2.5, see Section 4.6.2 below.

of Jupiter's faint rings (Burns et al., 1985). In fact, the theory has been derived extensively in the works of Schaffer & Burns (1992) and Hamilton (1994). We summarize those derivations in Appendix E, but note that in order to approximate the strength of the 3:4 Lorentz resonance in question, one needs to know the planet's non-axisymmetric magnetic field coefficients. However, current models of Saturn's magnetic field (Dougherty et al., 2018) show that the planet has negligible non-axisymmetric components, so the relevant magnetic field perturbations are probably external to the planet. Thus, we improvise by instituting a simple sinusoidal perturbation in the magnetic field that resembles the observed planetary period oscillations measured by *Cassini's* magnetometer.

We begin with the Lorentz Force $\mathbf{F_L} = q_g \mathbf{v_{rel}} \times \mathbf{B}$ on a charged dust grain q_g, which arises from the rotation of Saturn's magnetic field $\mathbf{B}$. Here $\mathbf{v_{rel}}$ is a ring particle's orbital velocity relative to the angular frequency of Saturn's PPO rotation Ω_S given by

$$\mathbf{v_{rel}} = \mathbf{v} - (\boldsymbol{\Omega_s} \times \mathbf{r}) \tag{4.7}$$

where $\mathbf{r}$ and $\mathbf{v}$ are a ring particle's radial position and Keplerian orbital velocity in the ring plane. We are considering low eccentricity rings around Saturn, whose magnetic pole is effectively aligned with its rotation axis (Dougherty et al., 2018), so we can simplify this expression to

$$\mathbf{v_{rel}} = a(n - \Omega_S)\hat{\boldsymbol{\phi}}. \tag{4.8}$$

Our Lorentz force is then given by

$$\mathbf{F_L} = -q_g a(n - \Omega_S)\left[B_\theta \hat{\mathbf{r}} - B_r \hat{\boldsymbol{\theta}}\right] \tag{4.9}$$

where the radius r, polar angle θ, and azimuthal angle ϕ define the usual spherical coordinates relative to the rotating planet. We mainly care about the small PPO magnetic perturbation on top of the static B_θ component of the magnetic field because it will produce an oscillating force in the radial direction, as needed to create a Lindblad resonance. While the fundamental PPO magnetospheric signal will go like $\cos(\lambda - \Omega_S t)$, deviations in the shape of the magnetic field perturbation from a pure sinusoid and nonlinearities in the expression for the perturbing force will give rise to harmonics of the form $\cos[j(\lambda - \Omega_S t)]$ for various integer values of j. We consider a simple perturbation $B_{\theta 0}\cos[j(\lambda - \Omega_S t)]$ where $B_{\theta 0}$ can be compared to measured MAG oscillations modulated by the rotation periods associated with the northern and southern PPO systems (Provan et al., 2018).

The perturbation produces a radial force given by

$$F_r = -q_g a(n - \Omega_S) B_{\theta 0}\cos[j(\lambda - \Omega_S t)]. \tag{4.10}$$

This perturbing force can now be inserted into the perturbation equations of a ring particle's eccentricity and longitude of pericenter, which for objects on nearly circular orbits are (Burns, 1976, 1977)

$$\frac{de}{dt} = n\left[\frac{F_r}{F_G}\sin f + 2\frac{F_\lambda}{F_G}\cos f\right] \tag{4.11}$$

and

$$\frac{d\varpi}{dt} = \frac{n}{e}\left[-\frac{F_r}{F_G}\cos f + 2\frac{F_\lambda}{F_G}\sin f\right] \tag{4.12}$$

where the ring particle's true anomaly $f = \lambda - \varpi$ and the central gravitational force on a dust grain of mass m_g due to Saturn is $F_G = \frac{GM_S m_g}{a^2}$. After plugging in our F_r (assuming the longitudinal force $F_\lambda = 0$) and applying the appropriate trigonometric product and sum identities these become:

$$\frac{de}{dt} = \frac{-nq_g a^3(n-\Omega_S)B_{\theta 0}}{GM_S m_g}\frac{1}{2}\{\sin\left[j(\lambda-\Omega_S t)+(\lambda-\varpi)\right] - \sin\left[j(\lambda-\Omega_S t)-(\lambda-\varpi)\right]\} \tag{4.13}$$

and

$$\frac{d\varpi}{dt} = \frac{nq_g a^3(n-\Omega_S)B_{\theta 0}}{eGM_S m_g}\frac{1}{2}\{\cos\left[j(\lambda-\Omega_S t)+(\lambda-\varpi)\right] + \cos\left[j(\lambda-\Omega_S t)-(\lambda-\varpi)\right]\}. \tag{4.14}$$

The perturbations on the ring particles are small, so we can assume that $\lambda \approx nt$ and $\varpi \approx \dot{\varpi_0}t$. Hence, for particles near a particular resonance with a specified value of m, these expressions will nearly all average to zero. The only case where this does not happen is when $j = m$, in which case the first term will average to zero and the second can be written with $\varphi = m(\lambda - \Omega_S t) - (\lambda - \varpi)$. Hence the time-average perturbation questions become:

$$\left\langle \frac{de}{dt} \right\rangle = \frac{nq_g a^3(n-\Omega_S)B_{\theta 0}}{2GM_S m_g}\sin\varphi \tag{4.15}$$

and

$$\left\langle \frac{d\varpi}{dt} \right\rangle = \frac{nq_g a^3(n-\Omega_S)B_{\theta 0}}{2eGM_S m_g}\cos\varphi + \dot{\varpi_0}. \tag{4.16}$$

Following the logic used to derive Equation E.9 we find the forced eccentricity is

$$a_r e_f = \frac{1}{3}\frac{q_g}{m_g}\frac{a_r^5}{\delta a}\frac{n/\Omega_S - 1}{m-1}\frac{\Omega_S}{GM_S}B_{\theta 0} \tag{4.17}$$

where our resonance strength is given by

$$\beta = \frac{1}{3}\frac{q_g}{m_g}a_r^5\frac{n/\Omega_S - 1}{m-1}\frac{\Omega_S}{GM_S}B_{\theta 0}. \tag{4.18}$$

Finally for the case of the Roche Division, where $m = -3$ and $\frac{n}{\Omega_S} \approx \frac{3}{4}$ we find:

$$\beta = \frac{1}{48}\frac{q_g}{m_g}a_r^5\frac{\Omega_S}{GM_S}B_{\theta 0} \tag{4.19}$$

which can be used to estimate the amplitude of magnetic field oscillations needed to produce the observed structures in the rings.

Table 4.1: Imaging sequences used in this study

Mov ID	Obs ID	Files	#	Date	Dur	Exp	Phase	Emiss	Long
029ax	ISS_029RF_FMOVIE001_VIMS	N1538168640-N1538193384	24	2006 SEP 28	6.9	0.18	158.4-160.2	57.5- 58.3	265.6-267.7
029ay	ISS_029RF_FMOVIE001_VIMS	N1538269441-N1538275217	6	2006 SEP 30	1.6	0.18	158.9-159.3	60.6- 60.8	83.4- 83.9
029bx	ISS_029RF_FMOVIE001_VIMS	N1538169174-N1538217594	46	2006 SEP 28	13.4	0.68	158.5-161.7	57.5- 59.1	265.7-269.5
029by	ISS_029RF_FMOVIE001_VIMS	N1538270015-N1538300071	27	2006 SEP 30	8.3	0.68	158.9-161.0	60.6- 61.5	83.5- 85.7
029cx	ISS_029RF_FMOVIE001_VIMS	N1538194460-N1538218132	23	2006 SEP 29	6.6	0.15	160.3-161.8	58.3- 59.1	267.8-269.6
029cy	ISS_029RF_FMOVIE001_VIMS	N1538276373-N1538299493	21	2006 SEP 30	6.4	0.15	159.4-160.9	60.8- 61.5	84.0- 85.7
030a	ISS_030RF_FMOVIE001_VIMS	N1539655570-N1539660972	4	2006 OCT 16	1.5	0.46	150.6-151.0	48.7- 48.9	265.0-265.5
030b	ISS_030RF_FMOVIE001_VIMS	N1539656467-N1539683497	16	2006 OCT 16	7.5	1.00	150.6-152.4	48.7- 49.7	265.1-267.5
030c	ISS_030RF_FMOVIE001_VIMS	N1539662774-N1539682596	12	2006 OCT 16	5.5	0.38	151.1-152.4	48.9- 49.6	265.7-267.4
031a	ISS_031RF_FMOVIE001_VIMS	N1541012989-N1541025000	28	2006 OCT 31	3.3	0.26	156.3-157.4	51.9- 52.7	95.0- 96.2
031b	ISS_031RF_FMOVIE001_VIMS	N1541025445-N1541045470	46	2006 OCT 31	5.6	0.22	157.4-159.0	52.7- 54.1	96.2- 98.2
031cx	ISS_031RF_FMOVIE001_VIMS	N1541045915-N1541062380	38	2006 NOV 01	4.6	0.18	159.1-160.3	54.1- 55.2	98.2- 99.7
031cy	ISS_031RF_FMOVIE001_VIMS	N1541110189-N1541119755	12	2006 NOV 01	2.7	0.18	159.9-160.0	58.3- 58.9	294.3-294.9
032a	ISS_032RF_FMOVIE001_VIMS	N1542047155-N1542063616	38	2006 NOV 12	4.6	0.26	155.9-157.3	51.8- 52.9	94.7- 96.4
032b	ISS_032RF_FMOVIE001_VIMS	N1542064061-N1542084086	46	2006 NOV 12	5.6	0.22	157.4-159.0	52.9- 54.3	96.4- 98.3
032c	ISS_032RF_FMOVIE001_VIMS	N1542084531-N1542096546	28	2006 NOV 13	3.3	0.18	159.1-160.0	54.3- 55.1	98.4- 99.4
032d	ISS_032RF_FMOVIE001_VIMS	N1542149816-N1542156952	18	2006 NOV 13	2.0	0.12	163.5-163.9	58.5- 59.0	103.7-104.2
033	ISS_033RF_FMOVIE001_VIMS	N1543166702-N1543216891	99	2006 NOV 25	13.9	0.56	159.8-160.7	57.6- 60.7	293.5-296.5
036	ISS_036RF_FMOVIE001_VIMS	N1545557060-N1545613256	127	2006 DEC 23	15.6	0.56	158.6-160.8	54.2- 57.2	285.9-289.7
039a	ISS_039RF_FMOVIE002_VIMS	N1549801218-N1549851279	123	2007 FEB 10	13.9	2.60	125.5-131.1	31.4- 33.1	243.2-254.8
039b	ISS_039RF_FMOVIE002_VIMS	N1549901779-N1549911779	26	2007 FEB 11	2.8	3.20	136.6-137.7	35.8- 36.5	265.1-267.0
173ax	ISS_173RF_FMOVIE001_PRIME	N1729024626-N1729053296	55	2012 OCT 15	8.0	1.80	137.5-142.1	123.9-124.2	138.4-112.4
173by	ISS_173RF_FMOVIE001_PRIME	N1729053606-N1729082276	55	2012 OCT 16	8.0	1.20	153.4-160.8	123.3-118.4	334.3-308.4
174x	ISS_174RF_FRSTRCHAN001_PRIME	N1731106419-N1731132308	63	2012 NOV 08	7.2	1.20	150.4-156.0	123.6-121.2	318.5-318.5
174y	ISS_174RF_FRSTRCHAN001_PRIME	N1731132699-N1731158588	64	2012 NOV 09	7.2	1.20	143.9-149.5	121.6-119.3	135.0-135.1
185a	ISS_185RI_ROCHEMOV001_PRIME	N1743541318-N1743581038	31	2013 APR 01	11.0	2.00	139.4-162.7	134.5-116.1	138.9-159.4
196	ISS_196RF_FMOVIE006_PRIME	N1756377239-N1756428571	125	2013 AUG 28	14.3	1.20	145.3-150.1	132.7-129.5	301.1-304.6
201	ISS_201RF_FMOVIE001_VIMS	N1770315948-N1770367142	160	2014 FEB 05	14.2	1.20	125.8-142.8	137.6-131.0	305.0-327.3
203x	ISS_203RF_FMOVIE001_PRIME	N1776077815-N1776106170	70	2014 APR 13	7.9	1.20	139.8-136.5	74.5- 72.1	203.1-202.8
203y	ISS_203RF_FMOVIE001_PRIME	N1776106495-N1776134850	70	2014 APR 13	7.9	1.20	132.0-129.0	72.2- 70.3	37.2- 37.2
208x	ISS_208RF_FMOVIE001_PRIME	N1789913768-N1789932276	90	2014 SEP 20	5.1	1.20	131.9-142.4	132.6-126.5	51.6- 51.2
209x	ISS_209RF_FMOVIE001_PRIME	N1793068408-N1793089959	46	2014 OCT 27	6.0	1.20	134.2-132.8	72.0- 71.2	218.6-218.6
209y	ISS_209RF_FMOVIE001_PRIME	N1793090708-N1793110822	43	2014 OCT 27	5.6	1.20	129.1-127.9	71.2- 70.5	44.1- 44.2

Mov ID	Obs ID	Files	#	Date	Dur	Exp	Phase	Emiss	Long
237	ISS_237RI_EGAPMOVMP001_PRIME	N1846112392-N1846137205	28	2016 JUL 01	6.9	0.32	135.3-130.5	83.8- 80.7	243.8-247.7
240	ISS_240RF_FMOVIE002_PRIME	N1850609421-N1850636617	50	2016 AUG 23	7.6	1.50	134.6-130.2	81.0- 77.5	245.4-246.1
241	ISS_241RI_FNTHPMOV001_PRIME	N1851525687-N1851564003	32	2016 SEP 02	10.6	2.00	159.7-149.9	100.2- 92.7	228.8-235.1
265	ISS_265RF_FMOVIE001_PRIME	N1867972213-N1867991971	30	2017 MAR 12	5.5	1.20	134.3-132.0	74.8- 72.6	233.6-233.6
268a	ISS_268RI_HPMONITOR002_PRIME	N1870352908-N1870396600	23	2017 APR 08	12.1	2.00	145.6-140.7	84.5- 80.1	238.3-241.6
272	ISS_272RF_FMOVIE001_PRIME	N1872298730-N1872325959	74	2017 MAY 01	7.6	1.00	136.5-133.7	75.3- 72.6	237.6-238.2
274x	ISS_274RF_FMOVIE001_PRIME	N1873378488-N1873395652	75	2017 MAY 13	4.8	1.00	139.9-138.5	78.0- 76.6	233.8-234.3
274y	ISS_274RF_FMOVIE001_PRIME	N1873415748-N1873456613	172	2017 MAY 14	11.4	1.00	130.3-124.4	74.3- 69.8	83.8- 84.2
281	ISS_281RI_HPMONITOR001_PRIME	N1877745556-N1877791066	38	2017 JUL 03	12.6	2.00	147.3-144.3	84.1- 81.0	221.2-221.1
287	ISS_287RI_HPMONITOR001_PRIME	N1880562754-N1880589544	31	2017 AUG 04	7.4	2.00	145.0-143.0	82.1- 80.3	54.7- 56.3
289	ISS_289RF_FMOVIE001_PRIME	N1881776562-N1881839798	156	2017 AUG 18	17.6	1.00	137.8-131.5	75.0- 68.4	226.4-228.1
292	ISS_292RF_FMOVIE001_PRIME	N1883393812-N1883445888	63	2017 SEP 06	14.5	0.68	142.2-138.2	78.9- 75.1	42.5- 42.8

Inertial longitudes are measured relative to the ascending node of the rings on J2000. Image movie IDs are a combination of Rev number, exposure duration (a, b, or c), and ring ansa (x or y). Observations such as 029ay and 029cy are too short to be useful on their own, but can be combined with each other and 029by (see Figure G.2).

4.4 Observational data

We conducted a comprehensive survey of the available Roche Division images from the *Cassini* cameras. Section 4.4.1 summarizes the observations used in this study, while Section 4.4.2 describes how these data were processed to obtain maps of the fractional brightness variations that can be compared with the above model predictions.

4.4.1 Imaging data

This study examines high-phase-angle image sequences of the Roche Division obtained over the course of the entire *Cassini* mission by the Imaging Science Subsystem (ISS). For consistency, we only consider images obtained by the Narrow Angle Camera (NAC) using the clear filters, because they are the most common and have the highest signal-to-noise. Every image is calibrated using the standard CISSCAL calibration routines (Porco et al., 2004; West et al., 2010) to remove backgrounds, flatfield, and convert the raw data numbers into I/F, a standard measure of reflectance. I is the intensity of radiation scattered by the ring particles and πF is the solar flux at Saturn, so I/F is a unitless quantity that equals unity for a perfect Lambert surface viewed at normal incidence. We geometrically navigate the images using appropriate SPICE kernels (Acton, 1996) and by matching background point sources or streaks to stars in the Tycho and UCAC catalogs.

The images chosen for this analysis belong to movie sequences. These are image sequences taken of a common longitudinal region of the rings over the course of a large fraction of the local ring region's orbital period. This enables us to watch ring material move through the region over time, so we can detect radial and azimuthal brightness variations in the rings. We've found that the structures we are interested in are only detectable in images taken at phase angles α above around 130°.

Table 4.1 shows a breakdown of the complete dataset used in this study. *Cassini's* observations of the Roche Division were conducted during three distinct epochs, separated by the horizontal lines in the table. Throughout this work we identify the individual image sequences by their Saturn orbit numbers (or Rev number), exposure durations (a,b,c), and ring ansa (x or y) when necessary. This is not to be confused with the mission assigned Observation ID used to identify the images within archives, such as the PDS rings node. Table 4.1 also contains the ring ansa longitudes and lighting geometries spanned by the image sequences. Any individual images containing substantial defects or insufficient background stars for proper pointing have been removed from our in-depth analysis, but in some cases are useful merely for identifying the presence of structures (for instance Rev 289 has defects preventing proper analysis, but the presence of structures is clear). We also leave out observations that are less than 3.6 hours long, which are too short to reliably identify the resonant structures.

4.4.2 Data reduction

Each image of the Roche Division covers a relatively small range of longitude compared to the scale of the azimuthal brightness variations. Thus, we reduce each image into a high signal-to-noise profile of ring brightness as a function of radius by averaging the image's brightness data over all longitudes spanned

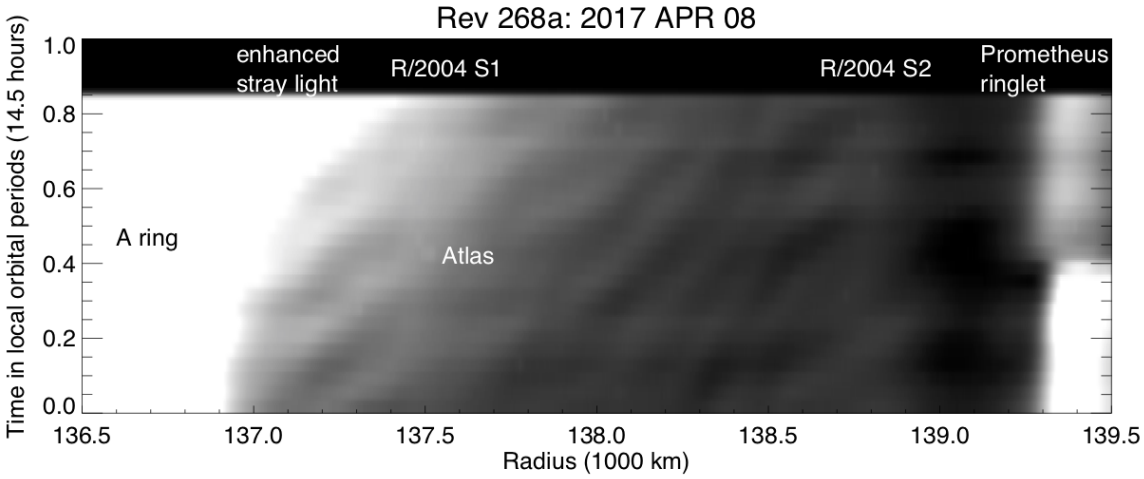

Figure 4.2: This map of the Roche Division is made up of average brightness radial profiles of individual images, at an inertial longitude of $\sim 240°$, stacked from bottom to top sequentially in time and shown in local orbital periods. The bright A ring edge is at the left of the map and the Prometheus ringlet is at the right, with a radial and brightness asymmetry clearly displayed on either side of Prometheus which passed by this longitude about halfway through the sequence (Atlas passed by at the same time and its faint brightness signature is labeled). The Roche Division is brighter in the upper left corner of the map because the ring opening angle is slowly increasing, resulting in a brighter A ring edge. There are multiple regions of diagonal brightness variations between $137,000$ and $139,000$ km.

by the image.

The lighting geometry in each image can vary significantly both within an individual sequence and between observations taken at different epochs. We can compare the radial profiles of images with different emission angles e or ring opening angles $B = 90° - e$ (not to be confused with the magnetic field) by converting the observed I/F reflectance into "normal I/F" or $\mu I/F$, where $\mu = |\sin B|$. Ideally, for a low optical depth region like the Roche Division, the normal I/F should be independent of incidence and emission angle. However, even after this correction several obstacles remain when trying to compare images from multiple sequences or even within individual sequences.

While several observations contain images with nearly identical phase angles, others have a gradual change in phase angle, sometimes by more than 10° over the course of the observation. The range of phase angles from all images included in the study is $125° - 163°$, making direct comparison of the normal I/F profiles problematic. The general trend for dusty rings is that they appear brighter at higher phase angles, which can be described in terms of a phase function. However, in this case further difficulties arise because of the background signals from the A and F rings.

There are drastic variations in stray light from the A ring among the different data sets because they include observations of both the lit and unlit side of the rings. Images of the lit side of Saturn's rings capture a bright A ring whose brightness can leak into the Roche Division due to the stray light and extended PSF of the camera (West et al., 2010). Raw radial scans of these images exhibit a bright inner Roche Division that generally decreases in brightness with increasing radii until approaching the inner

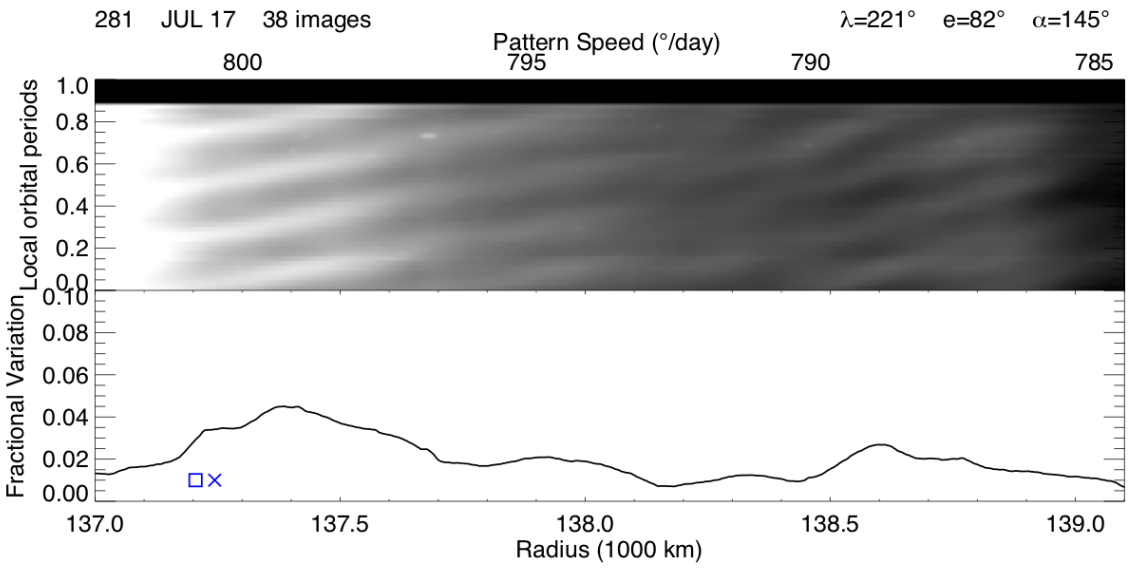

Figure 4.3: Above is a corrected brightness map of the Roche Division from Rev 281 similar to Figure 4.2, atop the fractional variation in the rings brightness at each radius and pattern speed. The SKR (X) and MAG (square) rate/radius are marked in blue for the northern hemisphere (red for the southern hemisphere at early times). The peak of 4.5% occurs at 799.2 $^\circ$day^{-1} or 137, 385 km. When the resonant structures are detected, those with the largest fractional brightness variations consistently occur in this inner region of the Roche Division near the magnetospheric periodicities.

edge of the Prometheus ringlet and the F ring (see Figures 4.1 and 4.2). Conversely, radial scans of the unlit side of the rings, which include a darker A ring, often reveal a much darker inner Roche Division with a general brightness enhancement contaminating the outer Roche Division as one approaches the F ring. Additionally, calibrated images with different exposure durations with otherwise nearly identical observation geometries can have constant instrumental offsets that produce slightly different reflectance levels in images of the Roche Division that are relevant here because the rings themselves are so faint.

These issues are best illustrated by considering a single data set. Figure 4.2 is an example map of the Roche Division, created using the radial scans from Rev 268a images. The Rev 268a image-movie monitored the Roche Division for 12.1 hours (about 0.86 local orbital periods). The radial profile of the first image is on the bottom, with the following images' radial scans shown in the map sequentially to the top. In this particular movie, the phase angle of each image decreases over the course of the observation from bottom ($\alpha = 145^\circ$) to top ($\alpha = 140^\circ$), which should normally cause a decrease in the observed reflectance due to less optimal forward scattering. In reality, brightness increases from bottom to top in the left side of the image because of increasing amounts of stray light from the A ring. The ring plane opening angles in this observation are all $< 10^\circ$ and vary by 4° over the course of the observation. At these small opening angles the A-ring's brightness depends strongly on the viewing geometry. In general, images with larger opening angles suffer from increased contamination of the bright A ring on the lit side of the rings after converting the profiles to Normal I/F. This means that as the ring opens up (smaller e, larger B) the Roche Division reflectance is artificially enhanced. This increase is especially apparent near

the A ring in the upper left corner of the mosaic. Whenever the ring opening angle and emission angle vary significantly, there is a similar alteration in ring brightness near the F ring in observations of the unlit side of the rings. We should also note that the Prometheus ringlet, located in the far right of this figure, has its own individual asymmetry in reflectance and radius on either side of Prometheus. This region is far enough from the A ring to be largely unaffected by the changing ring opening angle. However, the decrease in phase angle over the course of the observation serves to enhance this characteristic asymmetry observed in the Prometheus ringlet reflectance.

Despite these distracting trends in reflectance due to the lighting geometry, in Figure 4.2 we see that the bands of dust in individual images (e.g. Figure 4.1) change in radius over time (we recommend viewing the mosaic figures in the electronic copy). In fact, the ring brightness in each radial region is clearly periodic, appearing to increase and decrease four times over the course of an orbital period. In this observation there appear to be at least three distinct canted azimuthal brightness variations centered at approximately 137,300 km, 138,200 km, and 138,600 km. Each of these azimuthal brightness variations look like the characteristic response of dusty rings to a strong resonance described in Section 4.3.2 above.

Besides these patterns of canted bands, there are also structures in this region that might be tied to various moons. More continuous dust bands may occupy the narrow regions around 137,500 and 138,800 km, possibly corresponding to R/2004 S1&2 and having some relation to the orbit of Atlas and the position of the Janus/Epimetheus 8:7 ILR, respectively. Upon further stretching of the image in Figure 4.1 we can also detect the faint leading wake of Prometheus in R/2004 S2, which complicates any attempts to identify resonant structures that might exist there. The Prometheus ringlet shows a distinct offset in radius and a variation in brightness on either side of the central images corresponding to when Prometheus passed through the longitudinal region captured in the image-movie. Additionally, radial scans of images taken after Atlas passed by (right after Prometheus) show a slightly wider R/2004 S1 region.

As described above, the various trends in reflectance caused by different changes in lighting geometry within an image sequence and between sequences obtained over the course of the mission complicate efforts to quantify the amplitudes of these structures. To best facilitate comparisons between observations without compromising the integrity of the data we use a simple but robust normalization procedure. While a third-order polynomial fit to individual radial scans can reasonably remove these trends, it cannot without also adversely altering the appearance of the subtle structures we are interested in. Hence, we found that the best solution to create a set of normalized profiles within an image sequence is to subtract a linear trend in reflectance with time at each radius across the mosaic. This accounts for variation in brightness across images taken from drifts in lighting geometry during an image sequence while preserving any periodic variations due to the resonant structures. The ideal result is a vertically flat Roche Division map (no brightness slope with time) at radii where no structures occur. This method can cause issues near the edges of the A ring, F ring, and Prometheus ringlet, so we limit the normalization to the region of the Roche Division stretching from $137,000-139,100$ km. Finally, for each Roche Division observation we determine the amplitude of the $m = -3$ longitudinal brightness variations by fitting the data in a radius vs. phase (see Equation 4.3) mosaic to a sinusoid at every radius. The brightness amplitude at each radius is normalized to a fractional amplitude by comparing it to the average brightness level of the

Roche Division at that radius for each observation. We present corrected maps of the Roche Division from every data set (or combination of data sets) included in Table 4.1 whose duration is longer than ~ 7 hours in Appendix G.

For an example, in Figure 4.3 we show the normalized Roche Division map and fractional variation in ring brightness vs. radius during Rev 281. This observation sequence had particularly favorable viewing geometry (low B and high α) and so provides the clearest example of the resonant structure in the Roche Division. The strongest structure peaks around $137,420$ km, near the edge of the A ring with a pattern speed of 798.9 $^\circ\text{day}^{-1}$. Similarly strong patterns are present near this location both in 2006 and since 2016.

In general, the structures in the Roche Division occur in a region from just outside the edge of the A ring to the R/2004 S2 ringlet. In certain observations, bright and dark diagonal banding almost appears to cover this entire range of nearly $2,000$ km as one structure. In fact, diagonal bands in the mosaic for Rev 281 of Figure 4.3 can be traced from $137,200 - 138,100$ km and only show possible interruptions around $137,700$ km where Atlas orbits. Other observations show more distinct substructures at each radial region. We provide a brief summary of the lengthier observations in Figure 4.5 and more detailed figures of each of these observations in Appendix G.

4.5 Results

We can characterize the Roche Division patterns using the radius of the peak amplitude and the equivalent pattern speed given by Equation 4.4, along with the structure's peak amplitude and width. Figure 4.4 is a zoomed in look at the strongest structure of Rev 281 from Figure 4.3. The top panel is a mosaic of the observations and the middle panel is a mosaic modeled using Equation 4.5. After fitting the actual fractional brightness variations with a Lorentzian in the bottom plot, we can constrain the damping length L (here, the half width at half maximum), the fractional amplitude A, and calculate the resonance strength β at the exact resonance ($\delta r = 0$) using Equation 4.6. We can then use these parameters to estimate properties of the perturbation.

In Table 4.2 we present the spectrum of the strongest patterns in observation sequences longer than half a local orbital period (~ 7.25 hours) by noting their radii and the corresponding pattern speeds (and equivalent period). We also provide the relevant resonance strength parameters and estimate an effective perturber mass using Equation 4.2 and magnetic field oscillation amplitude using Equation 4.19. The exact particle properties of the Roche Division are unknown at this time and are beyond the scope of this work. To provide an order of magnitude estimate of the magnetic oscillation amplitude $B_{\theta 0}$, we can re-express the charge-to-mass ratio as $3\epsilon_0\Phi/\rho_g s^2$, where ϵ_0 is the permittivity of free space, and assume a particle size $s = 5$ μm (Showalter et al., 1998), density $\rho_g = 1$ g/m^3, and electrostatic potential $\Phi = 10$ Volts (Farrell et al., 2012), consistent with prior estimates for dusty particles near the main rings (Mitchell et al., 2013).

Both the peak amplitudes and widths of these structures vary dramatically among the various observations. For example, considering just the innermost structure we can see that the resonance strength appears to vary by over an order of magnitude. Observations like 033, 036, 268a, and 281 (see Figures

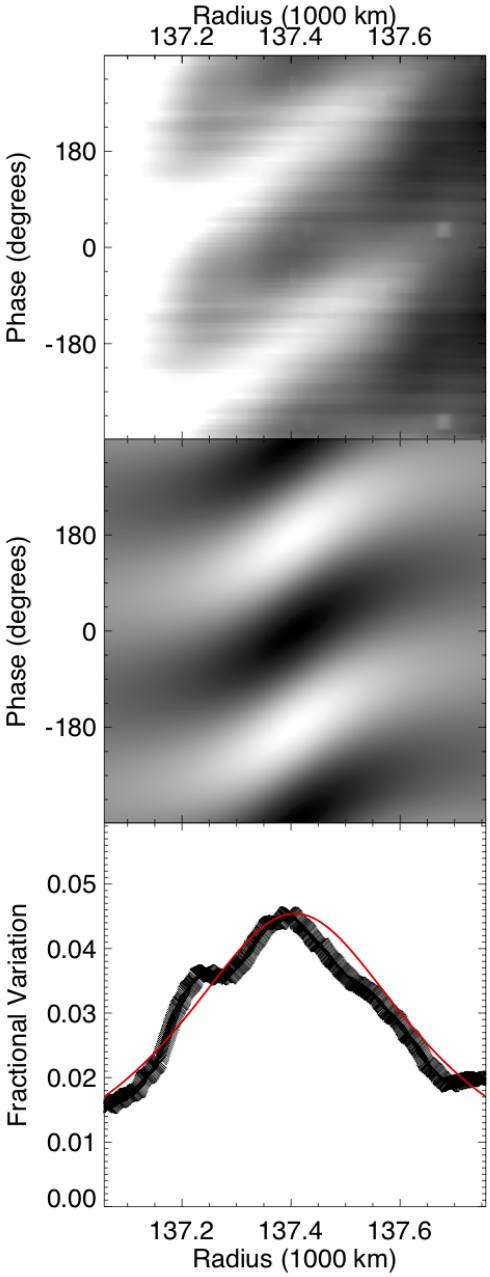

Figure 4.4: The top panel is a small map of the high amplitude structure of Rev 281 from Figure 4.3, but with a pattern phase axis rather than time to conform with Equation 4.5. The middle panel is the model of the region made with Equation 4.5, after approximating L as the full width at half maximum from a Lorentzian fit (red curve) to the bottom panel showing the fractional change in brightness across the structure at each radius.

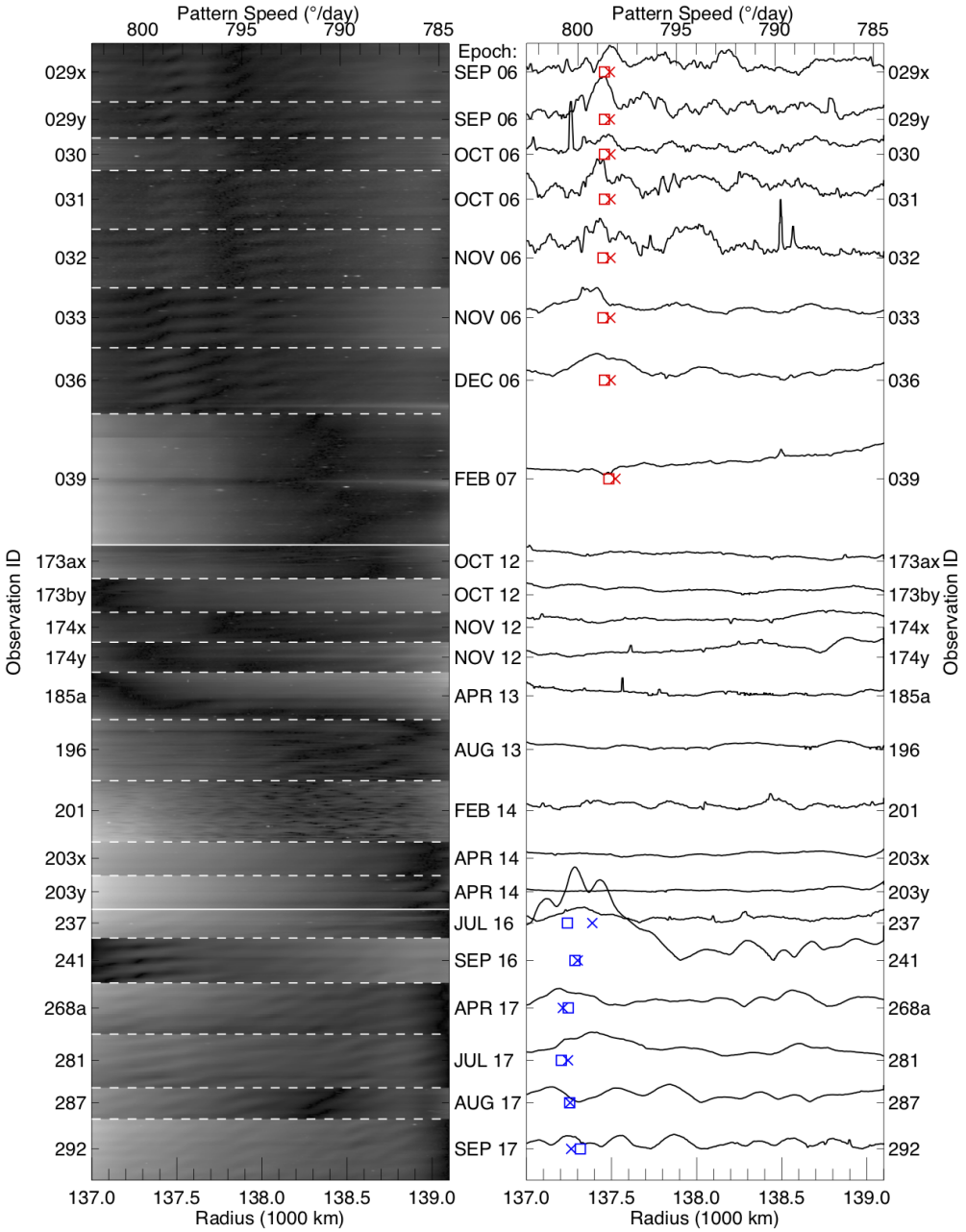

Figure 4.5: This plot is a summary of Roche Division maps and their $m = -3$ fractional amplitudes of observations taken over the course of the *Cassini* mission whose durations are 7 hours or longer. Each map is scaled to the same time scale (height), where for example Rev 196 is about one local orbital period ($\sim$ 14.5 hours). Subsequent observations are stacked on top of one another sequentially in time, marked by the month and year the observation took place, and delineated by dashed lines or a solid line to separate out the main epoch ranges. The curves in the right portion of the figure are measures of the fractional amplitudes $\frac{amplitude\ of\ brightness\ variation}{average\ brightness}$ at each radius. These curves show the abundance of peaks occurring when appropriate northern (blue) or southern (red) SKR (X) and MAG(square) periods may be affecting the region. See Appendix G for larger plots of each observation.

Table 4.2: Peak pattern speeds and perturber strengths

Image movie ID	Date Month Year	Radius r (km)	Pattern speed Ω_p ($^\circ$day^{-1})	Pattern period (hours)	Peak fractional amplitude A	Damping length L (km)	Resonance strength β (km^2)	Effective perturber mass M_{Mimas}	Magnetic field oscillation amp. $B_{\theta 0}$ (nT)
029x	SEP 2006	137350	799.5	10.81	0.031	40	50	0.1	1.0
029x	SEP 2006	137500	798.3	10.82	0.051	80	290	0.4	6.2
029x	SEP 2006	138180	792.4	10.90	0.045	80	310	0.5	6.4
029y	SEP 2006	137320	799.8	10.80	0.039	30	50	0.1	1.0
029y	SEP 2006	137440	798.7	10.82	0.070	70	330	0.5	7.1
030	OCT 2006	137470	798.5	10.82	0.032	70	140	0.2	2.9
031	OCT 2006	137420	798.9	10.82	0.063	60	240	0.4	5.1
033	NOV 2006	137380	799.3	10.81	0.048	110	620	0.9	13.3
036	DEC 2006	137440	798.8	10.82	0.042	190	1510	2.3	32.0
036	DEC 2006	138040	793.6	10.89	0.022	120	310	0.5	6.5
237	JUL 2016	137320	799.8	10.80	0.024	160	630	0.9	13.4
241	SEP 2016	137120	801.6	10.78	0.099	130	1600	2.4	34.2
241	SEP 2016	137290	800.1	10.80	0.149	110	1660	2.5	35.4
241	SEP 2016	137430	798.8	10.82	0.129	130	2090	3.1	44.2
268a	APR 2017	137230	800.6	10.79	0.029	170	800	1.2	17.1
268a	APR 2017	138140	792.7	10.90	0.016	110	210	0.3	4.3
268a	APR 2017	138580	788.9	10.95	0.028	120	420	0.6	8.6
281	JUL 2017	137420	798.9	10.81	0.044	270	3200	4.8	67.8
281	JUL 2017	137920	794.6	10.87	0.021	240	1150	1.7	23.9
281	JUL 2017	138600	788.7	10.95	0.027	120	390	0.6	7.9
287	AUG 2017	137140	801.4	10.78	0.026	100	270	0.2	5.7
287	AUG 2017	137540	797.9	10.83	0.024	120	330	0.5	6.9
287	AUG 2017	137840	795.3	10.86	0.030	110	380	0.6	8.0
292	SEP 2017	137250	800.4	10.79	0.022	80	130	0.2	2.7
292	SEP 2017	137550	797.8	10.83	0.023	60	80	0.1	1.7
292	SEP 2017	137870	795.0	10.87	0.024	76	140	0.2	2.9

Using a Mimas mass of $3.7493(\pm 0.0031) \times 10^{19}$ kg (Jacobson et al., 2006). The error of these measurements are dominated by systematic offsets that are difficult to quantify a priori.

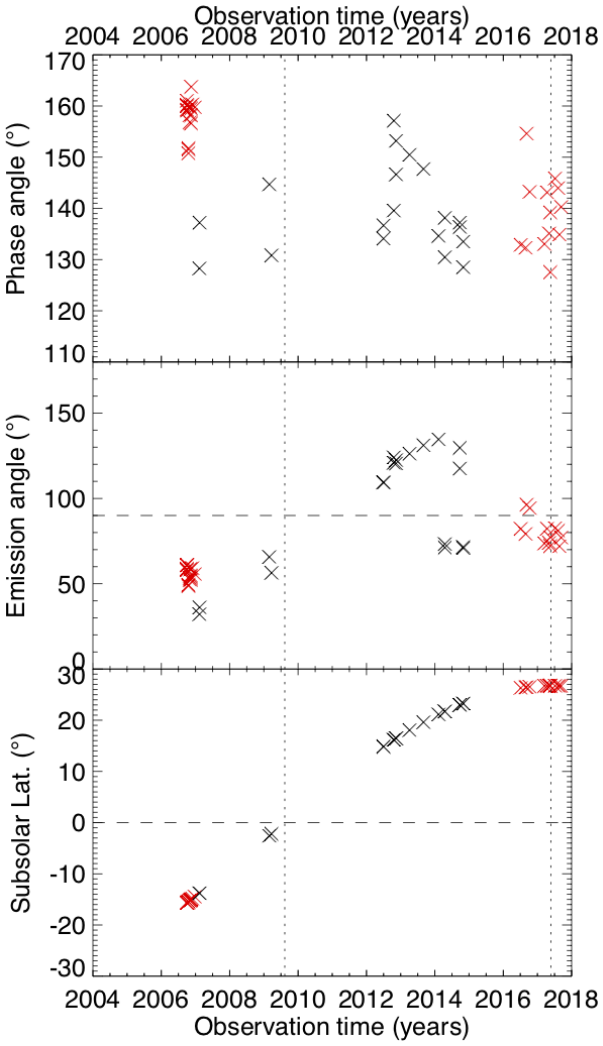

Figure 4.6: These plots show the phase angle (top), emission angle (middle) of all Roche Division observations in Table 4.1, and Saturn's subsolar latitude (bottom) versus the time of each observation. The red or dark symbols correspond to observations where the longitudinal brightness variations were visible in the Roche Division. The vertical dotted lines mark Saturn's equinox in 2009 and solstice in 2017. The horizontal dashed line marks 0° and 90° in the relevant plots. The lack of brightness variation detections in many observations cannot easily be attributed to their photometric angles.

G.6, G.7, G.20, and G.23) have a single radially broad structure between Atlas and the A ring, while others, 029x, 241, 287, and 292 are made up of multiple narrower structures (see Figures G.1, G.19, G.24, and G.26). This may be related to the strength of the rotating PPO current systems. Alternatively, some of these changes could be because the observations were obtained with different lighting geometries, which can affect the appearance of these structures. For instance, observations taken at different phase angles are sensitive to different particle sizes due to their light scattering properties.

On a global scale, in Figure 4.5 patterns can be seen in all the observations from 2006 and 2016-2017, and no similar patterns are detected in 2012-2014. Close examination of the lighting and viewing conditions reveal that these alone cannot explain the overall variable presence of the patterns. Figure 4.6 shows the photometric angles for each observation throughout the mission. The red X's correspond to the observations where we are able to detect periodic structures in the Roche Division. The majority of observations in 2006 were taken from very high phase angles ($\alpha > 150°$), but the remaining observations were taken at a large range of phase angles ($\alpha \sim 130 - 160°$). Lower phase angle observations ($\alpha < 140°$) are generally less likely to reveal the structures, and reveal them with less detail. However, we cannot attribute the lack of structure identification from 2009-2015 to a lack of appropriate phase angle viewing, because several Revs (173by, 174x, 174y, 185a, and 196) have phase angles $\alpha > 140°$ and cover a sufficient length of time (at least half of a local orbital period), conditions under which patterns could be seen in 2016-2017.

The best candidate for missing the structure due to lighting geometry might be due to a combination of phase angle and the emission angle. These structures are most obvious in sequences with particularly high phase angles ($> 150°$) or with emission angles closest to 90° (i.e. low ring opening angles $|B| < 10°$). While there isn't an obvious missed opportunity of comparable lighting geometry during the 2009-2015 epoch of no Roche Division structures, we should examine this possibility closely. Notice in the central plot of Figure 4.6, we cannot compare sequences having the same emission angle between each of the three epochs, as we are able to with phase angles. Emission angles $e < 90°$ correspond to observations taken from the north side of Saturn's ring-plane. During the first observations of the Roche Division, in late 2006, Saturn's southern hemisphere was illuminated by the Sun, so these observations with emission angles $e \sim 50 - 60°$ were taken from the unlit side of the rings. Similarly, several observations after equinox were taken from the unlit side of the rings, but from the south side of the ring plane. However, this spread in emission angles ($e \sim 110 - 140°$) does cover a similar range in absolute ring-plane opening angles $|B| = |90° - e| \approx 35°$ on the unlit side of the rings. If the structures were present all the time, and only visible under optimal lighting geometry, there is no reason that we shouldn't see the structures in Rev 173by and 174x when we can see them in Rev 031 having nearly identical lighting geometry (see lighting geometry in Table 4.1 and maps in Appendix G). Therefore, we conclude the presence of the Roche Division structures must be due to changes in the frequencies of the forces perturbing them.

4.6 Discussion

4.6.1 Pattern speeds and locations

The seasonal appearance of resonant structures in Saturn's Roche Division fits in well with the observed seasonal variations in Saturn's PPO rotational modulations. This is demonstrated in Figure 4.7, which shows the rotation speeds of the northern (blue) and southern (red) PPO systems derived from the SKR (solid line) and MAG (dashed line) data over the *Cassini* mission (Ye et al., 2016, 2018; Provan et al., 2016, 2018). An equivalent scale of PPO periods is shown on the right hand vertical axis. As briefly indicated in Section 4.2, the rates were well separated early in the mission under Saturn southern summer conditions at $816°\text{day}^{-1}$ for the weaker northern system and $\sim 800°\text{day}^{-1}$ for the stronger southern system, before converging towards near-equal rates with near-equal amplitudes across vernal equinox in mid-2009. An interval of variable but near-equal rates with variable amplitudes then ensued between mid-2010 and mid-2013 (Provan et al., 2013; Fischer et al., 2015), though the northern rate $\sim 812°\text{day}^{-1}$ generally remained larger than the southern rate $\sim 809°\text{day}^{-1}$, before it coalesced at $\sim 808°\text{day}^{-1}$ between mid-2013 and mid-2014. The rates then separated again, with the now-stronger northern system slowing to $\sim 800°\text{day}^{-1}$ while the weaker southern system remained near $\sim 809°\text{day}^{-1}$. The Roche Division structures reported by Hedman et al. (2009a) were observed during the initial interval of well-separated rotation rates, as indicated by the left hand dark gray band in Figure 4.7, when the period of the stronger southern system was $\sim 798°\text{day}^{-1}$. However, during the extended post-equinox interval of near-equal northern and southern system rates $\sim 810°\text{day}^{-1}$, all observations of the Roche Division show no evidence of such periodic brightness variations, as indicated by the central gray band in Figure 4.7. (See Appendix G for the individual maps and fractional amplitudes of these observations.)

During the time between early 2009 and late 2014 when we observe no ring structures, both PPO rates are above $805°\text{day}^{-1}$ (Fischer et al., 2015; Ye et al., 2016; Provan et al., 2016). Thus, an appropriately commensurate 3:4 OLR with a pattern speed greater than $805\ °\text{day}^{-1}$ would be located interior to the outer edge of Saturn's A ring and unsuitable to produce resonant structures in the Roche Division. Horizontal dashed lines in Figure 4.7 show the pattern speed at $\sim 805\ °\text{day}^{-1}$ for such a resonance at the outer edge of the A ring, as well as at reference radii of $137,000$ and $137,500$ km in the region outside the edge of the A ring. We first observe the reappearance of the Roche Division structures in Rev 237 on July 1st, 2016 and they are apparent in all later observation sequences. The closest prior observation to Rev 237 is Rev 209 in October 2014 just after the rate of the northern component began to slow down after the interval of coalesced periods.

Additionally, during 2006 and 2016-2017 the PPOs of the stronger systems have pattern speeds that coincide with the location of the largest fractional variations in the Roche Division. This is most notable between the observations in 2006 when the southern PPO rate slowed to below $799\ °\text{day}^{-1}$ and the observations in 2017 when the northern PPO rate was around $800\ °\text{day}^{-1}$. In the 2006 observations the location with the highest fractional brightness variations is further out into the Roche Division around $137,400 - 137,500$ km while in 2017 some strong structures appear even closer to the A ring around $137,100 - 137,300$ km (See Figure 4.5). This suggests that the structures in the inner Roche Division

are tied to the presence of the variable PPO rates.

In fact, we find that the innermost Roche Division structure is in sync with the PPOs. In Figure 4.8 we show four of the best observations of the mission mapped to the appropriate MAG PPO longitude system. In their determination of the PPO periods the magnetometer team also defines a longitude system and tracks the phases of both PPO systems (Provan et al., 2018). For each ring observation shown we determine the longitude of each ring profile in the appropriate north or south PPO system at the time the image was taken. See Appendix F for a complete description of the PPO longitude systems and how we bring our ring observations into this system to create Figure 4.8. The effective MAG PPO resonant radius for the northern (blue) and southern (red) systems are marked with dashed lines on the maps. The fractional variation of the brightness profile at each of these radii is plotted below with the same color scheme for north/south and a different symbol for each ring observation. The SKR maximum emission in this MAG longitude system is marked by the vertical dashed lines with appropriate symbols on each end (Ye et al., 2018). The minimum fractional variations of the ring pattern appears to be consistently at quadrature with the PPO system that is responsible for the resonance in the Roche Division at any given time. The zero point of the PPO longitude system is defined where the oscillating magnitude of B_θ is a minimum in the northern PPO system and where B_θ is a maximum in the southern PPO system. Strangely, we do not see a 180° offset between the northern and southern PPO affected ring structures. Nonetheless, the coherence of these structures at the drifting resonant radius is suggestive of a clear relation between the PPO and the inner Roche Division.

The connection between the outer Roche Division structures, with slower expected pattern speeds, and the PPOs is less clear. We do not understand how this phenomena can perturb an almost 2000-km-wide radial span in the Roche Division. It is possible that the outer structures are due to other longer periods, but these are not seen in the MAG and SKR data. Also, if they are due to different periodic forces they would not necessarily disappear at the same time as the faster PPO signals. Our detection of resonant structures so far from the exact PPO resonance could be due to unexpectedly long propagation from the resonant radius.

Perhaps these extensive dusty structures in the Roche Division are generated by similar phenomena as the spokes. The dusty spokes in Saturn's B ring, which extend over a radial range up to $10,000$ km (Smith et al., 1981), are also related to the PPO periods (Mitchell et al., 2013). The spokes in the B ring and the resonant Roche Division structures certainly have some connection, but the dust making up the B ring spokes must be levitated above and below the numerous larger ring particles (Mitchell et al., 2006), introducing added complexity to the dusts' response to resonant forcing from the PPO near co-rotation. Indeed one might wonder why spoke-like structures do not form in the outer A ring when the PPO periods are both $\sim 810°\text{deg}^{-1}$. There may be a different response to the PPO by dust within dense rings and dust in dust-dominated rings preventing propagation across this boundary. At times when the PPO resonant radius falls directly in a dust-dominated ring, the structures may be able to propagate across the dusty region, with some interruptions from embedded moons and other gravitational influences. This is an idea that will need to be explored more explicitly in a future work.

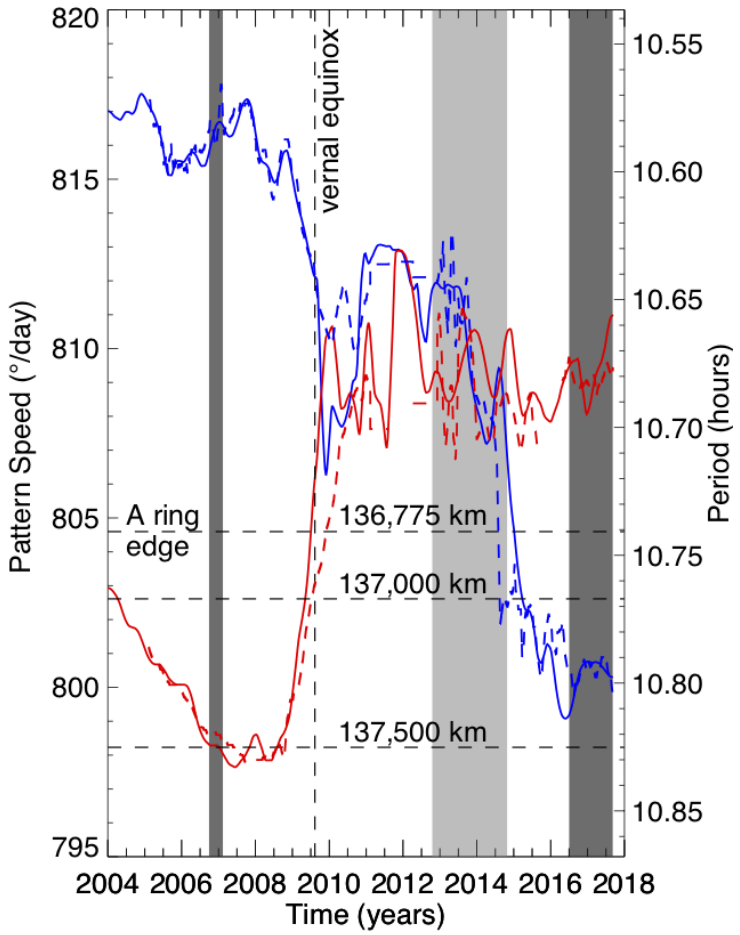

Figure 4.7: This plot shows the rotational modulation rates of the Southern (red) and Northern (blue) hemispherical components of the SKR (Ye et al., 2018) (solid) and MAG (Provan et al., 2018) (dashed) versus time. Light horizontal dashed lines mark the effective edge of the A ring edge (near 805 $^\circ\text{day}^{-1}$) , and the pattern speeds for reference radii at $137,000$ and $137,500$ km. A vertical dashed line marks the vernal equinox. The vertical gray bands encompass periods spanned by the observations in Table 4.1. The darker bands around 2006 and 2016-2017 reflect the observation epochs when we have clear detections of brightness variations in the Roche Division. The lighter band covers the observation epoch around 2012-2014 when there wasn't a single detection of brightness variations in the Roche Division. This suggests that the presence of periodic brightness variations in the Roche Division is correlated with times when there are suitably long magnetospheric periods.

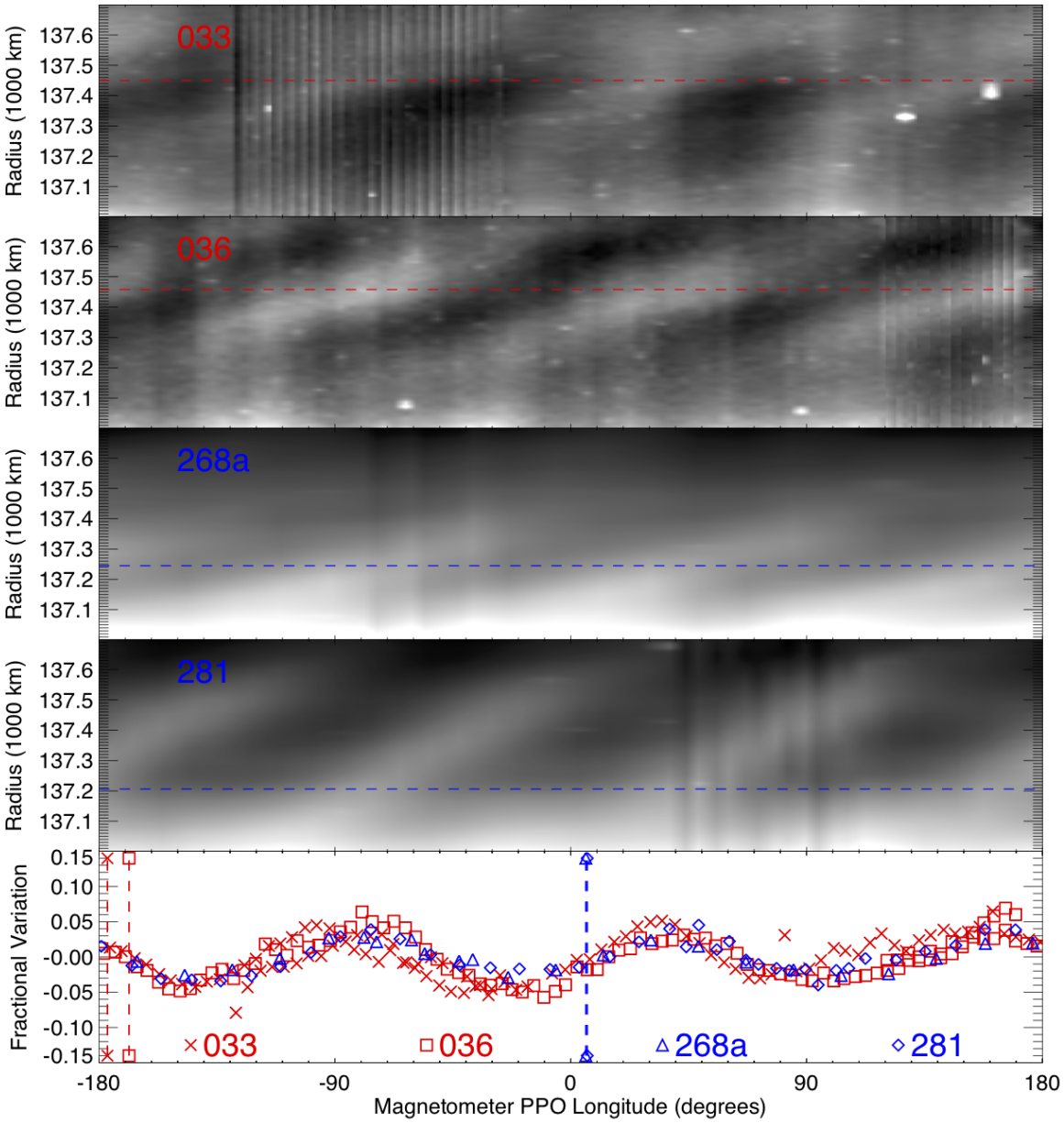

Figure 4.8: The top four panels contain maps of four Roche Division observations using the MAG PPO longitude system, see Appendix F (Provan et al., 2018). Dashed lines mark the resonant radius of the southern (red) or northern (blue) PPO period at the time of the ring observations. In the lower plot are the brightness profiles of the ring map at the resonant radius marked above. The vertical axis in this plot represent the fractional variation above or below the mean brightness at the resonant radius. The vertical dashed lines in the bottom plot mark the longitude of the maximum SKR emission in the MAG PPO system for each observation (Ye et al., 2018). The innermost Roche Division structure appears to be in sync with the PPO longitude.

4.6.2 Perturbation strengths

Additional insights into the sources of these perturbations can be extracted from their amplitudes. The structures' typical peak amplitudes are $2-7\%$ of the local mean Roche Division brightness with damping lengths of $\sim 50-300$ km (see Table 4.2). If these structures were generated by gravitational forces, then hypothetical perturber masses cover a wide range, from nearly five Mimas masses to just a tenth of a Mimas mass. Again, the innermost structure is perturbed most heavily. However, we should recall that these mass estimates are the result of an incomplete phenomenological model. Applying this simple dissipation model to the 8:7 Mimas ILR in the G ring, we measure the mass of Mimas to be 2.5 times the actual Mimas mass, so these results are likely just an order of magnitude estimate of an actual perturber mass (Hedman et al., 2009a). On the other hand, if these perturbations are due to oscillations in the magnetic field, then our estimates of the magnetic field oscillation amplitude $B_{\theta 0}$ are within an order of magnitude of the Provan et al. (2013, 2016, 2018) results. This provides further evidence that the perturbing forces are electromagnetic rather than gravitational.

Considerations of the expected gravitational effects of other moons on the Roche Division confirms that the perturbations responsible for producing these patterns are very strong and likely non-gravitational. Saturn's moons Janus and Epimetheus are similar-mass co-orbital satellites that exhibit horseshoe orbits with an 8 year period (Harrington & Seidelmann, 1981). The Janus/Epimetheus 7:6 ILR is located on the edge of the A ring and shapes its 7-lobed wavy edge (El Moutamid et al., 2016). This resonance, along with the combined torques from several satellite resonances in the outer region of the A ring, confines Saturn's main rings (Tajeddine et al., 2017). While the exact location of the Janus and Epimetheus resonances drift slightly over their 8 year orbital swap, the 8:7 ILR always occurs in the same part of the outer Roche Division and so might be expected to shape that region. However, there are no obvious 8-lobed or canted structures moving at the moons' orbital rates in any of the image-movies presented here.

Instead, the brightness variations of a 3:4 OLR appear to dominate this location (see Rev 281), but the structure is consistently not as clean as those in other radial locations. The Janus/Epimetheus 8:7 ILR should be even stronger than its 7:6 ILR, but the lack of an 8 lobed structure similar to that found in the G ring at the Mimas 8:7 ILR is consistent with high gravitational masses needed to produce the 3:4 resonant structures. Thus, the strength of the 3:4 OLR with Saturn's PPOs must be even greater if it is the dominant perturbing force in this region. This further reinforces the conclusion that these structures are the result of electromagnetic perturbations associated with Saturn's rotating PPO systems. In fact, our measured values of β for the 3:4 OLR structures closest to the Janus/Epimetheus 8:7 ILRs are 420 km^2 and 390 km^2 for Revs 268a and 281. These are more than 10 times larger than those predicted for the Janus 8:7 ILR using the mass found by Jacobson et al. (2008).

As mentioned earlier, leading Prometheus wakes are also observed in the R/2004 S2 ringlet near this location adding to the competing perturbing forces. One might also expect, due to the close proximity of the Roche Division dust bands to Atlas and Prometheus, that gravitational satellite wakes should dominate the Roche Division's appearance. Upon close inspection of Figure 4.1, we can see the wakes leading Prometheus in the outer band R/2004 S2. Satellite wakes have azimuthal wavelength $\lambda = 3\pi\delta a$

related to the radial separation of the satellite and the ring material $\delta a = |a - a_s|$ (Cuzzi & Scargle, 1985; Showalter et al., 1986; Chancia & Hedman, 2016). This wavelength is $\sim 2^\circ$ in longitude compared to the 120° variations of the 3:4 OLR. We have not detected any evidence of satellite wakes in the dust around Atlas. Some of the material in Atlas' vicinity could be co-rotating like the Prometheus ringlet (Hedman & Carter, 2017) or the Encke Gap ringlets (Hedman et al., 2013), but we have not seen any evidence supporting either arrangement.

4.7 Summary and conclusions

In this work we have tracked the presence of dusty periodic structures in the Roche Division throughout the course of the *Cassini* mission. We find these structures are present when the 3:4 OLR with Saturn's seasonally-varying magnetospheric periodicities are in this region. By analyzing the resonant response of the rings and applying a simple model of an oscillating magnetic field we are able to estimate oscillation amplitudes comparable to those observed with *Cassini's* magnetometer instrument.

It is evident that electromagnetic forces dominate the perturbations in the Roche Division. The effect of nearby small satellites and satellite resonances are mostly washed out by the dominant influence of the 3:4 OLR with the rotating magnetic field perturbation. The varying nature of the magnetospheric periodicities is coincident with the presence of Roche Division structures, providing further evidence of this association. Further investigation of the magnetospheric observations connected to the Roche Division and investigations of other dusty ring structures could resolve the issue of how these patterns span a wide range of radii. This could be relevant to studies of other expansive dust systems, like protoplanetary disks.

As previously discussed, the ring regions where the most analogous structures have been detected are the G ring and D ring. While the dusty resonant structure in the G ring is known to be caused by the 8:7 ILR with Mimas, the D ring seems to be perturbed by the same phenomena as the Roche Division, but at the 2:1 ILR with the PPO periods (Hedman et al., 2009a). However, the D ring spans a much wider radial range of pattern speeds matched by various phenomena associated with Saturn's rotation. While the Roche Division only covers the slowest rotation periods of the PPO, the D ring covers the full range of these seasonal magnetospheric periods and the full range of Saturn's latitudinal wind speeds. In fact, the prevalence of resonant structures resulting from 2:1 ILRs warrants a separate work. However, we note that the faint region of the D ring between the D72 and D73 ringlets appears to be responding to the same phenomena we report on here for the Roche Division.

The presence of ring structures at these particular resonances with the PPO makes sense because the D ring and Roche Division contain large populations of dust. The remaining resonances with various $|m|$ live mostly in the dense A, B, and C rings. The only other such PPO resonance falling in a dusty ring is the 2:3 OLR ($m = -2$) located near the inner edge of the Janus-Epimetheus ring ($\sim 149,000$ km from Saturn's center). This location has not been monitored at an extent comparable to D ring or Roche Division, but our brief investigation of the limited data revealed no obvious structures. As mentioned previously, the B ring spokes may be an expression of the PPO perturbations surrounding PPO co-rotation. Future studies should examine the connections between the B ring spokes and these

patterns in the D ring and Roche Division, and why there are no dusty spokes or similar structures around other PPO resonances like the 3:2, 4:3, and 5:4 ILR, or 4:5 OLR.

4.8 Acknowledgements

...as they appear in the official publication.

This work was supported by NASA through the Cassini Data Analysis Program NNX15AQ67G. Work at the University of Leicester was supported by STFC Consolidated Grant ST/N000749/1. We thank Georg Fischer for helpful comments on an earlier version of this manuscript. We are grateful for helpful conversations with Douglas P. Hamilton concerning Lorentz resonances and quantifying their strengths. We also thank the Cassini project and imaging team for acquiring the data for this work. We would also like to thank two anonymous reviewers for their helpful suggestions that ultimately improved the clarity and consistency of this manuscript.

Chapter 5: Conclusions

In this work I found new evidence that two previously unexplained narrow rings may be perturbed by tiny moonlets in the Uranian ring system (Chapter 2). My studying of the Uranian ring occultations also culminated in the first publication of measured influence of a Uranian moon's resonant perturbations on one of the planet's ten dense rings (Chapter 3). This discovery allowed for the first mass and density measurements of one of the thirteen small inner moons of Uranus. Finally my work on Saturn's Roche Division ties the variable presence of periodic dusty structures to Saturn's seasonal magnetospheric periodicities (Chapter 4). Specifically, we found that these dusty structures are likely produced by nanotesla magnitude oscillations of Saturn's axisymmetric magnetic field, consistent with *in situ* measurements made with *Cassini's* magnetometer. Together, these findings highlight the advance in using remote sensing observations of planetary rings to learn about the interconnected components of the planetary system, where the rings themselves provide a natural instrument for measuring the various influential forces in their environments.

Of course, many questions concerning planetary rings and their home planetary systems remain and there is much work to be done with the data we have already obtained. Our ongoing work with the Uranian system includes newly compiled occultation data containing the dense main ring widths (McGhee-French et al., 2019). This data will be fundamental in determining the influence of resonances on the edges of the ϵ, δ, and γ, as well as searching for unexpected signatures in the remaining ring widths. Our preliminary investigations have found evidence of additional normal mode oscillations in the complex γ ring, including a poorly understood $m = -1$ mode. I recently presented preliminary analysis of a complete re-examination of the *Voyager 2* imagery (Chancia & Hedman, 2019). We found measurable azimuthal brightness variations in the ϵ and γ rings due to their resonances with Ophelia (see Figure 5.1). This finding combined with the analysis of ring widths will provide the first documented measure of these resonances perturbations on the rings and may yield the masses of two more small inner Uranian moons. Our analysis of the high-phase-angle images has also revealed a series of distinctly narrow dusty rings between the δ and γ rings that fall nearly coincident with a series of Cordelia resonances. The short exposure images (~ 5 seconds, compared to the famous 96 second exposure that revealed the dusty Uranian rings for the first time) in which these rings subtly appear have not previously been reported on in the literature and were likely overlooked due to their poor signal to noise. Nonetheless, many are clearly visible after some basic processing and they are utterly perplexing.

Concerning Saturn's dusty rings, there are a number of follow up studies in the works or worth considering. In parallel to our study of the Roche Division images, we have presented preliminary results on the resonant brightness variations in Saturn's D ring (Chancia & Hedman, 2018). As mentioned in Chapter 4 the area of the D ring surrounding the D72 ringlet is also subject to the influence of Saturn's planetary period oscillations, but at the 2:1 inner resonance. In fact, this ring spans a region where a number of connections with the planet's rotation are possible. In Figure 5.2 we show the rotation rate and period of Saturn's northern and southern PPO (both SKR and MAG data), latitudinal winds, and bulk interior, compared to a sample radial profile of image N1866440201. Each period or pattern speed corresponds to the radius of a potential 2:1 resonance in the D ring. To effectively address the array of resonant structures spanning from $\sim 70,000$ to $73,000$ km from Saturn center it is sensible break the

region down into the three regions with different circumstances. First, a region interior to D72 where the only possible perturbation is a 2:1 resonance with Saturn's fastest latitudinal wind speeds. Second, the region outside of D72 spanning the full range of Saturn's seasonal PPOs. Third, is the D72 ringlet itself. In the 2:1 resonance pattern speed space, D72 is currently positioned on top of Saturn's deep bulk rotation rate, nearly perfectly set between the range of slow and fast wind speed latitudinal bands, and is skirted on its outer edge by the northern hemisphere PPO rate in the early part of the *Cassini* mission.

Due to the number of possible perturbing forces and their possibly time variable influence, analysis of these structures is considerably more difficult than those in the Roche Division. Our results of Chapter 4 also showed that resonant dusty structures can span over substantial radial regions if unhindered by stronger features. This further complicates deciphering signatures in the D ring, which rarely feature persistent structures between observations even just a few months apart. With a better understanding of the forces at work in this region of the D ring, we may be able to isolate the structures caused by the dominant perturbing forces. Recent work following the *Cassini* grand finale has revealed many other complex connections between the innermost D ring and the planet's magnetosphere (Roussos et al., 2018; Krupp et al., 2018; Kollmann et al., 2018; Provan et al., 2019) and atmosphere (Waite et al., 2018; Perry et al., 2018).

The results of Chapter 4 should also prompt future theoretical investigations of the radial propagation of structures within dusty rings. Saturn's B ring spokes are also known to extend for hundreds of kilometers. Further analysis of spoke observations and searches for spokes among the other rings in images obtained over the course of the *Cassini* mission may reveal connections with the D ring and Roche Division.

Finally, future observations of planetary rings include the near and distant possibility of future orbiter and flyby spacecraft at the outer planets and Earth-based telescopes. In the nearest future, the *James Webb Space Telescope* (JWST) is expected to launch in the spring of 2021 (as of June 2019). Plans are approved among the early release science and guaranteed time observing programs to image components of the Jovian and Saturnian ring-moon systems from $0.6 - 28.8$ microns with various instruments. These observations will provide a new means to conduct seasonal studies of the rings and moons. Our team of ring scientists is ready to propose our own general observer science for cycle 1 in the spring of 2020. Our targets will be the rings and small moons of Uranus and Neptune. The spectral capability of JWST will allow for the first high resolution observations of these faint bodies with hyperspectral coverage up to and beyond 2.38 microns. The rings and moons of Uranus in particular are notoriously dark and featureless within current limited multispectral coverage (Karkoschka, 1997, 2001a; de Kleer et al., 2013). Spectra from JWST should provide vast advancement in our knowledge of the composition of the inner Uranian ring-moon system and will allow comparison with the large classical satellites that show hints of water and carbon dioxide ices on their surfaces (Grundy et al., 2006; Cartwright et al., 2015). The observations of Neptune's moons and rings will reveal the native composition of the material around Neptune for the first time (Dumas et al., 2003). These observations are imperative for understanding the formation and evolution of the ice giant ring-moon systems.

Two orbiting spacecraft missions to Jupiter are planned to launch before 2025. The *Europa Clipper* mission managed by NASA and *Jupiter Icy Moons Explorer* managed by ESA. While these missions

are primarily focused on observing Jupiter's icy moons and investigating their subsurface oceans, they will have many opportunities to observe Jupiter's vast dusty rings. These observations will be a great complement to the results of the current *Juno* orbiter mission, which is focused on Jupiter's magnetosphere and gravity field. The bulk of Jupiter's dusty rings are known to be sculpted by its strong tilted dipole magnetic field, plasma drag, and intense solar radiation pressure (Burns et al., 1985; Hamilton & Krivov, 1996; Burns et al., 1999; Horányi & Juhász, 2010). Analysis of observations connecting dusty rings and the planetary magnetic field, magnetosphere, and interior will provide useful comparisons to our work with *Cassini* and the Saturn system.

Looking even further into the future, preparing for NASA's upcoming decadal survey is already underway. An ice giant mission is expected to be a priority for the advancement of the planetary sciences in the 2023-2032 decade. In a recent call for planetary mission concept study proposals a number of concepts were proposed to visit both the Uranus and Neptune systems with various mission class orbiter and flyby spacecraft. Further study of both of these systems is imperative for the continued advancement of ring science looking forward into the middle of this century. In the meantime, we will continue to explore and learn from the data brought back from missions that are now years in the past, and hope for the best concerning the spacecraft on their way to the launch pad.

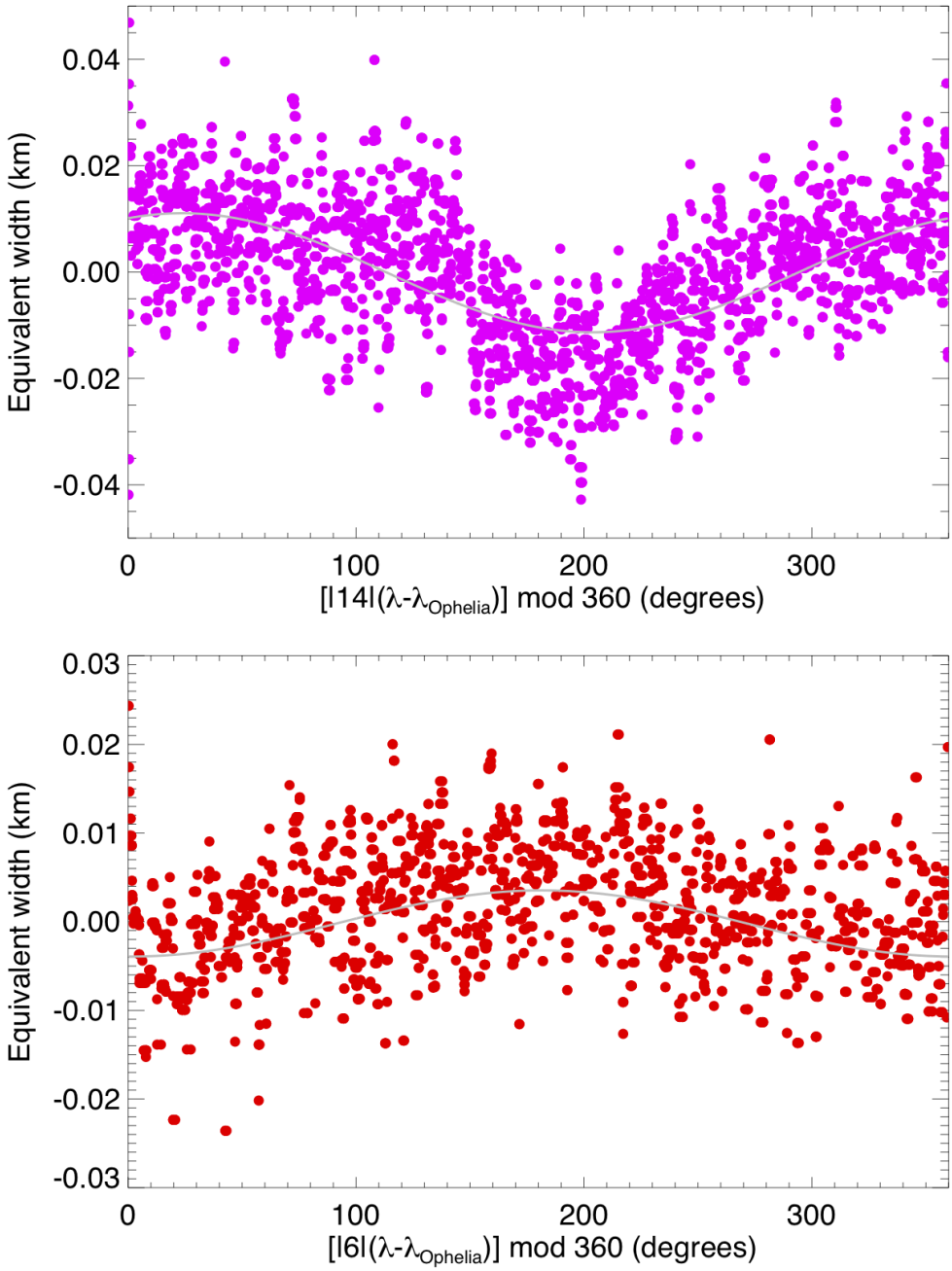

Figure 5.1: Ophelia's 14:13 and 6:5 inner Lindblad resonances fall on the outer edge of the ϵ ring and inner edge of the γ ring respectively. These plots show the Equivalent Width, or radially integrated reflectance, of the rings obtained from a Uranian ring image-movie against their $m-$folded azimuthal distance from Opehlia. The observation clearly captures the subtle variation in brightness of each ring as the $m = 14$ and $m = 6$ edge waves pass by the longitudinal region captured in the images obtained over several hours. The variations in brightness reveal the expected orientation of the resonant induced wavy edge on each ring (Note they occur on opposite ring edges).

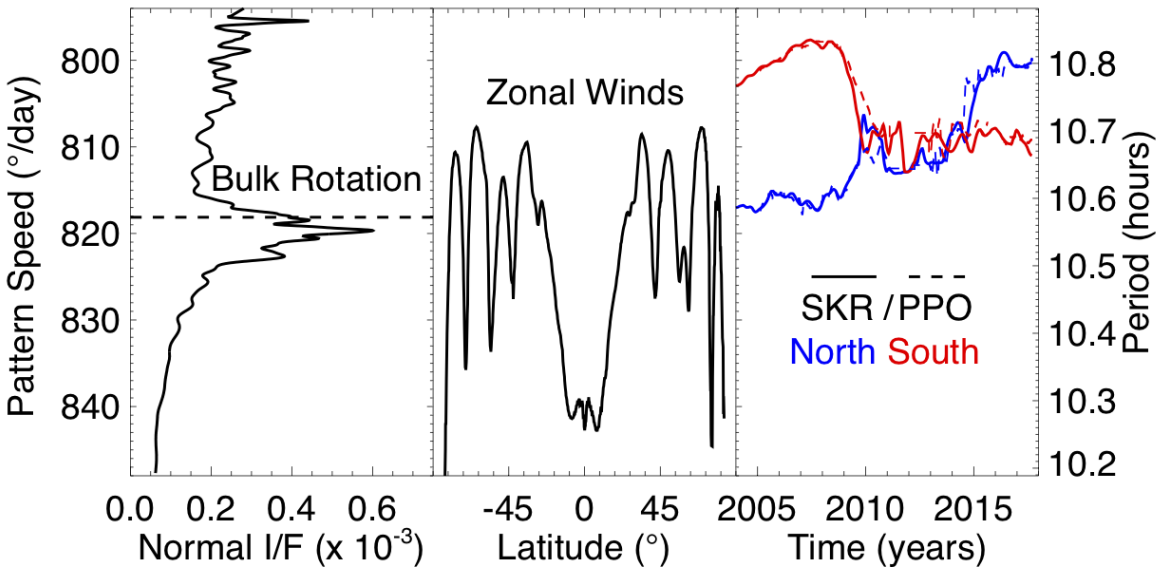

Figure 5.2: Comparing the pattern speed range covered by the D72 region with the various rotation rates associated with Saturn. The D ring reflectance profile from image N1866440201 is in the left panel shown vs. effective $m = 2$ pattern speed range of $70,000$ to $73,000$ km from Saturn's center. Saturn's bulk rotation rate is also marked in the left panel with a dashed line. The middle panel shows Saturn's latitudinal wind speeds and the right panel shows the SKR and MAG PPO periods for each hemisphere over the course of the *Cassini* mission.

References

Acton, C. H. 1996. Ancillary data services of NASA's Navigation and Ancillary Information Facility. Planetary and Space Science, 44, 65, doi: 10.1016/0032-0633(95)00107-7

Aizawa, M., Masuda, K., Kawahara, H., & Suto, Y. 2018. Systematic Search for Rings around Kepler Planet Candidates: Constraints on Ring Size and Occurrence Rate. The Astronomical Journal, 155, 206, doi: 10.3847/1538-3881/aab9a1

Aizawa, M., Uehara, S., Masuda, K., Kawahara, H., & Suto, Y. 2017. Toward Detection of Exoplanetary Rings via Transit Photometry: Methodology and a Possible Candidate. The Astronomical Journal, 153, 193, doi: 10.3847/1538-3881/aa6336

Andrews, D. J., Bunce, E. J., Cowley, S. W. H., et al. 2008. Planetary period oscillations in Saturn's magnetosphere: Phase relation of equatorial magnetic field oscillations and Saturn kilometric radiation modulation. Journal of Geophysical Research (Space Physics), 113, A09205, doi: 10.1029/2007JA012937

Andrews, D. J., Coates, A. J., Cowley, S. W. H., et al. 2010a. Magnetospheric period oscillations at Saturn: Comparison of equatorial and high-latitude magnetic field periods with north and south Saturn kilometric radiation periods. Journal of Geophysical Research (Space Physics), 115, A12252, doi: 10.1029/2010JA015666

Andrews, D. J., Cowley, S. W. H., Dougherty, M. K., et al. 2012. Planetary period oscillations in Saturn's magnetosphere: Evolution of magnetic oscillation properties from southern summer to post-equinox. Journal of Geophysical Research (Space Physics), 117, A04224, doi: 10.1029/2011JA017444

Andrews, D. J., Cowley, S. W. H., Dougherty, M. K., & Provan, G. 2010b. Magnetic field oscillations near the planetary period in Saturn's equatorial magnetosphere: Variation of amplitude and phase with radial distance and local time. Journal of Geophysical Research (Space Physics), 115, A04212, doi: 10.1029/2009JA014729

Arridge, C. S., André, N., Khurana, K. K., et al. 2011. Periodic motion of Saturn's nightside plasma sheet. Journal of Geophysical Research (Space Physics), 116, A11205, doi: 10.1029/2011JA016827

Bader, A., Badman, S. V., Kinrade, J., et al. 2018. Statistical Planetary Period Oscillation Signatures in Saturn's UV Auroral Intensity. Journal of Geophysical Research (Space Physics), 123, 8459, doi: 10.1029/2018JA025855

Badman, S. V., Andrews, D. J., Cowley, S. W. H., et al. 2012. Rotational modulation and local time dependence of Saturn's infrared H_3^+ auroral intensity. Journal of Geophysical Research (Space Physics), 117, A09228, doi: 10.1029/2012JA017990

Barnes, J. W., & Fortney, J. J. 2004. Transit Detectability of Ring Systems around Extrasolar Giant Planets. The Astrophysical Journal, 616, 1193, doi: 10.1086/425067

Bhattacharyya, J. C., & Kuppuswamy, K. 1977. A new satellite of Uranus. Nature, 267, 331, doi: 10.1038/267331a0

Borderies, N., Goldreich, P., & Tremaine, S. 1984, in IAU Colloq. 75: Planetary Rings, ed. R. Greenberg & A. Brahic, 713–734

Borderies, N., Goldreich, P., & Tremaine, S. 1986. Nonlinear density waves in planetary rings. Icarus, 68, 522, doi: 10.1016/0019-1035(86)90054-0

Bradley, T. J., Cowley, S. W. H., Provan, G., et al. 2018. Field-Aligned Currents in Saturn's Nightside Magnetosphere: Subcorotation and Planetary Period Oscillation Components During Northern Spring. Journal of Geophysical Research (Space Physics), 123, 3602, doi: 10.1029/2017JA024885

Braga-Ribas, F., Sicardy, B., Ortiz, J. L., et al. 2014. A ring system detected around the Centaur (10199) Chariklo. Nature, 508, 72, doi: 10.1038/nature13155

Burns, J. A. 1976. Elementary derivation of the perturbation equations of celestial mechanics. American Journal of Physics, 44, 944, doi: 10.1119/1.10237

—. 1977. Erratum: "An elementary derivation of the perturbation equations of celestial mechanics". American Journal of Physics, 45, 1230, doi: 10.1119/1.11091

Burns, J. A., Cuzzi, J. N., & Showalter, M. R. 1983, in Bulletin of the American Astronomical Society, Vol. 15, Bulletin of the American Astronomical Society, 1013–1014

Burns, J. A., Schaffer, L. E., Greenberg, R. J., & Showalter, M. R. 1985. Lorentz resonances and the structure of the Jovian ring. Nature, 316, 115, doi: 10.1038/316115a0

Burns, J. A., Showalter, M. R., Hamilton, D. P., et al. 1999. The Formation of Jupiter's Faint Rings. Science, 284, 1146, doi: 10.1126/science.284.5417.1146

Carbary, J. F. 2017. Update on Saturn's energetic electron periodicities. Journal of Geophysical Research (Space Physics), 122, 156, doi: 10.1002/2016JA023405

Carbary, J. F., & Krimigis, S. M. 1982. Charged particle periodicity in the Saturnian magnetosphere. Geophysical Research Letters, 9, 1073, doi: 10.1029/GL009i009p01073

Carbary, J. F., Mitchell, D. G., Brandt, P. C., Krimigis, S. M., & Gurnett, D. A. 2011. ENA periodicities and their phase relations to SKR emissions at Saturn. Geophysical Research Letters, 38, L16106, doi: 10.1029/2011GL048418

Carbary, J. F., Mitchell, D. G., Krimigis, S. M., & Krupp, N. 2009. Dual periodicities in energetic electrons at Saturn. Geophysical Research Letters, 36, L20103, doi: 10.1029/2009GL040517

Cartwright, R. J., Emery, J. P., Rivkin, A. S., Trilling, D. E., & Pinilla-Alonso, N. 2015. Distribution of CO_2 ice on the large moons of Uranus and evidence for compositional stratification of their near-surfaces. Icarus, 257, 428, doi: 10.1016/j.icarus.2015.05.020

Chancia, R., & Hedman, M. 2018, in AAS/Division for Planetary Sciences Meeting Abstracts, 117.03

Chancia, R., & Hedman, M. 2019, in AAS/Division of Dynamical Astronomy Meeting, Vol. 51, AAS/-Division of Dynamical Astronomy Meeting, P9

Chancia, R. O., & Hedman, M. M. 2016. Are There Moonlets Near the Uranian α and β Rings? The Astronomical Journal, 152, 211, doi: 10.3847/0004-6256/152/6/211

Chancia, R. O., Hedman, M. M., Cowley, S. W. H., Provan, G., & Ye, S. Y. 2019. Seasonal structures in Saturn's dusty Roche Division correspond to periodicities of the planet's magnetosphere. Icarus, 330, 230, doi: 10.1016/j.icarus.2019.04.012

Chancia, R. O., Hedman, M. M., & French, R. G. 2017. Weighing Uranus' Moon Cressida with the η Ring. The Astronomical Journal, 154, 153, doi: 10.3847/1538-3881/aa880e

Charnoz, S., Salmon, J., & Crida, A. 2010. The recent formation of Saturn's moonlets from viscous spreading of the main rings. Nature, 465, 752, doi: 10.1038/nature09096

Charnoz, S., Crida, A., Castillo-Rogez, J. C., et al. 2011. Accretion of Saturn's mid-sized moons during the viscous spreading of young massive rings: Solving the paradox of silicate-poor rings versus silicate-rich moons. Icarus, 216, 535, doi: 10.1016/j.icarus.2011.09.017

Clarke, K. E., Andrews, D. J., Arridge, C. S., Coates, A. J., & Cowley, S. W. H. 2010. Magnetopause oscillations near the planetary period at Saturn: Occurrence, phase, and amplitude. Journal of Geophysical Research (Space Physics), 115, A08209, doi: 10.1029/2009JA014745

Colwell, J. E., Horn, L. J., Lane, A. L., et al. 1990. Voyager photopolarimeter observations of Uranian ring occultations. Icarus, 83, 102, doi: 10.1016/0019-1035(90)90009-X

Ćuk, M., Dones, L., & Nesvorný, D. 2016. Dynamical Evidence for a Late Formation of Saturn's Moons. The Astrophysical Journal, 820, 97, doi: 10.3847/0004-637X/820/2/97

Cuzzi, J. N., & Scargle, J. D. 1985. Wavy edges suggest moonlet in Encke's gap. The Astrophysical Journal, 292, 276, doi: 10.1086/163158

de Kleer, K., de Pater, I., Ádámkovics, M., & Hammel, H. 2013. Near-infrared spectra of the uranian ring system. Icarus, 226, 1038, doi: 10.1016/j.icarus.2013.07.016

de Pater, I., Gibbard, S. G., & Hammel, H. B. 2006a. Evolution of the dusty rings of Uranus. Icarus, 180, 186, doi: 10.1016/j.icarus.2005.08.011

de Pater, I., Hammel, H. B., Gibbard, S. G., & Showalter, M. R. 2006b. New Dust Belts of Uranus: One Ring, Two Ring, Red Ring, Blue Ring. Science, 312, 92, doi: 10.1126/science.1125110

de Pater, I., Hammel, H. B., Showalter, M. R., & van Dam, M. A. 2007. The Dark Side of the Rings of Uranus. Science, 317, 1888, doi: 10.1126/science.1148103

de Pater, I., Dunn, D. E., Stam, D. M., et al. 2013. Keck and VLT AO observations and models of the uranian rings during the 2007 ring plane crossings. Icarus, 226, 1399, doi: 10.1016/j.icarus.2013.08.001

Dermott, S. F., Gold, T., & Sinclair, A. T. 1979. The rings of Uranus - Nature and origin. The Astronomical Journal, 84, 1225, doi: 10.1086/112533

Desch, M. D., & Kaiser, M. L. 1981. Voyager measurement of the rotation period of Saturn's magnetic field. Geophysical Research Letters, 8, 253, doi: 10.1029/GL008i003p00253

Dougherty, M. K., Cao, H., Khurana, K. K., et al. 2018. Saturn's magnetic field revealed by the Cassini Grand Finale. Science, 362, aat5434, doi: 10.1126/science.aat5434

Dumas, C., Smith, B. A., & Terrile, R. J. 2003. Hubble Space Telescope NICMOS Multiband Photometry of Proteus and Puck. The Astronomical Journal, 126, 1080, doi: 10.1086/375909

Duncan, M. J., & Lissauer, J. J. 1997. Orbital Stability of the Uranian Satellite System. Icarus, 125, 1, doi: 10.1006/icar.1996.5568

El Moutamid, M., Hedman, M., & Nicholson, P. D. 2018, in AAS/Division for Planetary Sciences Meeting Abstracts, 214.16

El Moutamid, M., Nicholson, P. D., French, R. G., et al. 2016. How Janus' orbital swap affects the edge of Saturn's A ring? Icarus, 279, 125, doi: 10.1016/j.icarus.2015.10.025

Elliot, J. L. 1979. Stellar occultation studies of the solar system. Annual Review of Astronomy & Astrophysics, 17, 445, doi: 10.1146/annurev.aa.17.090179.002305

Elliot, J. L., Dunham, E., & Mink, D. 1977a. The rings of Uranus. Nature, 267, 328, doi: 10.1038/267328a0

Elliot, J. L., Dunham, E., Wasserman, L. H., & Millis, R. L. 1978. The radii of Uranian rings alpha, beta, gamma, delta, epsilon, eta, 4, 5, and 6 from their occultations of SAO 158687. The Astronomical Journal, 83, 980, doi: 10.1086/112280

Elliot, J. L., French, R. G., Frogel, J. A., et al. 1981a. Orbits of nine Uranian rings. The Astronomical Journal, 86, 444, doi: 10.1086/112904

Elliot, J. L., French, R. G., Meech, K. J., & Elias, J. H. 1984. Structure of the Uranian rings. I - Square-well model and particle-size constraints. The Astronomical Journal, 89, 1587, doi: 10.1086/113662

Elliot, J. L., Frogel, J. A., Elias, J. H., et al. 1981b. The 20 March 1980 occultation by the Uranian rings. The Astronomical Journal, 86, 127, doi: 10.1086/112864

Elliot, J. L., Glass, I. S., French, R. G., & Kangas, J. A. 1987. The occultation of KME 17 by Uranus and its rings. Icarus, 71, 91, doi: 10.1016/0019-1035(87)90165-5

Elliot, J. L., & Nicholson, P. D. 1984, in IAU Colloq. 75: Planetary Rings, ed. R. Greenberg & A. Brahic, 25–72

Elliot, J. L., Dunham, E., Mink, D., et al. 1977b. Occultation of SAO 158687 by Uranian Satellite Belt. IAU Circulars, 3051

Elliot, J. L., Elias, J. H., French, R. G., et al. 1983. The rings of Uranus - Occultation profiles from three observatories. Icarus, 56, 202, doi: 10.1016/0019-1035(83)90033-7

Espinosa, S. A., & Dougherty, M. K. 2000. Periodic perturbations in Saturn's magnetic field. Geophysical Research Letters, 27, 2785, doi: 10.1029/2000GL000048

Farrell, W. M., Wahlund, J.-E., Morooka, M., et al. 2012. The electromagnetic pickup of submicron-sized dust above Enceladus's northern hemisphere. Icarus, 219, 498, doi: 10.1016/j.icarus.2012.02.033

Fischer, G., Gurnett, D. A., Kurth, W. S., Ye, S.-Y., & Groene, J. B. 2015. Saturn kilometric radiation periodicity after equinox. Icarus, 254, 72, doi: 10.1016/j.icarus.2015.03.014

French, R. G., Dawson, R. I., & Showalter, M. R. 2015. Resonances, Chaos, and Short-term Interactions Among the Inner Uranian Satellites. The Astronomical Journal, 149, 142, doi: 10.1088/0004-6256/149/4/142

French, R. G., Elliot, J. L., & Allen, D. A. 1982. Inclinations of the Uranian rings. Nature, 298, 827, doi: 10.1038/298827a0

French, R. G., Elliot, J. L., & Levine, S. E. 1986a. Structure of the Uranian rings. II - Ring orbits and widths. Icarus, 67, 134, doi: 10.1016/0019-1035(86)90181-8

French, R. G., Flury, S., Fong, J., et al. 2019a, in AAS/Division of Dynamical Astronomy Meeting, Vol. 51, AAS/Division of Dynamical Astronomy Meeting, P7

French, R. G., Kangas, J. A., & Elliot, J. L. 1986b. What perturbs the gamma and delta rings of Uranus? Science, 231, 480, doi: 10.1126/science.231.4737.480

French, R. G., McGhee-French, C. A., Nicholson, P. D., & Hedman, M. M. 2019b. Kronoseismology III: Waves in Saturn's inner C ring. Icarus, 319, 599, doi: 10.1016/j.icarus.2018.10.013

French, R. G., & Nicholson, P. D. 1995, in Bulletin of the American Astronomical Society, Vol. 27, American Astronomical Society Meeting Abstracts #186, 857

French, R. G., Nicholson, P. D., Hedman, M. M., et al. 2016a. Deciphering the embedded wave in Saturn's Maxwell ringlet. Icarus, 279, 62, doi: 10.1016/j.icarus.2015.08.020

French, R. G., Nicholson, P. D., McGhee-French, C. A., et al. 2016b. Noncircular features in Saturn's rings III: The Cassini Division. Icarus, 274, 131, doi: 10.1016/j.icarus.2016.03.017

French, R. G., Nicholson, P. D., Porco, C. C., & Marouf, E. A. 1991, Dynamics and structure of the Uranian rings, ed. J. T. Bergstralh, E. D. Miner, & M. S. Matthews, 327–409

French, R. G., Elliot, J. L., French, L. M., et al. 1988. Uranian ring orbits from earth-based and Voyager occultation observations. Icarus, 73, 349, doi: 10.1016/0019-1035(88)90104-2

French, R. G., Roques, F., Nicholson, P. D., et al. 1996. Earth-Based Detection of Uranus' Lambda Ring. Icarus, 119, 269, doi: 10.1006/icar.1996.0020

French, R. G., McGhee-French, C. A., Lonergan, K., et al. 2017. Noncircular features in Saturn's rings IV: Absolute radius scale and Saturn's pole direction. Icarus, 290, 14, doi: 10.1016/j.icarus.2017.02.007

French, R. S., & Showalter, M. R. 2012. Cupid is doomed: An analysis of the stability of the inner uranian satellites. Icarus, 220, 911, doi: 10.1016/j.icarus.2012.06.031

Galopeau, P. H. M., & Lecacheux, A. 2000. Variations of Saturn's radio rotation period measured at kilometer wavelengths. Journal of Geophysical Research, 105, 13089, doi: 10.1029/1999JA005089

García-Melendo, E., Pérez-Hoyos, S., Sánchez-Lavega, A., & Hueso, R. 2011. Saturn's zonal wind profile in 2004-2009 from Cassini ISS images and its long-term variability. Icarus, 215, 62, doi: 10.1016/j.icarus.2011.07.005

Gehrels, T., Baker, L. R., Beshore, E., et al. 1980. Imaging photopolarimeter on Pioneer Saturn. Science, 207, 434, doi: 10.1126/science.207.4429.434

Goldreich, P., & Lynden-Bell, D. 1965. II. Spiral arms as sheared gravitational instabilities. Monthly Notices of the Royal Astronomical Society, 130, 125, doi: 10.1093/mnras/130.2.125

Goldreich, P., & Porco, C. C. 1987. Shepherding of the Uranian Rings. II. Dynamics. The Astronomical Journal, 93, 730, doi: 10.1086/114355

Goldreich, P., & Tremaine, S. 1978a. The excitation and evolution of density waves. The Astrophysical Journal, 222, 850, doi: 10.1086/156203

—. 1979. Towards a theory for the Uranian rings. Nature, 277, 97, doi: 10.1038/277097a0

—. 1980. Disk-satellite interactions. The Astrophysical Journal, 241, 425, doi: 10.1086/158356

—. 1982. The dynamics of planetary rings. Annual Review of Astronomy & Astrophysics, 20, 249, doi: 10.1146/annurev.aa.20.090182.001341

Goldreich, P., & Tremaine, S. D. 1978b. The formation of the Cassini division in Saturn's rings. Icarus, 34, 240, doi: 10.1016/0019-1035(78)90165-3

Graps, A. L., Showalter, M. R., Lissauer, J. J., & Kary, D. M. 1995. Optical Depths Profiles and Streamlines of the Uranian (epsilon) Ring. The Astronomical Journal, 109, 2262, doi: 10.1086/117451

Grätz, F., Seiß, M., & Spahn, F. 2018. Formation of Moon-induced Gaps in Dense Planetary Rings: Application to the Rings of Saturn. The Astrophysical Journal, 862, 157, doi: 10.3847/1538-4357/aace00

Gresh, D. L., Marouf, E. A., Tyler, G. L., Rosen, P. A., & Simpson, R. A. 1989. Voyager radio occultation by Uranus' rings. I - Observational results. Icarus, 78, 131, doi: 10.1016/0019-1035(89)90074-2

Grundy, W. M., Young, L. A., Spencer, J. R., et al. 2006. Distributions of H $_2$O and CO $_2$ ices on Ariel, Umbriel, Titania, and Oberon from IRTF/SpeX observations. Icarus, 184, 543, doi: 10.1016/j.icarus.2006.04.016

Gurnett, D. A., Groene, J. B., Averkamp, T. F., et al. 2011a. An SLS4 Longitude System Based on a Tracking Filter Analysis of the Rotational Modulation of Saturn Kilometric Radiation. Planetary, Solar and Heliospheric Radio Emissions (PRE VII), 51

Gurnett, D. A., Groene, J. B., Persoon, A. M., et al. 2010. The reversal of the rotational modulation rates of the north and south components of Saturn kilometric radiation near equinox. Geophysical Research Letters, 37, L24101, doi: 10.1029/2010GL045796

Gurnett, D. A., Lecacheux, A., Kurth, W. S., et al. 2009a. Discovery of a north-south asymmetry in Saturn's radio rotation period. Geophysical Research Letters, 36, L16102, doi: 10.1029/2009GL039621

Gurnett, D. A., Persoon, A. M., Groene, J. B., et al. 2009b. A north-south difference in the rotation rate of auroral hiss at Saturn: Comparison to Saturn's kilometric radio emission. Geophysical Research Letters, 36, L21108, doi: 10.1029/2009GL040774

—. 2011b. The rotation of the plasmapause-like boundary at high latitudes in Saturn's magnetosphere and its relation to the eccentric rotation of the northern and southern auroral ovals. Geophysical Research Letters, 38, L21203, doi: 10.1029/2011GL049547

Gurnett, D. A., Persoon, A. M., Kurth, W. S., et al. 2007. The Variable Rotation Period of the Inner Region of Saturn's Plasma Disk. Science, 316, 442, doi: 10.1126/science.1138562

Hamilton, D. P. 1994. A comparison of Lorentz, planetary gravitational, and satellite gravitational resonances. Icarus, 109, 221, doi: 10.1006/icar.1994.1089

Hamilton, D. P., & Krivov, A. V. 1996. Circumplanetary Dust Dynamics: Effects of Solar Gravity, Radiation Pressure, Planetary Oblateness, and Electromagnetism. Icarus, 123, 503, doi: 10.1006/icar.1996.0175

Harrington, R. S., & Seidelmann, P. K. 1981. The dynamics of the Saturnian satellites 1980S1 and 1980S3. Icarus, 47, 97, doi: 10.1016/0019-1035(81)90094-4

Hedman, M. M. 2018, An Introduction to Planetary Ring Dynamics, ed. M. S. Tiscareno & C. D. Murray, Cambridge Planetary Science (Cambridge University Press), 30–48

Hedman, M. M., Burns, J. A., Hamilton, D. P., & Showalter, M. R. 2012. The three-dimensional structure of Saturn's E ring. Icarus, 217, 322, doi: 10.1016/j.icarus.2011.11.006

—. 2013. Of horseshoes and heliotropes: Dynamics of dust in the Encke Gap. Icarus, 223, 252, doi: 10.1016/j.icarus.2012.11.036

Hedman, M. M., Burns, J. A., Tiscareno, M. S., & Porco, C. C. 2009a. Organizing some very tenuous things: Resonant structures in Saturn's faint rings. Icarus, 202, 260, doi: 10.1016/j.icarus.2009.02.016

Hedman, M. M., Burt, J. A., Burns, J. A., & Showalter, M. R. 2014. Non-circular features in Saturn's D ring: D68. Icarus, 233, 147, doi: 10.1016/j.icarus.2014.01.022

Hedman, M. M., Burt, J. A., Burns, J. A., & Tiscareno, M. S. 2010a. The shape and dynamics of a heliotropic dusty ringlet in the Cassini Division. Icarus, 210, 284, doi: 10.1016/j.icarus.2010.06.017

Hedman, M. M., & Carter, B. J. 2017. A curious ringlet that shares Prometheus' orbit but precesses like the F ring. Icarus, 281, 322, doi: 10.1016/j.icarus.2016.08.024

Hedman, M. M., Murray, C. D., Cooper, N. J., et al. 2009b. Three tenuous rings/arcs for three tiny moons. Icarus, 199, 378, doi: 10.1016/j.icarus.2008.11.001

Hedman, M. M., & Nicholson, P. D. 2013. Kronoseismology: Using Density Waves in Saturn's C Ring to Probe the Planet's Interior. The Astronomical Journal, 146, 12, doi: 10.1088/0004-6256/146/1/12

—. 2014. More Kronoseismology with Saturn's rings. Monthly Notices of the Royal Astronomical Society, 444, 1369, doi: 10.1093/mnras/stu1503

—. 2019. Axisymmetric density waves in Saturn's rings. Monthly Notices of the Royal Astronomical Society, 485, 13, doi: 10.1093/mnras/stz301

Hedman, M. M., Nicholson, P. D., & French, R. G. 2019. Kronoseismology. IV. Six Previously Unidentified Waves in Saturn's Middle C Ring. The Astronomical Journal, 157, 18, doi: 10.3847/1538-3881/aaf0a6

Hedman, M. M., Burns, J. A., Showalter, M. R., et al. 2007. Saturn's dynamic D ring. Icarus, 188, 89, doi: 10.1016/j.icarus.2006.11.017

Hedman, M. M., Nicholson, P. D., Baines, K. H., et al. 2010b. The Architecture of the Cassini Division. The Astronomical Journal, 139, 228, doi: 10.1088/0004-6256/139/1/228

Hesselbrock, A. J., & Minton, D. A. 2019. Three Dynamical Evolution Regimes for Coupled Ring-satellite Systems and Implications for the Formation of the Uranian Satellite Miranda. The Astronomical Journal, 157, 30, doi: 10.3847/1538-3881/aaf23a

Holberg, J. B., Nicholson, P. D., French, R. G., & Elliot, J. L. 1987. Stellar occultation probes of the Uranian rings at 0.1 and 2.2 microns - A comparison of Voyager UVS and earth-based results. The Astronomical Journal, 94, 178, doi: 10.1086/114462

Horányi, M., & Juhász, A. 2010. Plasma conditions and the structure of the Jovian ring. Journal of Geophysical Research (Space Physics), 115, A09202, doi: 10.1029/2010JA015472

Horn, L. J., Showalter, M. R., & Russell, C. T. 1996. Detection and Behavior of Pan Wakes in Saturn's A Ring. Icarus, 124, 663, doi: 10.1006/icar.1996.0240

Hubbard, W. B., Brahic, A., Sicardy, B., et al. 1986. Occultation detection of a neptunian ring-like arc. Nature, 319, 636, doi: 10.1038/319636a0

Hunt, G. J., Cowley, S. W. H., Provan, G., et al. 2014. Field-aligned currents in Saturn's southern nightside magnetosphere: Subcorotation and planetary period oscillation components. Journal of Geophysical Research (Space Physics), 119, 9847, doi: 10.1002/2014JA020506

Hussmann, H., Sohl, F., & Spohn, T. 2006. Subsurface oceans and deep interiors of medium-sized outer planet satellites and large trans-neptunian objects. Icarus, 185, 258, doi: 10.1016/j.icarus.2006.06.005

Iess, L., Militzer, B., Kaspi, Y., et al. 2019. Measurement and implications of Saturn's gravity field and ring mass. Science, 364, aat2965, doi: 10.1126/science.aat2965

Jacobson, R. A. 1998. The Orbits of the Inner Uranian Satellites from Hubble Space Telescope and Voyager 2 Observations. The Astronomical Journal, 115, 1195, doi: 10.1086/300263

—. 2014. The Orbits of the Uranian Satellites and Rings, the Gravity Field of the Uranian System, and the Orientation of the Pole of Uranus. The Astronomical Journal, 148, 76, doi: 10.1088/0004-6256/148/5/76

Jacobson, R. A., Campbell, J. K., Taylor, A. H., & Synnott, S. P. 1992. The masses of Uranus and its major satellites from Voyager tracking data and earth-based Uranian satellite data. The Astronomical Journal, 103, 2068, doi: 10.1086/116211

Jacobson, R. A., Spitale, J., Porco, C. C., et al. 2008. Revised Orbits of Saturn's Small Inner Satellites. The Astronomical Journal, 135, 261, doi: 10.1088/0004-6256/135/1/261

Jacobson, R. A., Antreasian, P. G., Bordi, J. J., et al. 2006. The Gravity Field of the Saturnian System from Satellite Observations and Spacecraft Tracking Data. The Astronomical Journal, 132, 2520, doi: 10.1086/508812

Jia, X., Kivelson, M. G., & Gombosi, T. I. 2012. Driving Saturn's magnetospheric periodicities from the upper atmosphere/ionosphere. Journal of Geophysical Research (Space Physics), 117, A04215, doi: 10.1029/2011JA017367

Julian, W. H., & Toomre, A. 1966. Non-Axisymmetric Responses of Differentially Rotating Disks of Stars. The Astrophysical Journal, 146, 810, doi: 10.1086/148957

Karkoschka, E. 1997. Rings and Satellites of Uranus: Colorful and Not So Dark. Icarus, 125, 348, doi: 10.1006/icar.1996.5631

—. 2001a. Comprehensive Photometry of the Rings and 16 Satellites of Uranus with the Hubble Space Telescope. Icarus, 151, 51, doi: 10.1006/icar.2001.6596

—. 2001b. Voyager's Eleventh Discovery of a Satellite of Uranus and Photometry and the First Size Measurements of Nine Satellites. Icarus, 151, 69, doi: 10.1006/icar.2001.6597

Klemola, A. R., & Marsden, B. G. 1977. Predicted occultations by the rings of Uranus, 1977-1980. The Astronomical Journal, 82, 849, doi: 10.1086/112137

Klemola, A. R., & Mink, D. J. 1991. Occultations by Uranus and Neptune - 1991-1999. The Astronomical Journal, 102, 389, doi: 10.1086/115882

Klemola, A. R., Mink, D. J., & Elliot, J. L. 1981. Predicted occultations by Uranus - 1981-1984. The Astronomical Journal, 86, 138, doi: 10.1086/112866

Kollmann, P., Roussos, E., Kotova, A., et al. 2018. Saturn's Innermost Radiation Belt Throughout and Inward of the D-Ring. Geophysical Research Letters, 45, 10,912, doi: 10.1029/2018GL077954

Krupp, N., Roussos, E., Kollmann, P., et al. 2018. Energetic Neutral and Charged Particle Measurements in the Inner Saturnian Magnetosphere During the Grand Finale Orbits of Cassini 2016/2017. Geophysical Research Letters, 45, 10,847, doi: 10.1029/2018GL078096

Kumar, K., de Pater, I., & Showalter, M. R. 2015. Mab's orbital motion explained. Icarus, 254, 102, doi: 10.1016/j.icarus.2015.03.002

Kurth, W. S., Averkamp, T. F., Gurnett, D. A., Groene, J. B., & Lecacheux, A. 2008. An update to a Saturnian longitude system based on kilometric radio emissions. Journal of Geophysical Research (Space Physics), 113, A05222, doi: 10.1029/2007JA012861

Lamy, L. 2011. Variability of southern and northern periodicities of Saturn Kilometric Radiation. Planetary, Solar and Heliospheric Radio Emissions (PRE VII), 38. https://arxiv.org/abs/1102.3099

Lamy, L. 2017, in Planetary Radio Emissions VIII, edited by G. Fischer, G. Mann, M. Panchenko, and P. Zarka, Austrian Academy of Sciences Press, Vienna, p.171-190, 2017, 171–190

Lamy, L., Cecconi, B., Zarka, P., et al. 2011. Emission and propagation of Saturn kilometric radiation: Magnetoionic modes, beaming pattern, and polarization state. Journal of Geophysical Research (Space Physics), 116, A04212, doi: 10.1029/2010JA016195

Lamy, L., Prangé, R., Pryor, W., et al. 2013. Multispectral simultaneous diagnosis of Saturn's aurorae throughout a planetary rotation. Journal of Geophysical Research (Space Physics), 118, 4817, doi: 10.1002/jgra.50404

Lane, A. L., West, R. A., Nelson, R. M., et al. 1986. Photometry from Voyager 2 - Initial results from the Uranian atmosphere, satellites, and rings. Science, 233, 65, doi: 10.1126/science.233.4759.65

Lewis, M., Stewart, G., Leezer, J., & West, A. 2011. Negative diffusion in planetary rings with a nearby moon. Icarus, 213, 201, doi: 10.1016/j.icarus.2010.11.022

Lin, C. C., & Shu, F. H. 1964. On the Spiral Structure of Disk Galaxies. The Astrophysical Journal, 140, 646, doi: 10.1086/147955

Lissauer, J. J. 1995. Urey prize lecture: On the diversity of plausible planetary systems. Icarus, 114, 217, doi: 10.1006/icar.1995.1057

Lissauer, J. J., & Cuzzi, J. N. 1982. Resonances in Saturn's rings. The Astronomical Journal, 87, 1051, doi: 10.1086/113189

Mankovich, C., Marley, M. S., Fortney, J. J., & Movshovitz, N. 2019. Cassini Ring Seismology as a Probe of Saturn's Interior. I. Rigid Rotation. The Astrophysical Journal, 871, 1, doi: 10.3847/1538-4357/aaf798

Markwardt, C. B. 2009, in Astronomical Society of the Pacific Conference Series, Vol. 411, Astronomical Data Analysis Software and Systems XVIII, ed. D. A. Bohlender, D. Durand, & P. Dowler, 251

McGhee-French, C., French, R. G., & Gordon, M. 2019, in AAS/Division of Dynamical Astronomy Meeting, Vol. 51, AAS/Division of Dynamical Astronomy Meeting, P22

Millis, R. L., & Wasserman, L. H. 1978. The occultation of BD -15 deg 3969 by the rings of Uranus. The Astronomical Journal, 83, 993, doi: 10.1086/112281

Millis, R. L., Wasserman, L. H., & Birch, P. V. 1977. Detection of rings around Uranus. Nature, 267, 330, doi: 10.1038/267330a0

Mink, D. J., & Klemola, A. 1982. Possible occulations by satellites of Uranus and Neptune - 1983-1985. The Astronomical Journal, 87, 1881, doi: 10.1086/113278

—. 1985. Predicted occultations by Uranus, Neptune, and Pluto 1985-1990. The Astronomical Journal, 90, 1894, doi: 10.1086/113893

Mitchell, C. J., Horányi, M., Havnes, O., & Porco, C. C. 2006. Saturn's Spokes: Lost and Found. Science, 311, 1587, doi: 10.1126/science.1123783

Mitchell, C. J., Porco, C. C., Dones, H. L., & Spitale, J. N. 2013. The behavior of spokes in Saturn's B ring. Icarus, 225, 446, doi: 10.1016/j.icarus.2013.02.011

Murray, C. D., Beurle, K., Cooper, N. J., et al. 2008. The determination of the structure of Saturn's F ring by nearby moonlets. Nature, 453, 739, doi: 10.1038/nature06999

Murray, C. D., & Dermott, S. F. 1999, Solar system dynamics (New York: Cambridge University Press)

Murray, C. D., & Thompson, R. P. 1988. The dust rings of Uranus - A picture is worth a million words. Vistas in Astronomy, 32, 225, doi: 10.1016/0083-6656(88)90411-4

—. 1990. Orbits of shepherd satellites deduced from the structure of the rings of Uranus. Nature, 348, 499, doi: 10.1038/348499a0

Nichols, J. D., Cecconi, B., Clarke, J. T., et al. 2010. Variation of Saturn's UV aurora with SKR phase. Geophysical Research Letters, 37, L15102, doi: 10.1029/2010GL044057

Nicholson, P. D., French, R. G., Hedman, M. M., Marouf, E. A., & Colwell, J. E. 2014a. Noncircular features in Saturn's rings I: The edge of the B ring. Icarus, 227, 152, doi: 10.1016/j.icarus.2013.09.002

Nicholson, P. D., French, R. G., McGhee-French, C. A., et al. 2014b. Noncircular features in Saturn's rings II: The C ring. Icarus, 241, 373, doi: 10.1016/j.icarus.2014.06.024

Nicholson, P. D., Matthews, K., & Goldreich, P. 1981. The Uranus occultation of 10 June 1979. I - The rings. The Astronomical Journal, 86, 596, doi: 10.1086/112921

Nicholson, P. D., McLeod, B. A., Gilmore, G., Buie, M. W., & Matthews, K. 1988. Near-infrared stellar-occultation predictions for Uranus and Neptune - 1987-1990. The Astronomical Journal, 95, 562, doi: 10.1086/114656

Nicholson, P. D., Persson, S. E., Matthews, K., Goldreich, P., & Neugebauer, G. 1978. The rings of Uranus - Results of the 10 April 1978 occultation. The Astronomical Journal, 83, 1240, doi: 10.1086/112318

Nicholson, P. D., & Porco, C. C. 1988. A new constraint on Saturn's zonal gravity harmonics from Voyager observations of an eccentric ringlet. Journal of Geophysical Research, 93, 10209, doi: 10.1029/JB093iB09p10209

Ockert-Bell, M. E., Burns, J. A., Daubar, I. J., et al. 1999. The Structure of Jupiter's Ring System as Revealed by the Galileo Imaging Experiment. Icarus, 138, 188, doi: 10.1006/icar.1998.6072

Ortiz, J. L., Santos-Sanz, P., Sicardy, B., et al. 2017. The size, shape, density and ring of the dwarf planet Haumea from a stellar occultation. Nature, 550, 219, doi: 10.1038/nature24051

Owen, W. M., & Synnott, S. P. 1987. Orbits of the ten small satellites of Uranus. The Astronomical Journal, 93, 1268, doi: 10.1086/114409

Papaloizou, J. C. B., & Terquem, C. 2006. Planet formation and migration. Reports on Progress in Physics, 69, 119, doi: 10.1088/0034-4885/69/1/R03

Pascu, D., Rohde, J. R., Seidelmann, P. K., et al. 1998. Hubble Space Telescope Astrometric Observations and Orbital Mean Motion Corrections for the Inner Uranian Satellites. The Astronomical Journal, 115, 1190, doi: 10.1086/300245

Perry, M. E., Waite, J. H., Mitchell, D. G., et al. 2018. Material Flux From the Rings of Saturn Into Its Atmosphere. Geophysical Research Letters, 45, 10,093, doi: 10.1029/2018GL078575

Porco, C., Danielson, G. E., Goldreich, P., Holberg, J. B., & Lane, A. L. 1984. Saturn's nonaxisymmetric ring edges at 1.95 R(s) and 2.27 R(s). Icarus, 60, 17, doi: 10.1016/0019-1035(84)90135-0

Porco, C. A., & Danielson, G. E. 1982. The periodic variation of spokes in Saturn's rings. The Astronomical Journal, 87, 826, doi: 10.1086/113162

Porco, C. C. 2004. Satellites and Rings of Saturn. IAU Circulars, 8432

Porco, C. C., & Cassini Imaging Science Team. 2004. S/2004 S 3, S/2004 S 4, and R/2004 S 1. IAU Circulars, 8401

Porco, C. C., & Goldreich, P. 1987. Shepherding of the Uranian rings. I - Kinematics. II - Dynamics. The Astronomical Journal, 93, 724, doi: 10.1086/114354

Porco, C. C., & Nicholson, P. D. 1987. Eccentric features in Saturn's outer C ring. Icarus, 72, 437, doi: 10.1016/0019-1035(87)90185-0

Porco, C. C., West, R. A., Squyres, S., et al. 2004. Cassini Imaging Science: Instrument Characteristics And Anticipated Scientific Investigations At Saturn. Space Science Reviews, 115, 363, doi: 10.1007/s11214-004-1456-7

Porco, C. C., Baker, E., Barbara, J., et al. 2005. Cassini Imaging Science: Initial Results on Saturn's Rings and Small Satellites. Science, 307, 1226, doi: 10.1126/science.1108056

Provan, G., Cowley, S. W. H., Bradley, T. J., et al. 2018. Planetary Period Oscillations in Saturn's Magnetosphere: Cassini Magnetic Field Observations Over the Northern Summer Solstice Interval. Journal of Geophysical Research (Space Physics), 123, 3859, doi: 10.1029/2018JA025237

Provan, G., Cowley, S. W. H., Bunce, E. J., et al. 2019. Variability of Intra-D Ring Azimuthal Magnetic Field Profiles Observed on Cassini's Proximal Periapsis Passes. Journal of Geophysical Research (Space Physics), 124, 379, doi: 10.1029/2018JA026121

Provan, G., Cowley, S. W. H., Lamy, L., et al. 2016. Planetary period oscillations in Saturn's magnetosphere: Coalescence and reversal of northern and southern periods in late northern spring. Journal of Geophysical Research (Space Physics), 121, 9829, doi: 10.1002/2016JA023056

Provan, G., Cowley, S. W. H., Sandhu, J., Andrews, D. J., & Dougherty, M. K. 2013. Planetary period magnetic field oscillations in Saturn's magnetosphere: Postequinox abrupt nonmonotonic transitions to northern system dominance. Journal of Geophysical Research (Space Physics), 118, 3243, doi: 10.1002/jgra.50186

Provan, G., Lamy, L., Cowley, S. W. H., & Dougherty, M. K. 2014. Planetary period oscillations in Saturn's magnetosphere: Comparison of magnetic oscillations and SKR modulations in the postequinox interval. Journal of Geophysical Research (Space Physics), 119, 7380, doi: 10.1002/2014JA020011

Quillen, A. C., & French, R. S. 2014. Resonant chains and three-body resonances in the closely packed inner Uranian satellite system. Monthly Notices of the Royal Astronomical Society, 445, 3959, doi: 10.1093/mnras/stu2023

Ramer, K. M., Kivelson, M. G., Sergis, N., Khurana, K. K., & Jia, X. 2017. Spinning, breathing, and flapping: Periodicities in Saturn's middle magnetosphere. Journal of Geophysical Research (Space Physics), 122, 393, doi: 10.1002/2016JA023126

Roussos, E., Kollmann, P., Krupp, N., et al. 2018. A radiation belt of energetic protons located between Saturn and its rings. Science, 362, aat1962, doi: 10.1126/science.aat1962

Salo, H. 1995. Simulations of dense planetary rings. III. Self-gravitating identical particles. Icarus, 117, 287, doi: 10.1006/icar.1995.1157

Salo, H., Karjalainen, R., & French, R. G. 2004. Photometric modeling of Saturn's rings. II. Azimuthal asymmetry in reflected and transmitted light. Icarus, 170, 70, doi: 10.1016/j.icarus.2004.03.012

Schaffer, L., & Burns, J. A. 1992. Lorentz resonances and the vertical structure of dusty rings - Analytical and numerical results. Icarus, 96, 65, doi: 10.1016/0019-1035(92)90006-S

Seiß, M., Spahn, F., & Schmidt, J. 2010. Moonlet induced wakes in planetary rings: Analytical model including eccentric orbits of moon and ring particles. Icarus, 210, 298, doi: 10.1016/j.icarus.2010.06.013

Showalter, M. R. 1991. Visual detection of 1981S13, Saturn's eighteenth satellite, and its role in the Encke gap. Nature, 351, 709, doi: 10.1038/351709a0

—. 1996. Saturn's D Ring in the Voyager Images. Icarus, 124, 677, doi: 10.1006/icar.1996.0241

Showalter, M. R. 2011, in EPSC-DPS Joint Meeting 2011, 1224

Showalter, M. R., Burns, J. A., & Hamilton, D. P. 1998, in Bulletin of the American Astronomical Society, Vol. 30, AAS/Division for Planetary Sciences Meeting Abstracts #30, 1044

Showalter, M. R., Cuzzi, J. N., Marouf, E. A., & Esposito, L. W. 1986. Satellite 'wakes' and the orbit of the Encke Gap moonlet. Icarus, 66, 297, doi: 10.1016/0019-1035(86)90160-0

Showalter, M. R., de Pater, I., Lissauer, J. J., & French, R. S. 2019. The seventh inner moon of Neptune. Nature, 566, 350, doi: 10.1038/s41586-019-0909-9

Showalter, M. R., Hamilton, D. P., & Nicholson, P. D. 2006. A deep search for Martian dust rings and inner moons using the Hubble Space Telescope. Planetary and Space Science, 54, 844, doi: 10.1016/j.pss.2006.05.009

Showalter, M. R., & Lissauer, J. J. 2003. S/2003 U 1 and S/2003 U 2. IAU Circulars, 8209

—. 2006. The Second Ring-Moon System of Uranus: Discovery and Dynamics. Science, 311, 973, doi: 10.1126/science.1122882

Showalter, M. R., Cheng, A. F., Weaver, H. A., et al. 2007. Clump Detections and Limits on Moons in Jupiter's Ring System. Science, 318, 232, doi: 10.1126/science.1147647

Sicardy, B., Combes, M., Brahic, A., et al. 1982. The 15 August 1980 occultation by the Uranian system - Structure of the rings and temperature of the upper atmosphere. Icarus, 52, 454, doi: 10.1016/0019-1035(82)90006-9

Sicardy, B., Leiva, R., Renner, S., et al. 2019. Ring dynamics around non-axisymmetric bodies with application to Chariklo and Haumea. Nature Astronomy, 3, 146, doi: 10.1038/s41550-018-0616-8

Smith, B. A., Soderblom, L. A., Johnson, T. V., et al. 1979a. The Jupiter System Through the Eyes of Voyager 1. Science, 204, 951, doi: 10.1126/science.204.4396.951

Smith, B. A., Soderblom, L. A., Beebe, R., et al. 1979b. The Galilean Satellites and Jupiter: Voyager 2 Imaging Science Results. Science, 206, 927, doi: 10.1126/science.206.4421.927

Smith, B. A., Soderblom, L., Beebe, R. F., et al. 1981. Encounter with Saturn - Voyager 1 imaging science results. Science, 212, 163, doi: 10.1126/science.212.4491.163

Smith, B. A., Soderblom, L., Batson, R. M., et al. 1982. A New Look at the Saturn System: The Voyager 2 Images. Science, 215, 504, doi: 10.1126/science.215.4532.504

Smith, B. A., Soderblom, L. A., Beebe, R., et al. 1986. Voyager 2 in the Uranian system - Imaging science results. Science, 233, 43, doi: 10.1126/science.233.4759.43

Smith, B. A., Soderblom, L. A., Banfield, D., et al. 1989. Voyager 2 at Neptune: Imaging Science Results. Science, 246, 1422, doi: 10.1126/science.246.4936.1422

Southwood, D. J., & Cowley, S. W. H. 2014. The origin of Saturn's magnetic periodicities: Northern and southern current systems. Journal of Geophysical Research (Space Physics), 119, 1563, doi: 10.1002/2013JA019632

Spilker, L. 2019. Cassini-Huygens' exploration of the Saturn system: 13 years of discovery. Science, 364, 1046, doi: 10.1126/science.aat3760

Spitale, J. N., & Porco, C. C. 2009. Time Variability in the Outer Edge of Saturn's A-Ring Revealed by Cassini Imaging. The Astronomical Journal, 138, 1520, doi: 10.1088/0004-6256/138/5/1520

Stewart, G. R., Lin, D. N. C., & Bodenheimer, P. 1984, in IAU Colloq. 75: Planetary Rings, ed. R. Greenberg & A. Brahic, 447–512

Tajeddine, R., Nicholson, P. D., Longaretti, P.-Y., El Moutamid, M., & Burns, J. A. 2017. What Confines the Rings of Saturn? The Astrophysical Journal Supplement Series, 232, 28, doi: 10.3847/1538-4365/aa8c09

Tamayo, D., Triaud, A. H. M. J., Menou, K., & Rein, H. 2015. Dynamical Stability of Imaged Planetary Systems in Formation: Application to HL Tau. The Astrophysical Journal, 805, 100, doi: 10.1088/0004-637X/805/2/100

Taylor, G. E. 1973. An occultation by Uranus. Journal of the British Astronomical Association, 83, 352

Thomas, P., Weitz, C., & Veverka, J. 1989. Small satellites of Uranus - Disk-integrated photometry and estimated radii. Icarus, 81, 92, doi: 10.1016/0019-1035(89)90127-9

Thomas, P. C. 1988. Radii, shapes, and topography of the satellites of Uranus from limb coordinates. Icarus, 73, 427, doi: 10.1016/0019-1035(88)90054-1

Thomsen, M. F., Jackman, C. M., Cowley, S. W. H., et al. 2017. Evidence for periodic variations in the thickness of Saturn's nightside plasma sheet. Journal of Geophysical Research (Space Physics), 122, 280, doi: 10.1002/2016JA023368

Tiscareno, M. S., Burns, J. A., Hedman, M. M., & Porco, C. C. 2008. The Population of Propellers in Saturn's A Ring. The Astronomical Journal, 135, 1083, doi: 10.1088/0004-6256/135/3/1083

Tiscareno, M. S., Burns, J. A., Hedman, M. M., et al. 2006. 100-metre-diameter moonlets in Saturn's A ring from observations of 'propeller' structures. Nature, 440, 648, doi: 10.1038/nature04581

Tiscareno, M. S., Burns, J. A., Nicholson, P. D., Hedman, M. M., & Porco, C. C. 2007. Cassini imaging of Saturn's rings. II. A wavelet technique for analysis of density waves and other radial structure in the rings. Icarus, 189, 14, doi: 10.1016/j.icarus.2006.12.025

Tiscareno, M. S., & Harris, B. E. 2018. Mapping spiral waves and other radial features in Saturn's rings. Icarus, 312, 157, doi: 10.1016/j.icarus.2018.04.023

Tiscareno, M. S., Hedman, M. M., Burns, J. A., & Castillo-Rogez, J. 2013. Compositions and Origins of Outer Planet Systems: Insights from the Roche Critical Density. The Astrophysical Journal Letters, 765, L28, doi: 10.1088/2041-8205/765/2/L28

Tiscareno, M. S., Nicholson, P. D., Cuzzi, J. N., et al. 2019. Close-range remote sensing of Saturn's rings during Cassini's ring-grazing orbits and Grand Finale. Science, 364, aau1017, doi: 10.1126/science.aau1017

Toomre, A. 1964. On the gravitational stability of a disk of stars. The Astrophysical Journal, 139, 1217, doi: 10.1086/147861

Torrence, C., & Compo, G. P. 1998. A Practical Guide to Wavelet Analysis. Bulletin of the American Meteorological Society, 79, 61, doi: 10.1175/1520-0477(1998)079<0061:APGTWA>2.0.CO;2

Tyler, G. L., Eshleman, V. R., Hinson, D. P., et al. 1986. Voyager 2 radio science observations of the Uranian system Atmosphere, rings, and satellites. Science, 233, 79, doi: 10.1126/science.233.4759.79

Waite, J. H., Perryman, R. S., Perry, M. E., et al. 2018. Chemical interactions between Saturn's atmosphere and its rings. Science, 362, aat2382, doi: 10.1126/science.aat2382

Weiss, J. W., Porco, C. C., & Tiscareno, M. S. 2009. Ring Edge Waves and the Masses of Nearby Satellites. The Astronomical Journal, 138, 272, doi: 10.1088/0004-6256/138/1/272

West, R., Knowles, B., Birath, E., et al. 2010. In-flight calibration of the Cassini imaging science subsystem cameras. Planetary and Space Science, 58, 1475, doi: 10.1016/j.pss.2010.07.006

Ye, S.-Y., Fischer, G., Kurth, W. S., Menietti, J. D., & Gurnett, D. A. 2016. Rotational modulation of Saturn's radio emissions after equinox. Journal of Geophysical Research (Space Physics), 121, 11, doi: 10.1002/2016JA023281

—. 2018. An SLS5 Longitude System Based on the Rotational Modulation of Saturn Radio Emissions. Geophysical Research Letters, 45, 7297, doi: 10.1029/2018GL077976

Ye, S.-Y., Gurnett, D. A., Groene, J. B., Wang, Z., & Kurth, W. S. 2010. Dual periodicities in the rotational modulation of Saturn narrowband emissions. Journal of Geophysical Research (Space Physics), 115, A12258, doi: 10.1029/2010JA015780

Appendix A: Wavelength determination for RSS α ingress

The α ingress occultation scan does not contain a clear wake structure as in the other scans. As shown in Figure 2.3, this scan's wavelet transform contains no obvious locations of strong periodic structure consistent with a moonlet wake. However, the scan does contain a series of quasi-periodic dips and peaks in optical depth that are not cleanly isolated by the wavelet analysis. We determine the wake wavelength in this case by taking the average separation of these dips, marked in Figure A.1 and listed in Table A.1. An argument could be made to use an alternate set of dips or peaks for this calculation, but we have found that the various choices result in similar-enough wavelengths. Therefore, we believe that this estimation is a reasonable approach given the limited data set. We calculate a mean wavelength of 0.86 ± 0.09 km. The uncertainty we use here is the standard error of the mean and is much larger than the uncertainty determined for the other scans. This large uncertainty extends the possible range of moonlet radius to as high as 7 km; however, the moonlet would probably need to be on the smaller side of the range in Table 2.4 to have avoided detection in the images.

Table A.1: α ingress dip locations

Semimajor Axis (km)	Radius (km)
44,721.300	44,741.191
44,720.475	44,740.150
44,719.750	44,739.233
44,718.650	44,737.842
44,717.525	44,736.421
44,716.725	44,735.415
44,716.125	44,734.655

Locations of dips used for wavelength analysis in both semimajor axis and radius.

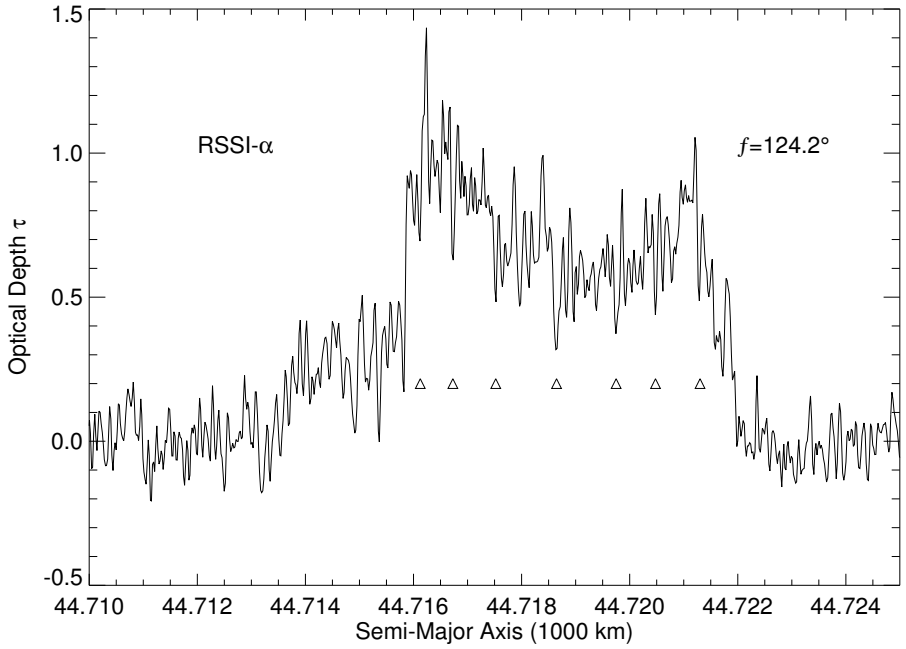

Figure A.1: The α ingress occultation in "semimajor axis space." We have marked the locations of the dips used in the wavelength analysis with triangles and have tabulated the exact semimajor axis of each dip in Table A.1.

Appendix B: β Persei PPS Occultation Analysis

Below is a parallel analysis of the β Persei (BP) PPS occultation observations. Table B.1 provides a summary of the BP PPS occultation data set used here, giving mid-times, inertial longitudes and radii, and true anomalies for the α and β rings at the time of the ingress and egress occultations. Figure B.1 contains the unbinned raw radial occultation scans of the α and β rings. The outer regions of both rings' ingress scans look to show some possible structure, but we find no dominant peaks in the Fourier spectrum of either ring. While past publications displaying binned versions of these stellar occultations (Colwell et al., 1990) look to possibly contain a periodic signature, upon further inspection of the unbinned raw data we found no strong evidence of periodic optical depth variations using the methods described above for the RSS data. We show the Fourier spectra for both ingress and egress of each ring in Figure B.2, along with the expected wavelengths resulting from the moonlet locations determined by our RSS analysis plotted as vertical lines and listed in Table B.2. None of these spectra show clear, unique maxima indicative of a strong periodic signal. In fact, for both the β ring scans the expected wavelengths are close to the occultation's sampling rate because the scan locations are significantly downstream from the last moonlet interaction. If our analysis of the RSS occultations is correct, it is unlikely that we can confirm detection of these small-wavelength optical depth variations in the β ring stellar occultations. We also note that in the egress scan the β ring is almost undetectable.

In the case of the α ring, the expected wavelengths are longer, and there are some weak peaks in the vicinity of the predictions based on the RSS data. However, these peaks are not far above the noise level and so cannot be regarded as strong evidence for periodic signals. However, we do observe a structure near the outer edge of the α ingress scan that arguably looks similar to the that of the RSS α ingress scan. Figure B.3 shows the α ingress scan in semimajor axis space accompanied by a sine wave with a wavelength we would expect the wake to have here, assuming a moonlet located as in Table 2.3. This wave appears to fit reasonably well here, but we do not claim this to be evidence that our α moonlet location is correct. Overall, we find that the analysis of the β Persei PPS occultation scans cannot confirm or deny the moonlet locations of the RSS analysis.

Table B.1: Geometry of β Persei Photopolarimeter Subsystem (PPS) occultations

Ring	Occ.	True Anom. (deg)	Mid-time (hr:min:s)	Mid-rad. (km)	Mid-long. (deg)
α	BPI	171.7	18:38:44.398	44,752.86	29.3
	BPE	249.7	19:33:16.498	44,731.10	107.4
β	BPI	59.7	18:37:21.368	45,651.83	27.9
	BPE	140.5	19:34:42.938	45,677.36	108.8

The appended labels of I and E stand for ingress and egress after BP for β Persei. The true anomaly of each ring at the time of their respective ring intercept mid-times and mid-radii is calculated from the inertial longitudes provided and the updated precession rates provided by R. G. French (see Table 2.2). Mid-times listed are the times of ring intercept measured in seconds after UTC 1986 January 24 00:00:00, when the light measured by PPS from β Persei (Algol) intercepted the mid-ring radius. The radial position of the rings shown in Figure B.1, created using the data provided on the PDS rings node, differs slightly from older publications.

Table B.2: Expected wavelengths for the PPS ring profiles based on the RSS analysis moonlet location.

Ring Scan	Wavelength (km)
BPI-α	$0.5^{+0.4}_{-0.2}$
BPE-α	$0.4^{+0.4}_{-0.1}$
BPI-β	$0.26^{+0.08}_{-0.06}$
BPE-β	$0.23^{+0.07}_{-0.05}$

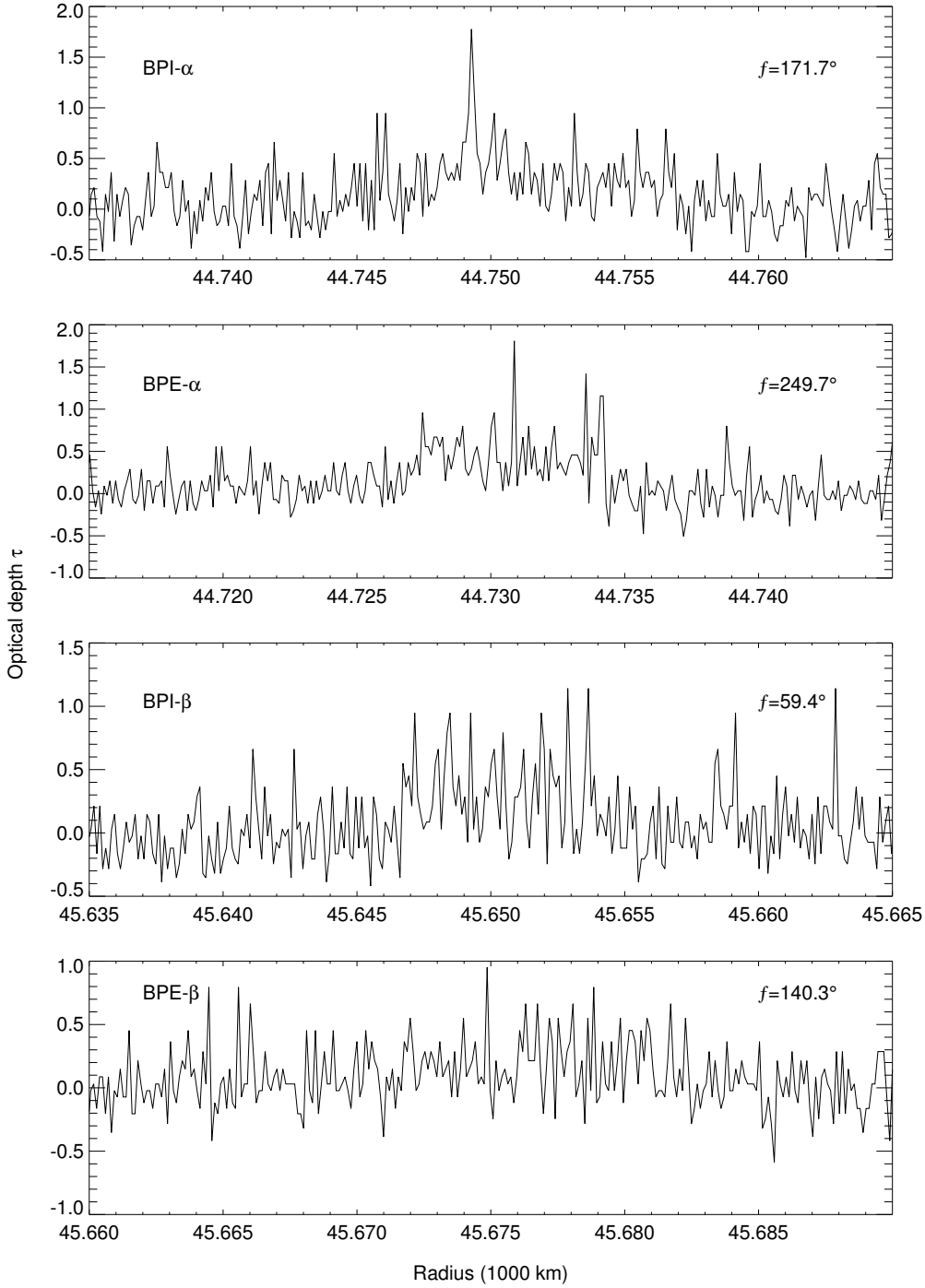

Figure B.1: β Persi PPS occultations of the α and β rings from the PDS. Note that like in Figure 2.1, these are the raw radial scans with varying scales in both optical depth and radius. The signal-to-noise ratio is much lower than the RSS data, so much so that it is very difficult to define edges in most cases. The β ring is hardly detectable at all in the egress scan.

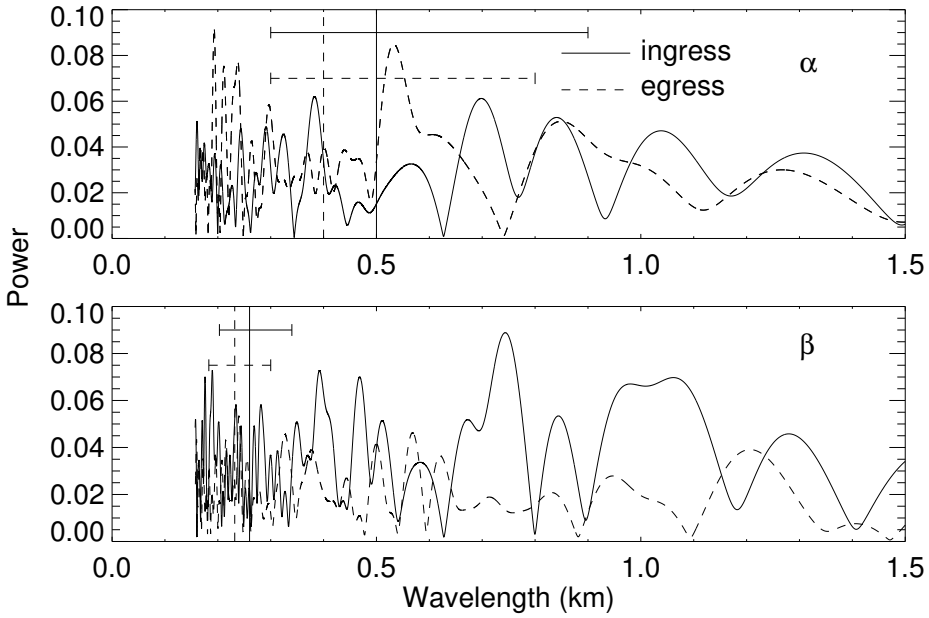

Figure B.2: Fourier transform of β Persei PPS occultation scans of the α and β rings. The ingress data are shown with solid lines and the egress with dashed lines. The vertical lines show the wavelengths, and uncertainties, that should be present if the moonlet is located as in the determination of the RSS analysis (see Table 2.3). No Fourier spectra of the PPS data have dominant wavelengths (except possibly the peak at ~ 0.53 in α egress, having no obvious correlation to structures in the ring profile) seen in the RSS analysis.

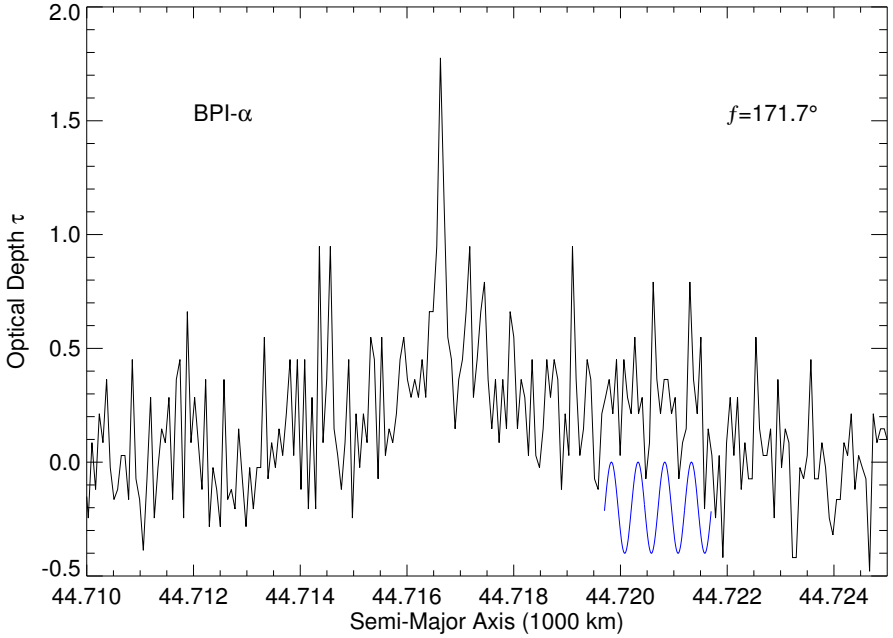

Figure B.3: β Persei PPS α ingress scan in semimajor axis space. The blue sine wave, with wavelength of 0.5 km, plotted below the data matches reasonably well with the quasi-periodic pattern near the outer edge of the ring. Given the low signal-to-noise ratio of the PPS data set, this is the best evidence we have for a connection between these observations, a proposed perturbing moonlet, and the RSS observations.

Appendix C: Uranian ring occultation observations

Included below are the occultation observation data we used in this analysis of the η ring. The precise numbers for the ring's position are derived from an analysis of the entire Uranian ring data set, including re-determined pole position (Pole right ascention = 77.3105814° and declination = 15.1697826°), standard gravitational parameter ($GM = 5.793956433 \times 10^6$ km^{3}s^{-2}), gravitational harmonics ($J_2 = 3.340656 \times 10^{-3}$ and $J_4 = -3.148536 \times 10^{-5}$), and time offsets. The numbers therefore can deviate slightly from previously published values. We list each observation ID, observing location, ring plane intercept time of the relevant electromagnetic wave observed, detected mid-radius of the η ring, $m = 3$ fit residuals, longitude of the observation, longitude of Cressida at this time, and reference to publications including the observation. Longitudes are measured in the prograde direction from the ascending node of Uranus' equator on the Earth's equator of the J2000 epoch. French et al. (1988) have included all observations from 1977-1986 in their most recent fit, but more recent observations are unpublished.

Table C.1: η ring occultation observation geometry

ID	Observing Location	Star Name Catalog ID	$t_{\text{ring intercept}}$ (UTC)	r (km)	$r - r_{\text{fit}}$ (km)	$\lambda(^\circ)$	Reference
1	Kuiper Airborne Obs.	U0 Hipparcos 71567	1977 MAR 10 17:48:26.95	47177.352	0.346	36.68	Elliot et al. (1977a)
2	Kuiper Airborne Observatory	U0 Hipparcos 71567	1977 MAR 10 19:20:03.28	47176.465	0.673	153.51	Elliot et al. (1977a)
3	Cerro Las Campanas Obs.	U5 UCAC2 25775788	1978 APR 10 03:00:16.19	47178.519	2.107	46.24	Nicholson et al. (1978)
4	Cerro Las Campanas Obs.	U5 UCAC2 25775788	1978 APR 10 03:50:16.64	47177.359	0.535	143.71	Nicholson et al. (1978)
5	Cerro Tololo Interamerican Obs.	U12 UCAC2 25096598	1980 AUG 15 22:20:37.70	47176.235	−0.087	22.05	Elliot et al. (1981a)
6	European Southern Obs. 1-m	U12 UCAC2 25096598	1980 AUG 15 19:24:18.97	47175.681	−0.476	171.95	Elliot et al. (1981a)
7	European Southern Obs. 1-m	U12 UCAC2 25096598	1980 AUG 15 22:20:36.26	47176.330	0.013	22.18	Elliot et al. (1981a)
8	Anglo-Australian Telescope	U13 Hipparcos 77434	1981 APR 26 16:45:45.26	47176.726	−0.341	26.90	French et al. (1982)
9	Anglo-Australian Telescope	U13 Hipparcos 77434	1981 APR 26 17:53:41.63	47176.877	−0.092	163.55	French et al. (1982)
10	European Southern Obs. 2-m	U14 Hipparcos 79085	1982 APR 22 00:27:11.11	47175.767	−0.184	164.12	French et al. (1986a)
11	Cerro Las Campanas Obs.	U14 Hipparcos 79085	1982 APR 21 23:07:45.20	47175.548	−0.314	24.83	French et al. (1986a)
12	Cerro Las Campanas Obs.	U14 Hipparcos 79085	1982 APR 22 00:27:11.32	47174.793	−1.158	164.09	French et al. (1986a)
13	Tenerife	U14 Hipparcos 79085	1982 APR 21 23:09:03.74	47176.060	−0.027	35.09	French et al. (1986a)
14	Cerro Tololo Interamerican Obs.	U14 Hipparcos 79085	1982 APR 21 23:07:38.90	47175.718	−0.143	24.70	French et al. (1986a)
15	Cerro Tololo Interamerican Obs.	U14 Hipparcos 79085	1982 APR 22 00:27:09.91	47175.595	−0.353	164.23	French et al. (1986a)
16	Mt. Stromlo	U15 UCAC2 23648038	1982 MAY 01 13:53:02.53	47176.249	0.275	27.01	French et al. (1986a)
17	Mt. Stromlo	U15 UCAC2 23648038	1982 MAY 01 15:01:45.77	47176.542	−0.119	162.76	French et al. (1986a)
18	Mt. Palomar	U16 UCAC2 23892052	1982 JUN 04 02:50:34.77	47175.991	−0.012	32.37	French et al. (1986a)
19	Mt. Palomar	U16 UCAC2 23892052	1982 JUN 04 03:50:47.86	47176.435	−0.464	156.73	French et al. (1986a)
20	South African Astronomical Obs.	U17 Hipparcos 80841	1983 MAR 24 22:05:13.10	47176.847	−0.238	35.29	French et al. (1986a)
21	Cerro Tololo Interamerican Obs.	U23 UCAC2 22735323	1985 MAY 04 02:28:59.92	47176.178	−0.003	318.94	French et al. (1988)
22	Cerro Tololo Interamerican Obs.	U23 UCAC2 22735323	1985 MAY 04 03:30:35.20	47176.885	0.774	229.93	French et al. (1988)
23	McDonald Obs.	U23 UCAC2 22735323	1985 MAY 04 03:37:42.72	47175.702	−0.133	221.66	French et al. (1988)
24	Cerro Tololo Interamerican Obs.	U25 UCAC2 22734194	1985 MAY 24 05:23:43.95	47176.565	0.747	316.13	French et al. (1988)
25	Cerro Tololo Interamerican Obs.	U25 UCAC2 22734194	1985 MAY 24 06:10:43.14	47176.151	0.340	233.85	French et al. (1988)
26	McDonald Obs.	U25 UCAC2 22734194	1985 MAY 24 05:22:06.85	47175.644	−0.154	326.24	French et al. (1988)
27	McDonald Obs.	U25 UCAC2 22734194	1985 MAY 24 06:17:47.01	47175.721	−0.124	223.28	French et al. (1988)
28	Mt. Palomar	U25 UCAC2 22734194	1985 MAY 24 05:23:00.51	47175.853	0.059	326.26	French et al. (1988)
29	Mt. Palomar	U25 UCAC2 22734194	1985 MAY 24 06:18:47.48	47175.497	−0.360	223.09	French et al. (1988)
30	IRTF	U28 UCAC2 22517254	1986 APR 26 10:58:06.57	47176.433	−0.282	333.24	Tyler et al. (1986)
31	IRTF	U28 UCAC2 22517254	1986 APR 26 12:34:39.87	47175.910	−0.632	215.97	Tyler et al. (1986)
32	IRTF	U1052 UCAC2 22296665	1988 MAY 12 10:56:55.69	47175.431	−0.563	293.09	Lane et al. (1986)
33	IRTF	U1052 UCAC2 22296665	1988 MAY 12 11:26:09.19	47176.094	−0.584	256.32	French et al. (1988)

ID	Observing Location	Star Name Catalog ID	$t_{\text{ring intercept}}$ (UTC)	r (km)	$r - r_{\text{fit}}$ (km)	$\lambda(^\circ)$	Reference
34	IRTF	U83 UCAC2 22564036	1991 JUN 25 10:10:59.40	47176.545	−0.530	326.15	French et al. (1988)
35	IRTF	U83 UCAC2 22564036	1991 JUN 25 10:59:59.96	47176.530	−0.581	224.37	Unpublished
36	IRTF	U84 UCAC2 22563790	1991 JUN 28 07:47:36.36	47176.741	−0.197	306.15	Unpublished
37	IRTF	U84 UCAC2 22563790	1991 JUN 28 08:19:53.10	47175.300	−0.507	243.98	Unpublished
38	Cerro Tololo Interamerican Obs.	U9539 UCAC2 23016546	1993 JUN 30 04:57:33.67	47176.082	0.063	351.62	Unpublished
39	Cerro Tololo Interamerican Obs.	U9539 UCAC2 23016546	1993 JUN 30 05:54:55.13	47177.216	0.256	199.09	Unpublished
40	South African Astronomical Obs.	U134 UCAC2 23509999	1995 SEP 09 15:29:49.47	47175.948	0.126	31.36	Unpublished
41	South African Astronomical Obs.	U134 UCAC2 23509999	1995 SEP 09 16:57:52.04	47177.201	0.292	161.04	Unpublished
42	IRTF	U137 UCAC3 141-413386	1996 MAR 16 11:59:43.68	47176.716	0.936	178.95	Unpublished
43	IRTF	U137 UCAC3 141-413386	1996 MAR 16 12:43:23.55	47177.408	0.372	13.13	Unpublished
44	Mt. Palomar	U138 UCAC2 24243463	1996 APR 10 09:27:44.07	47177.050	0.139	356.19	Unpublished
45	Mt. Palomar	U0201 UCAC2 27214859	2002 JUL 29 07:20:09.62	47177.709	0.829	74.55	Unpublished
46	Mt. Palomar	U0201 UCAC2 27214859	2002 JUL 29 07:29:17.80	47175.005	−0.807	117.00	Unpublished
47	Voyager 2 - RSS		1986 JAN 24 19:50:59.23	47176.817	0.080	343.08	French et al. (1991)
48	Voyager 2 - RSS		1986 JAN 24 22:44:28.11	47176.557	0.375	197.13	French et al. (1991)
49	Voyager 2 - PPS	β Per Hipparcos 14576	1986 JAN 24 19:36:54.98	47176.041	0.132	110.96	French et al. (1991)

The precise numbers for the ring's position are derived from an analysis of the entire Uranian ring data set, including re-determined pole position, GM, J_2, J_4, and time offsets. We used an epoch time, t_0, of UTC 1977 MAR 10 20:00:00.00 for all fits of this data set. The times, t, listed in this table refer to the exact time of the ray intercept in the ring plane for each occultation observation. The ring radii and longitudes are those observed at these times, where longitudes are measured in the prograde direction from the ascending node of Uranus' equator on the Earth's equator of the J2000 epoch. The residuals show separation of each observations' radii and the $m = 3$ model radii.

Appendix D: Faint ring response model

Here, we derive the model developed by Hedman et al. (2009a) with some slight corrections. We can approximate the dynamics of ring particles near a Lindblad resonance with a driven harmonic oscillator. Let $x = r - a$ represent a ring particle's radial excursions from semi-major axis a. The ring particle has a mean motion n close to that of the exact resonance n_r and its equation of motion is given by

$$\ddot{x} = -n^2 x - B\cos(n_r t) \tag{D.1}$$

where B is the strength of the driven oscillations. The solution to the equation of motion is

$$x = \frac{B}{n_r^2 - n^2}\cos(n_r t). \tag{D.2}$$

We can further approximate

$$n_r^2 - n^2 \approx \frac{3GM}{a_r^4}\delta a \tag{D.3}$$

where $n^2 = GM_S/a^3$, a_r is the resonant radius, and $\delta a = a - a_r$. Now, we can rewrite x as

$$x = r - a = \frac{\beta}{\delta a}\cos\phi' \tag{D.4}$$

where $\beta = B(3GM_S/a_r^4)^{-1}$ is the resonance strength and $\phi' = n_r t$ is related to the phase ϕ used in Equation 4.3 after approximating $\frac{m}{m-1} \approx \frac{n}{n_r}$. The distinction between ϕ and ϕ' is not noted by Hedman et al. (2009a), but is important to address. The phase parameter used previously, $\phi = m(\lambda - \Omega_p(t - t_0) - \delta_m)$ or more simply $\phi = m(\lambda - \lambda_s)$, varies differently than ϕ' with time if one considers the nature of our ring observations. In the ring image-movies we stare at one longitudinal region as time increases ($\dot{\lambda} = 0$), so ϕ is actually decreasing as time passes in our image sequence observations. Alternatively, one can clearly see that ϕ' should increase with time if $n_r > 0$. This will become important to consider when applying this simple model to the actual data and the direction the structure should be tilted, particularly for Figure 4.4.

After adding a damping term the equation of motion becomes:

$$\ddot{x} = -n^2 x - \frac{1}{\tau}\dot{x} - B\cos(n_r t) \tag{D.5}$$

where τ is the damping time of the radial excursions. The solution to the new equation of motion is

$$x = x_0\cos(n_r t - \phi_0') \tag{D.6}$$

where

$$x_0 = \frac{B}{(n_r^2 - n^2)\cos\phi_0' + (n_r/\tau)\sin\phi_0'} \tag{D.7}$$

and

$$\tan\phi_0' = \frac{n_r/\tau}{n_r^2 - n^2}. \tag{D.8}$$

The radii of particle streamlines can then be expressed as

$$r = a + x = a + x_0 \cos(\phi' - \phi'_0) = a + x_0(\cos\phi' \cos\phi'_0 - \sin\phi' \sin\phi'_0). \tag{D.9}$$

After finding the expressions for $\cos\phi'_0$ and $\sin\phi'_0$ from Equations D.7 and D.8 we can define the radius as

$$r = a + \frac{\beta}{(\delta a)^2 + L^2}(\delta a \cos\phi' - L \sin\phi') \tag{D.10}$$

where $L = a_r/(3n_r\tau)$ is the damping length. This streamline model results in a gradual shift of pericenter locations across the resonance, which is responsible for the canted brightness variations peaking at the exact resonance due to increased density of particles.

We assume that all particles are evenly distributed in semi-major axis and phase, and the phase space number density is constant $\rho(a, \phi) = \bar{\rho}$. Or, as a function of radius and phase

$$\rho(r, \phi) = \frac{\bar{\rho}}{dr/da} \tag{D.11}$$

where we assume the streamlines do not cross (i.e. dr/da never equals zero). In fact, the observed fractional variations in brightness are only a few percent at most, which is inconsistent with streamline crossing. Thus, the fractional variations in density are given by

$$\frac{\delta\rho(r, \phi)}{\rho} = \frac{\rho(r, \phi) - \bar{\rho}}{\bar{\rho}} \approx 1 - \frac{dr}{da}. \tag{D.12}$$

We can then differentiate Equation D.10 to get

$$\frac{dr}{da} = 1 - \frac{\beta}{[(\delta a)^2 + L^2]^2}\left[\left((\delta a)^2 - L^2\right)\cos\phi' - 2\delta a L \sin\phi'\right] \tag{D.13}$$

and, since $\delta r \approx \delta a$

$$\frac{\delta\rho(r, \phi')}{\rho} = \frac{\beta}{[(\delta r)^2 + L^2]^2}\left[\left((\delta r)^2 - L^2\right)\cos\phi' - 2\delta r L \sin\phi'\right] \tag{D.14}$$

where our amplitude of density variations is given by

$$A(r) = \frac{\beta}{(\delta r)^2 + L^2}. \tag{D.15}$$

The difference between Equation D.14 and Equation 4.5 is due to the subtle difference of ϕ' and ϕ.

Appendix E: Lorentz resonance strength

The perturbation equations needed to solve for the Lorentz resonance strength were derived by Hamilton (1994). We use the appropriate second-order expansion of the perturbation equations in their Table II. Specifically row three of the $g_{4,3}$ portion of Table II, because the resonant argument for the 3:4 OLR or effectively a 3:4 Lorentz resonance is $\varphi = -4\lambda + 3\lambda_s + \dot{\varpi}$. The approximate expansions are a function of the ratio of magnetic field coefficients $\frac{g_{4,3}}{g_{1,0}}$ appropriate for the 3:4 resonance:

$$\left\langle \frac{de}{dt} \right\rangle = 2\left(1 - \frac{n}{\Omega_S}\right) nL \frac{\sqrt{70}}{16} \frac{g_{4,3}}{g_{1,0}} \left(\frac{R_S}{a}\right)^3 \sin\varphi \tag{E.1}$$

and

$$\left\langle \frac{d\varpi}{dt} \right\rangle = -2\left(1 - \frac{n}{\Omega_S}\right) \frac{nL}{e} \frac{\sqrt{70}}{16} \frac{g_{4,3}}{g_{1,0}} \left(\frac{R_S}{a}\right)^3 \cos\varphi. \tag{E.2}$$

Here, Ω_S is the rotational frequency of Saturn's magnetic field, R_S is Saturn's equatorial radius, and L is the ratio of the Lorentz force and the planetary gravitational force:

$$L = \frac{q_g}{m_g} \frac{g_{1,0} R_S^3 \Omega_S}{G M_S}. \tag{E.3}$$

This force ratio is also dependent on Saturn's physical parameters, including mass M_S, the charge to mass ratio of the dust grains being perturbed $\frac{q_g}{m_g}$, and Saturn's dipole coefficient $g_{1,0}$. The stable solution requires $\left\langle \frac{de}{dt} \right\rangle = 0$, therefore, $\sin(\varphi) = 0$ and $\cos(\varphi) = \pm 1$.

To solve for the resonance strength we follow the logic of Hedman (2018). Taking the time derivative of Equation 4.1 we find:

$$\dot{\varphi} = m(n - n_s) - \left(n - \frac{d\varpi}{dt}\right) \tag{E.4}$$

and effectively

$$\dot{\varphi_0} = m(n - n_s) - (n - \dot{\varpi_0}) \tag{E.5}$$

where $\dot{\varpi_0}$ is the secular apsidal precession rate due to Saturn's finite oblateness. Consider the difference of $\dot{\varphi}$ and $\dot{\varphi_0}$:

$$\dot{\varphi} - \dot{\varphi_0} = m(n - n_s) - \left(n - \frac{d\varpi}{dt}\right) - m(n - n_s) + (n - \dot{\varpi_0}) = \frac{d\varpi}{dt} - \dot{\varpi_0}. \tag{E.6}$$

At the semi-major axis of a first-order resonance a_r for a particular integer m, φ is constant, and $\dot{\varphi} = 0$. Additionally, for ring particles orbiting near the resonance, or small $\delta a = a - a_r$, we can approximate $\dot{\varphi_0}$ by expanding in terms of $\frac{\delta a}{a_r}$:

$$\dot{\varphi_0} = -n \frac{\delta a}{a_r} \left[\frac{3}{2}(m-1) + \frac{21}{4} J_2 \left(\frac{R_S}{a_r}\right)^2\right] \approx -n \frac{\delta a}{a_r} \frac{3}{2}(m-1). \tag{E.7}$$

Equation E.2 should also contain a $\dot{\varpi_0}$ term to account for Saturn's finite oblateness, so we can rewrite

Equation E.6 as:

$$0 + n\frac{\delta a}{a_r}\frac{3}{2}(m-1) = -2\left(1 - \frac{n}{\Omega_S}\right)\frac{nL}{e}\frac{\sqrt{70}}{16}\frac{g_{4,3}}{g_{1,0}}\left(\frac{R_S}{a_r}\right)^3 \cos\varphi + \dot{\varpi}_0 - \dot{\varpi}_0. \tag{E.8}$$

We can now solve for a forced eccentricity $a_r e_f = \frac{\beta}{\delta a}$ similar to Equation 4.2:

$$a_r e_f = \frac{\sqrt{70}}{12}\left(\frac{n/\Omega_S - 1}{m-1}\right) L \frac{g_{4,3}}{g_{1,0}}\left(\frac{R_S}{a_r}\right)^3 \frac{a_r^2}{\delta a}, \tag{E.9}$$

and so in this case

$$\beta = \frac{\sqrt{70}}{12}\left(\frac{n/\Omega_S - 1}{m-1}\right) L \frac{g_{4,3}}{g_{1,0}}\left(\frac{R_S}{a_r}\right)^3 a_r^2 \tag{E.10}$$

is a measure of the resonance strength due to an electromagnetic perturbation. After substituting the right hand side of Equation E.3 for L:

$$\beta = \frac{\sqrt{70}}{12}\left(\frac{n/\Omega_S - 1}{m-1}\right) \frac{q_g}{m_g}\frac{R_S^3 \Omega_S a_r^2}{GM_S} g_{4,3}\left(\frac{R_S}{a_r}\right)^3. \tag{E.11}$$

A complete estimation of the resonance strength should also include contributions from, $h_{4,3}$ and other $g_{j,3}$ and $h_{j,3}$ coefficients. Assuming the charge to mass ratio for the ring particles in the Roche Division used above we find an upper limit of $g_{4,3}$ on the order of a few hundred to a few thousand nanotesla. This is far greater than those measured for the higher order axis-symmetric coefficients (Dougherty et al., 2018). However, measurements of the small magnetic field oscillations associated with the PPO perturbation field resemble our results. To compare with these measurements, we develop a new approximation for the electromagnetic perturbations on dusty ring regions very similar to the formulation shown here (See Section 4.3.3).

Appendix F: PPO Longitude System

We use the *Cassini* magnetometer PPO longitude system defined in Provan et al. (2018) and detailed in Figure F.1 to highlight our incorporation of ring observation longitudes. The PPO longitude of the northern or southern hemisphere $\Psi_{N/S} = \Phi_{N/S} - \phi$, where $\Phi_{N/S}$ are the PPO phases measured throughout the mission by the magnetometer team and ϕ is a longitude measured in the prograde direction from the sub-solar longitude. The PPO phases $\Phi_{N/S}$ are also measured from the sub-solar longitude in the prograde direction and define the zero point of the PPO longitude system $\Psi_{N/S}$. To get our ring observations into this longitude system we simply need to know the phase of the appropriate hemisphere's PPO $\Phi_{N/S}$ at the time of the observation and the angle of the observation ϕ relative to the sub-solar longitude. A ring observation's inertial longitudes $\lambda_{obs,ring}$ are measured in the prograde direction from a zero point $\lambda_{0,ring}$ relative to the ascending node of the rings on J2000. This means that all we need is the longitude of the sub-solar point in the ring longitude system $\lambda_{sun,ring}$ to then calculate $\phi = \lambda_{obs,ring} - \lambda_{sun,ring}$ needed to determine $\Psi_{N/S}$. Each ring image-movie observation captures one longitudinal region of the rings for several hours, but the ring system longitude is essentially identical. As the hours pass the images do however capture a spread of longitudes in the PPO system. This is how we are able to create Figure 4.8.

The SKR is similar to convert into the magnetometer PPO system. The SKR phases Φ_{SKR} track the location of maximum SKR emission relative to the sub-solar longitude (Ye et al., 2018). In this case we can readily substitute $\phi = \Phi_{SKR}$ and determine the SKR North or South longitude in the appropriate MAG PPO system $\Psi_{N/S}$. Because the magnetic field and SKR oscillations have essentially the same period, the SKR maximum emission is fixed at a constant offset relative to the zero point of $\Psi_{N/S}$ at any given time.

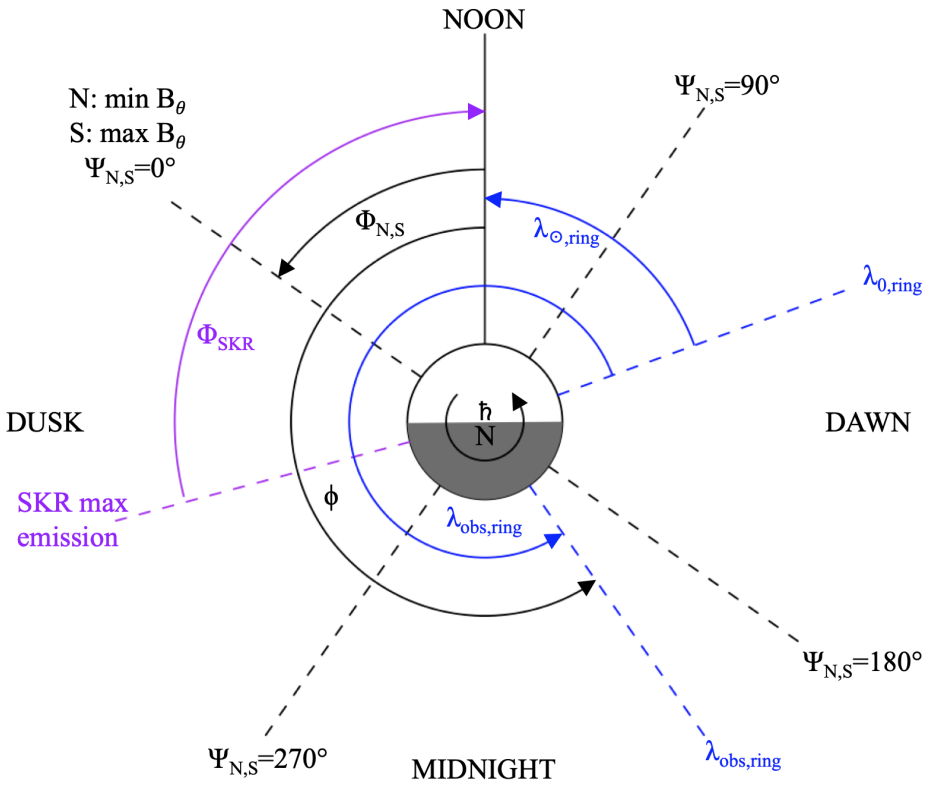

Figure F.1: A model of Saturn's PPO longitude system viewed from above the north pole, meant to enable a further understanding of Figure 4.8. The MAG PPO longitude system $\Psi_{N/S}$ is labeled in black, the ring inertial longitude system λ_{ring} relative to the ascending node of the rings on J2000 is labeled in blue, and the SKR phase Φ_{SKR} is labeled in purple. The longitude of the Sun at Saturn noon is handily used to relate the angles between the various longitude systems. In the MAG PPO longitude system $\Psi_{N/S} = 0°$ corresponds to a minimum B_θ component in the northern hemisphere, and a maximum B_θ in the southern hemisphere.

Appendix G: Roche Division Maps

Below are maps and fractional amplitude curves, equivalent to Figure 4.3 in the main text, for all imaging sequences with durations of 7 hours or longer (including Rev 237). Fits to the fractional amplitude peaks compiled in Table 4.2 are shown in their appropriate figures with dashed red lines. In some cases, we've combined observations with different exposure times into a single map (for example 029ax, 029bx, and 029cx into 029x). Note that in Figures G.9 through G.17 the SKR and MAG periods for both hemispheres fall in the A ring, well outside the radial scale shown.

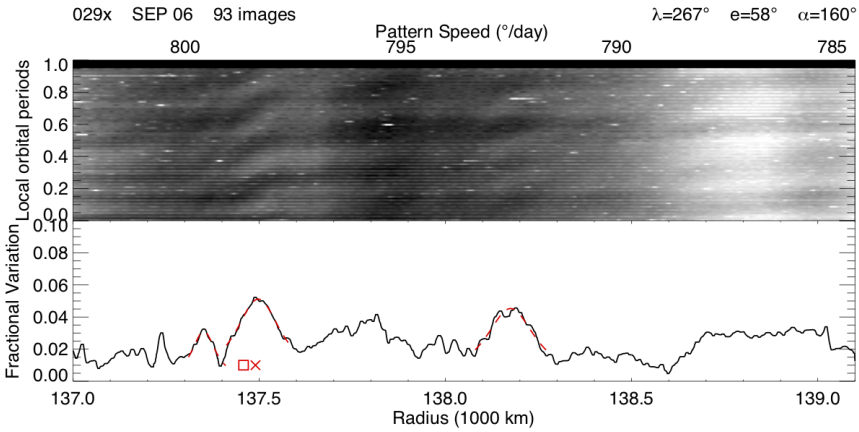

Figure G.1: Image movie 029x contains images from 029ax, 029bx, and 029cx. We've included the images' average inertial longitude λ, emission angle e, and phase angle α in the upper right corner. All fits to fractional amplitude peaks compiled in Table 4.2 are shown with dashed red lines.

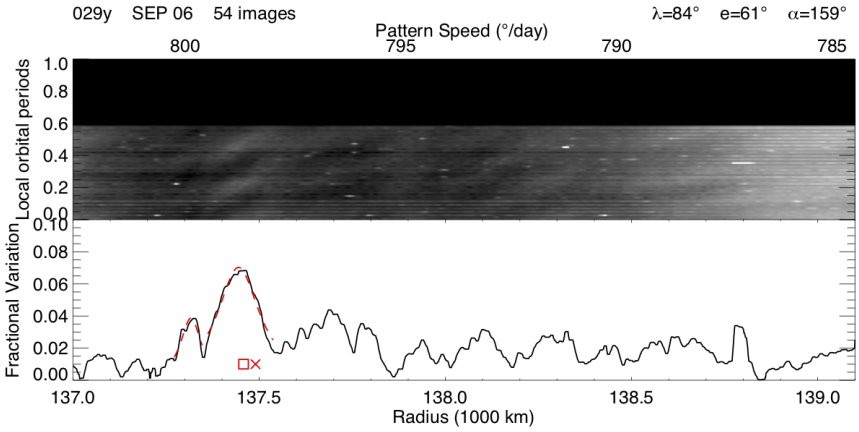

Figure G.2: Image movie 029y contains images from 029ay, 029by, and 029cy.

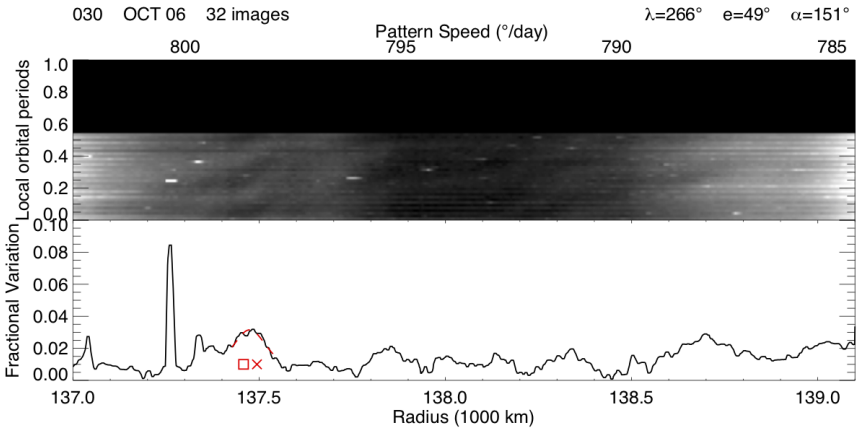

Figure G.3: Image movie 030 contains images from 030a, 030b, and 030c.

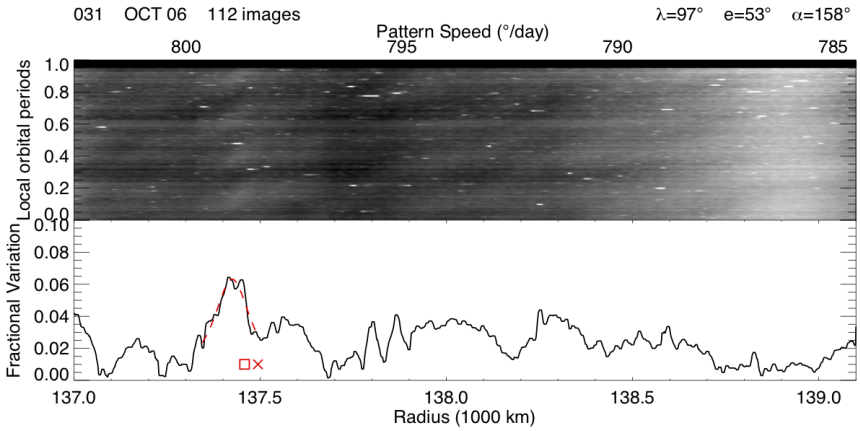

Figure G.4: Image movie 031 contains images from 031a, 031b, and 031cx.

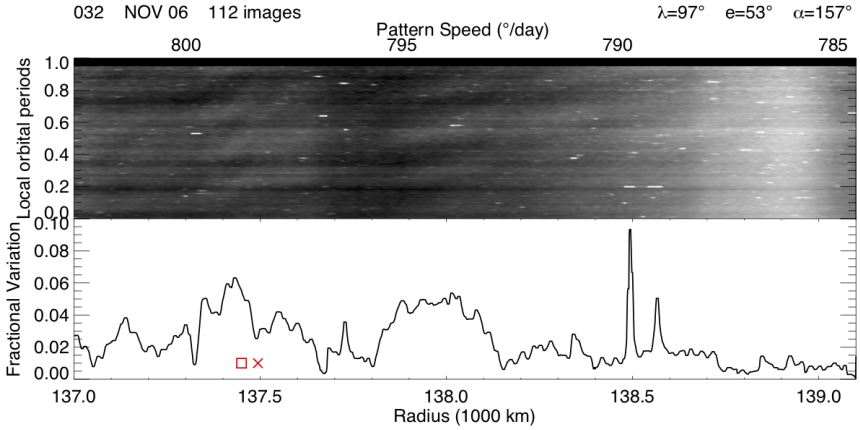

Figure G.5: Image movie 032 contains images from 032a, 032b, and 032c.

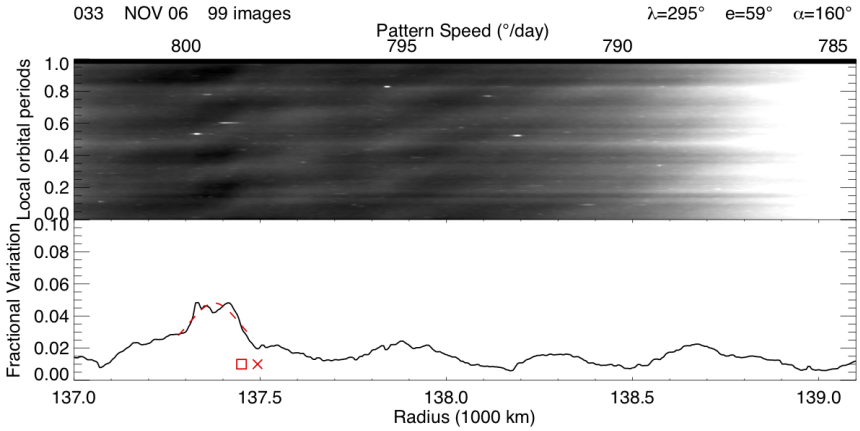

Figure G.6: Image movie 033.

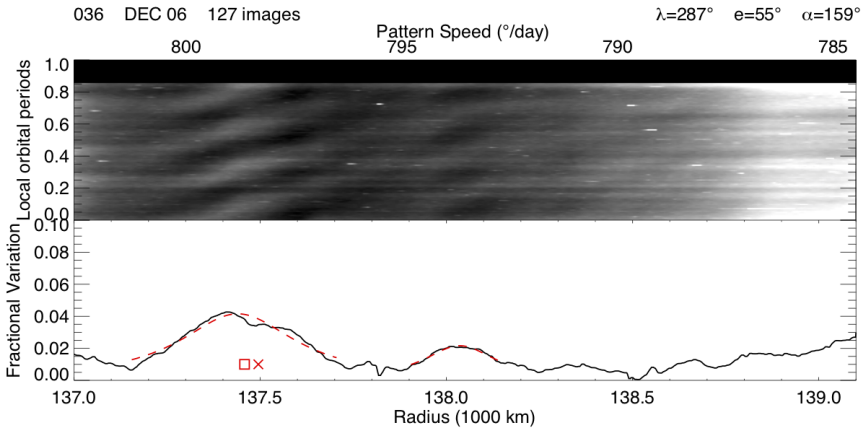

Figure G.7: Image movie 036.

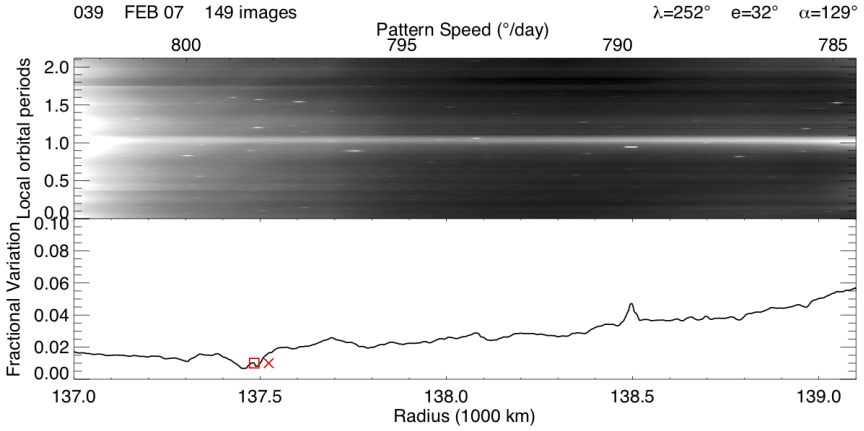

Figure G.8: Image movie 039 contains images from 039a and 039b.

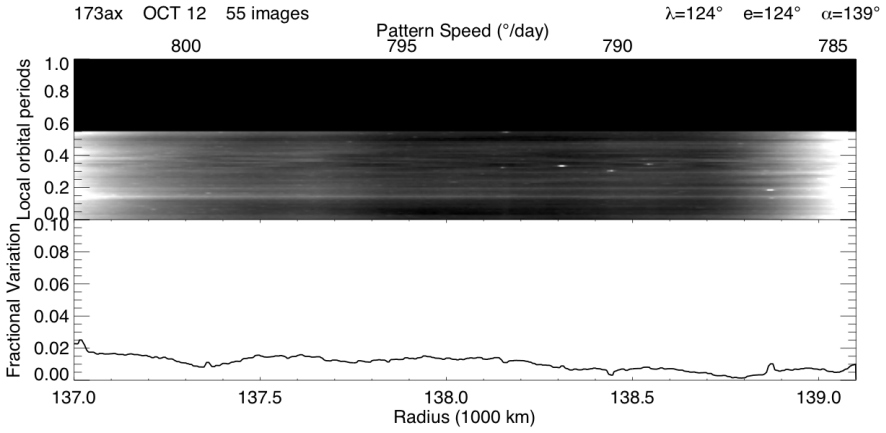

Figure G.9: Image movie 173ax.

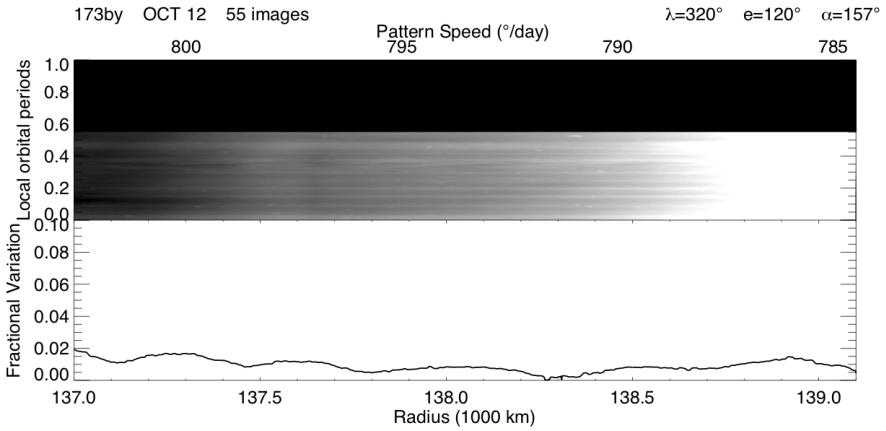

Figure G.10: Image movie 173by.

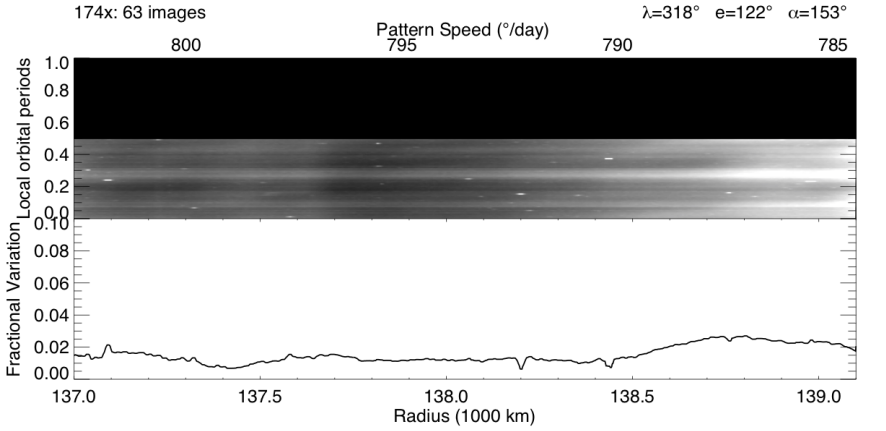

Figure G.11: Image movie 174x.

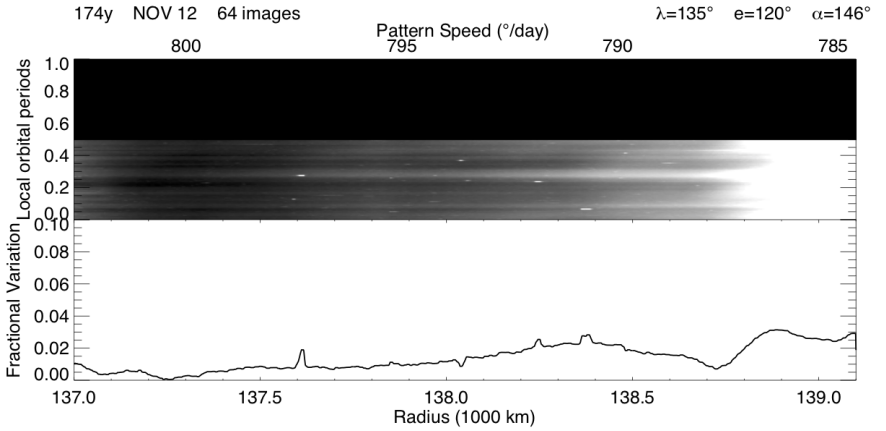

Figure G.12: Image movie 174y.

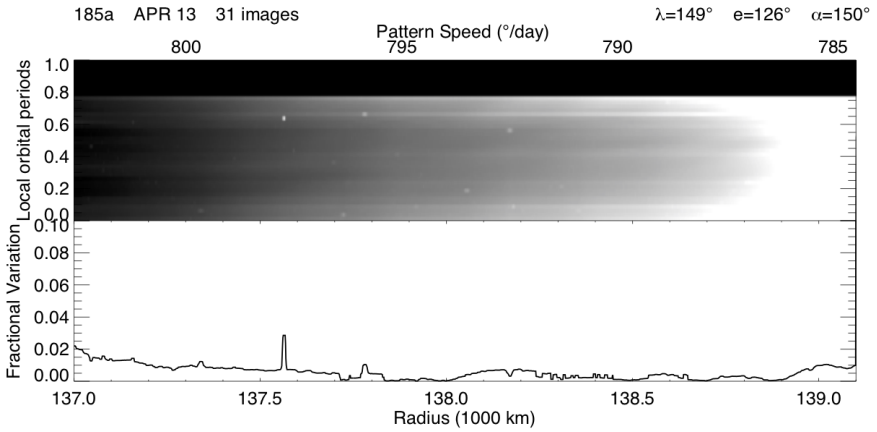

Figure G.13: Image movie 185a. Image movie 185b contains overexposed images due to an exposure time of 18 seconds.

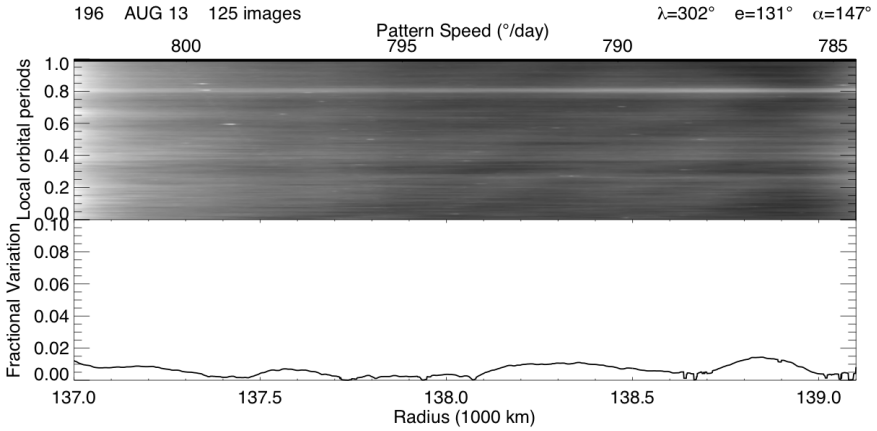

Figure G.14: Image movie 196.

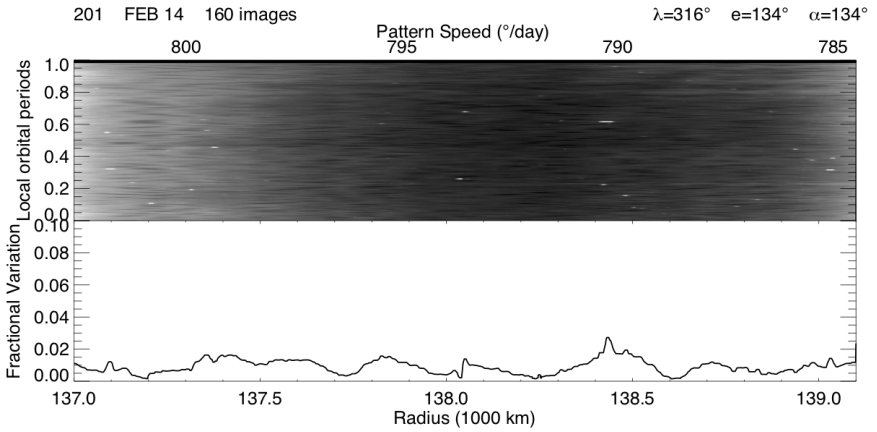

Figure G.15: Image movie 201.

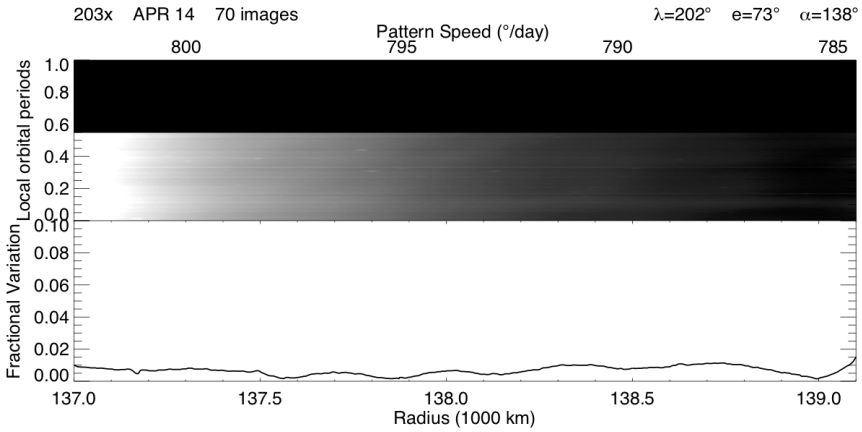

Figure G.16: Image movie 203x.

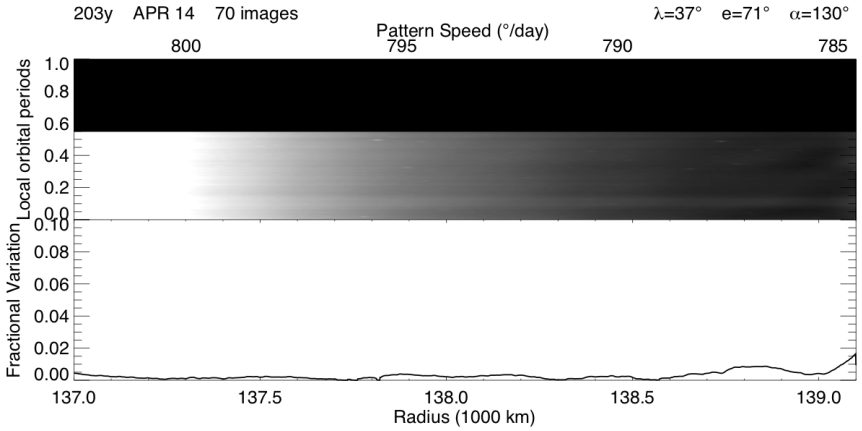

Figure G.17: Image movie 203y.

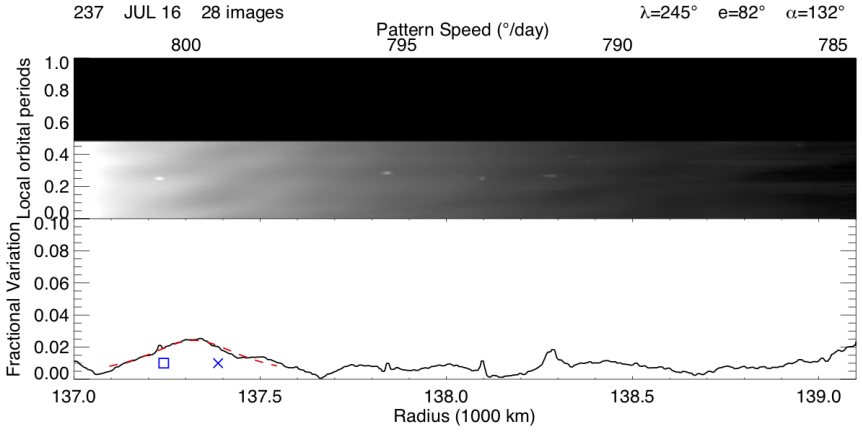

Figure G.18: Image movie 237. This movie is shorter than half an orbital period, but is included because it is the first reappearance of the 3:4 OLR structures in the Roche Division.

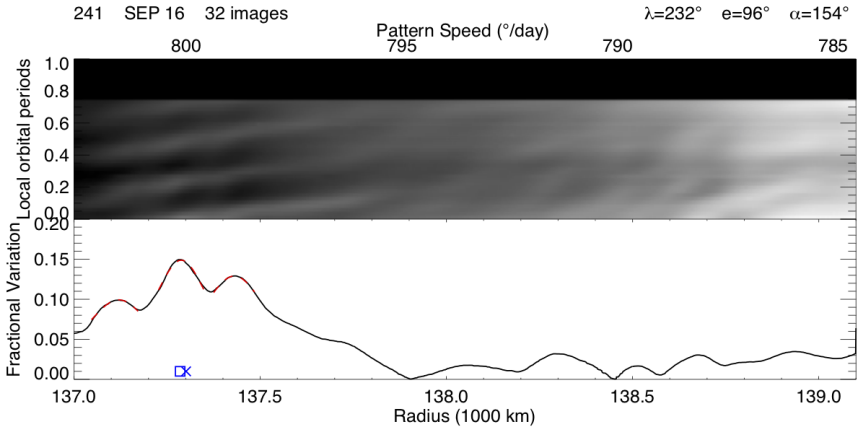

Figure G.19: Image movie 241. The scale on the fractional variation plot is increased in this plot alone. The brightness variations are substantially enhanced by the favorable lighting geometry of this observation.

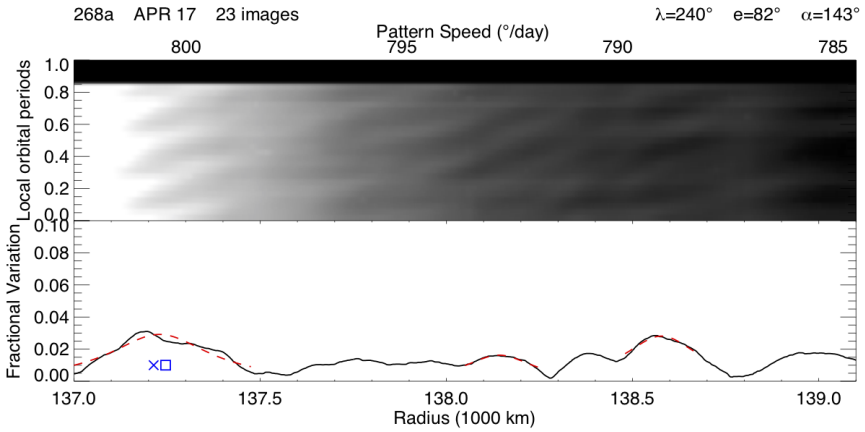

Figure G.20: Image movie 268a. Image movie 268b contains overexposed images due to an exposure time of 18 seconds.

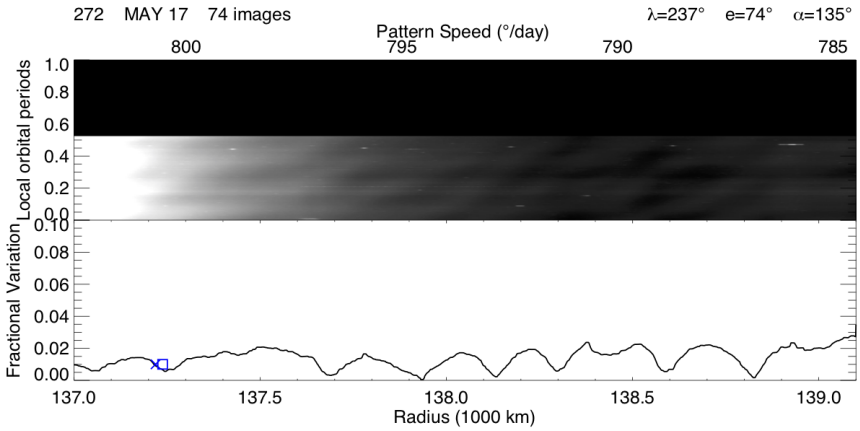

Figure G.21: Image movie 272.

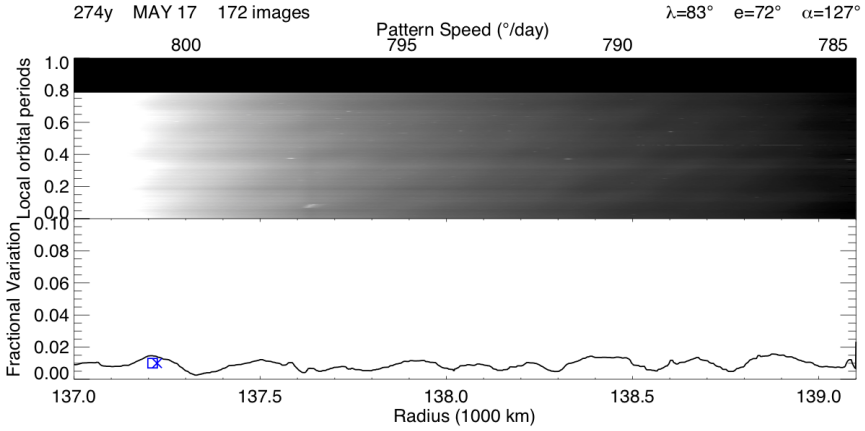

Figure G.22: Image movie 274y.

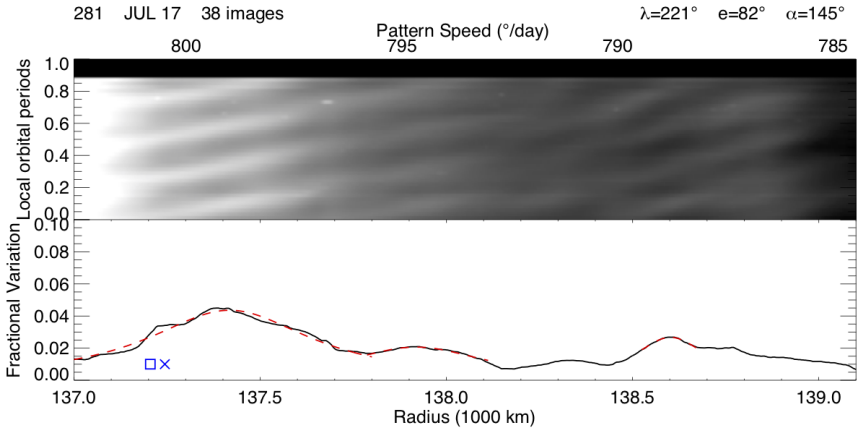

Figure G.23: Image movie 281.

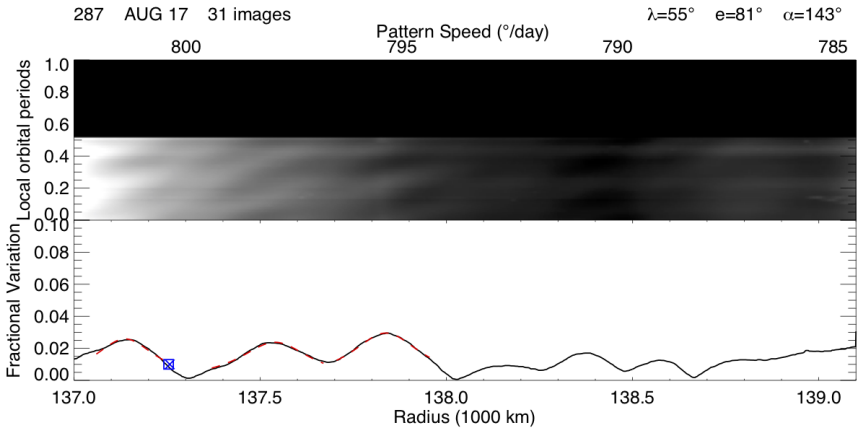

Figure G.24: Image movie 287.

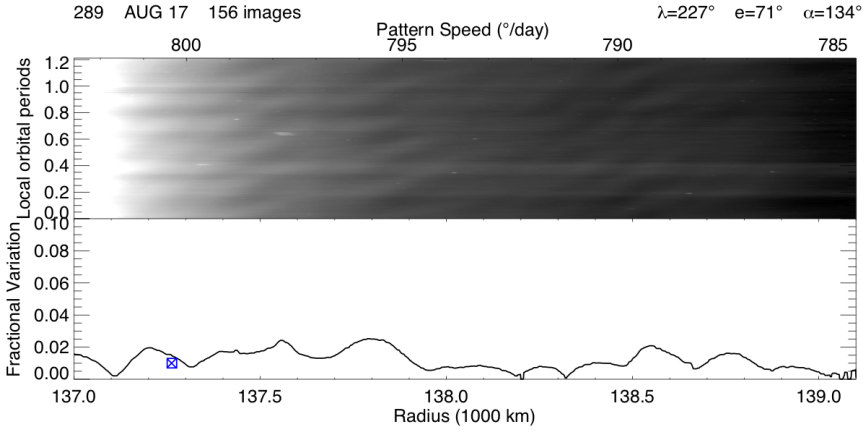

Figure G.25: Image movie 289.

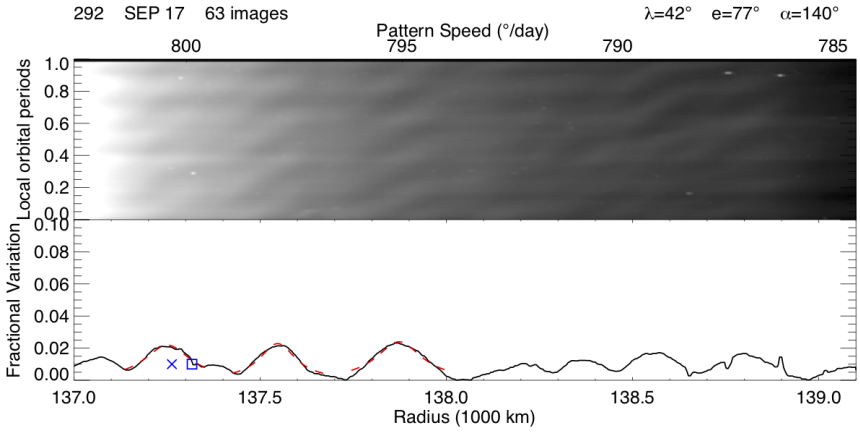

Figure G.26: Image movie 292.

Appendix H: Concerning Fourier and Wavelet Transforms

Fourier and Wavelet transforms are mathematical tools that we can use to classify the radial wavelengths of periodic variations in ring surface mass density that result from a number of gravitational interactions between the rings and moons or other perturbations. Spiral density wave structures are launched at strong Lindblad resonances in the rings and have a regular expected structure, such that they decrease in wavelength with radial distance from the exact resonance. Satellite wakes, on the other hand, are ring structures produced at much closer range and they exhibit more stable wavelengths of the ring surface mass density, changing in wavelength less rapidly with radius.

The optical depth or reflectance as a function of radius, $y(r)$, obtained from ring occultations or average brightness profiles from ring images, can be sampled for oscillating structures with nearly constant or variable wavelengths. In the case of a radial wavy structure of a moonlet wake we can effectively use a Fourier transform of the form

$$F(\lambda) = \frac{1}{r - r_1} \int_{r_1}^{r_2} (y(r) - y_{mean})\, e^{\frac{2\pi i (r - r_1)}{\lambda}} dr \tag{H.1}$$

to decompose the periodicities of a ring's radial profile with oscillations of wavelength λ in some radial window between r_1 and r_2, where y_{mean} is the mean optical depth or reflectance in the radial window. We can separate this function into its real and imaginary components using Euler's formula, where

$$F_{real} = \frac{1}{r - r_1} \int_{r_1}^{r_2} (y(r) - y_{mean}) \cos \frac{2\pi (r - r_1)}{\lambda} dr \tag{H.2}$$

and

$$F_{imaginary} = \frac{1}{r - r_1} \int_{r_1}^{r_2} (y(r) - y_{mean}) \sin \frac{2\pi (r - r_1)}{\lambda} dr, \tag{H.3}$$

to allow for easy integration of the data with an appropriate array of test case wavelengths. Finally, the absolute value of the Fourier transform can be plotted vs. wavelength

$$|F(\lambda)| = \sqrt{F_{real}^2 + F_{imaginary}^2}, \tag{H.4}$$

to reveal the wavelengths whose sinusoidal functions contribute the most to the ring's actual radial oscillations in optical depth or reflectance $y(r)$.

In Figure H.1 we plot the absolute values of three Fourier transforms covering various radial regions of an example ring radial brightness profile pictured above with marked radii. This specific data comes from a small portion of an image of the inner edge of Saturn's Encke Gap. At the edge there is a wavy structure due to the wakes leading the small moon Pan, orbiting near the center of the Encke Gap. Pan is much further from the rings here than in the case of the proposed α and β moonlets in Chapter 2. This means that the radial wavelength of the wake structure is much longer, and because the A ring is much wider than the narrow Uranian rings, the wakes span a much greater distance and slowly drift to longer radial wavelengths at greater radial distances from the Encke-gap inner edge. Also, featured in this profile is

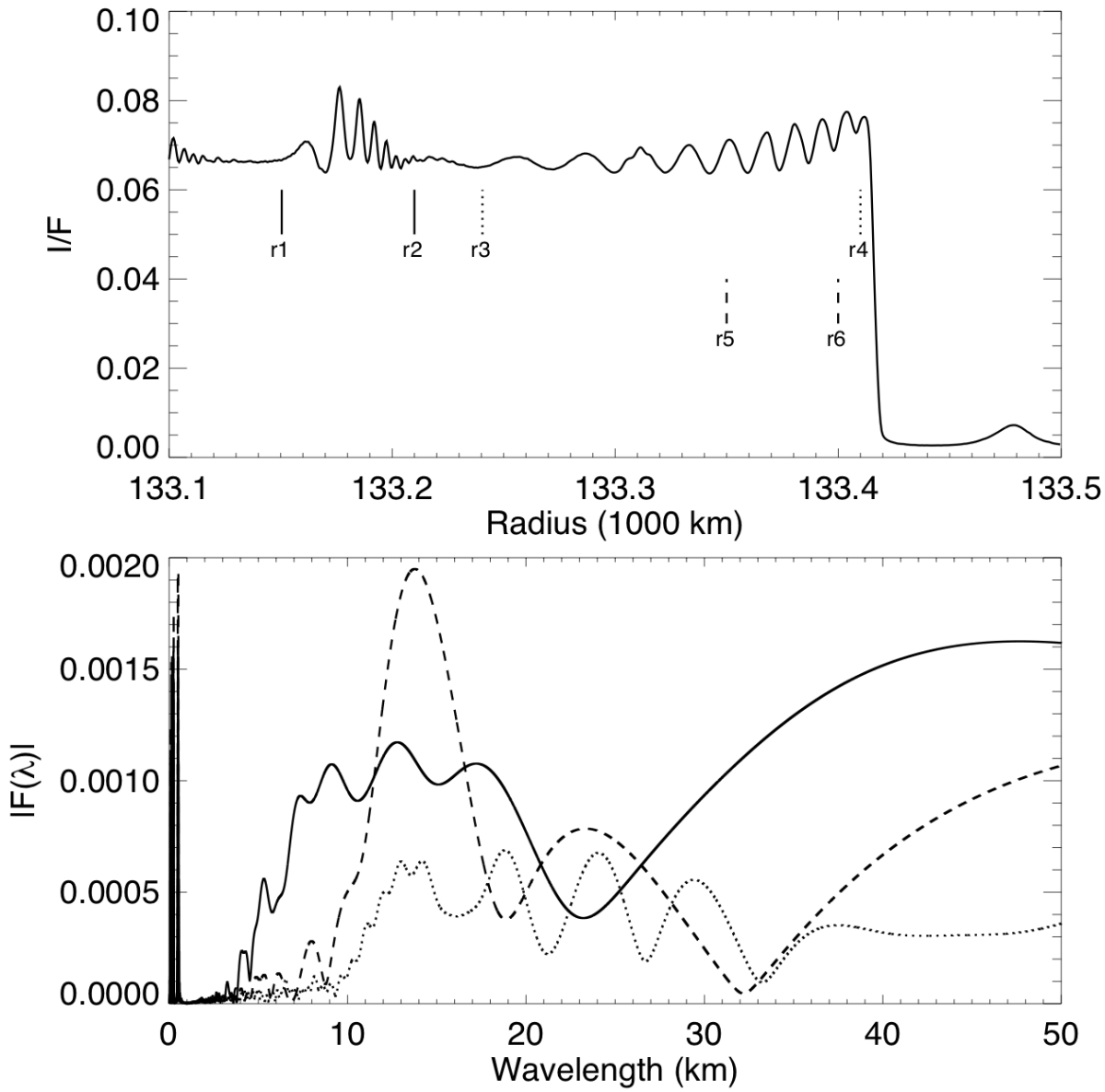

Figure H.1: The top plot is an average brightness radial profile of the inner edge of Saturn's Encke Gap, captured in an early *Cassini* image N1467351325. The profile clearly shows the radial structure of Pan's wake on the inner edge of the Gap and a spiral density wave located just interior to 133, 200 km. The radial ranged noted below the profile define the radial windows sampled in the Fourier transforms whose absolute value are displayed in the lower plot with matching line types.

the spiral density wave launched at the Prometheus 15:14 inner Lindblad resonance. Spiral density waves feature a more rapidly diminishing radial wavelength with increased distance from their resonance than a moonlet wake's gradual increase with distance from its perturbing moon. The Fourier transform below shows the relative effectiveness with which sinusoidal oscillations with a given wavelength represent the actual profile, by decomposing the data into components with different wavelengths. In both the $r_1 - r_2$ and $r_3 - r_4$ cases we see that the Fourier transform identifies a large range of wavelengths because we have sampled complete structures that have wavelengths that vary with radius. The $r_5 - r_6$ range effectively samples a narrower region with a nearly constant radial wavelength of $\sim$ 14 kilometers that is clearly identified in the Fourier transform below. Note, the peaks near 0.5 kilometers correspond to the radial resolution of the data.

We can see from Figure H.1 that Fourier transforms do not provide any information about where in the radial range sampled a particular wavelength component is most relevant unless if we narrow the range as in $r_5 - r_6$ to measure a clearly defined structure. In cases where the signal is less obvious or where the wavelength is changing significantly another tool can be particularly useful. Tiscareno et al. (2007) recently showed the effectiveness of applying Wavelet analysis to analyze these varying structures in planetary rings.

Wavelet transforms are essentially a localized Fourier transform, allowing the radii where a particular wavelength is a significant component of the input data to be located. Where a Fourier transform samples only the wavelengths of a defined radial window, a wavelet transform individually samples the same wavelengths but also with a variety of window sizes centered at each radii. This allows for the detection of both long and short wavelength structures at the same radii simultaneously and vice versa.

Wavelet analysis is performed by manipulating a mother wavelet, here we use the Morlet mother wavelet (Tiscareno et al., 2007; Torrence & Compo, 1998)

$$\psi(t) = \pi^{-1/4} \exp\left[i\omega_0 t - t^2/2\right] \tag{H.5}$$

representing a complex sinusoid with frequency, ω_0, confined within a gaussian envelope of scale 1. Manipulations of this mother wavelet yield the daughters:

$$\psi_{r,s}(r') = s^{-1/2}\pi^{-1/4} \exp\left[\frac{i\omega_0(r'-r)}{s} - \frac{(r'-r)^2}{2s^2}\right] \tag{H.6}$$

to be convolved with the input data similar to our $\exp\left[2\pi i(r - r_1)/\lambda\right]$ in the Fourier transform. Here the wavelength λ is proportional to the spatial scale s, such that

$$\lambda = \frac{4\pi s}{\omega_0 + \sqrt{2 + \omega_0}}. \tag{H.7}$$

The daughter wavelet is convolved with the input data at all radii r' in the spatial range s centered at r. Thus, if the chosen value of ω_0 is large the wavelet will have better wavelength resolution, at the expense of the radial resolution. This is because the spatial parameter s will be widened to accommodate for more cycles of the oscillations of each wavelength to fit within the gaussian envelope.

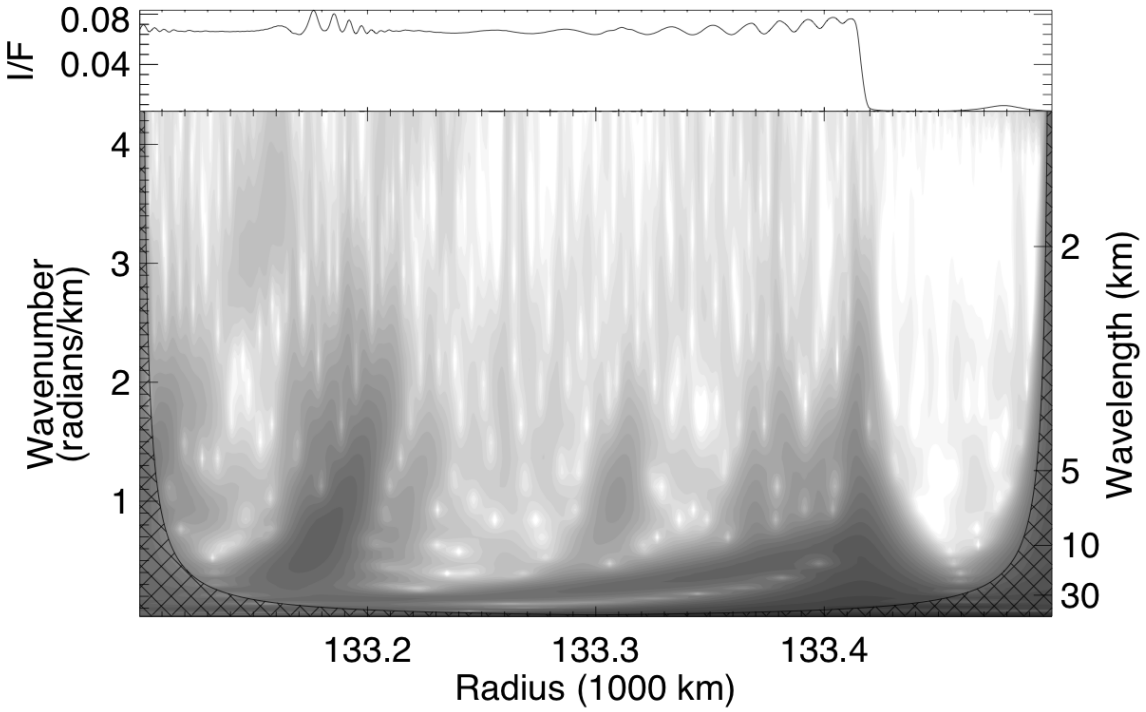

Figure H.2: The top plot is an average brightness radial profile of the inner edge of Saturn's Encke Gap as in Figure H.1, captured in an early *Cassini* image N1467351325. The lower panel shows the wavelet transform spectrum organized in wavenumber and wavelength on the left and right vertical axis respectively. The wavelet power is represented with contours, where darker regions correspond to the wavelengths at each radii that are more effective representations of the input data above.

Finally the wavelet transform itself is represented by

$$T(r,s) = \int_{-\infty}^{\infty} y(r')\psi^*_{r,s}(r')dr' \tag{H.8}$$

where * is the complex conjugate.

In Figure H.2 we plot the same radial profile as in Figure H.1 atop its wavelet transform. The dark signal shows the relative contributions of each wavelength component in the deconstructed input data at each radius. In the bottom middle portion of the spectrum, the signature of Pan's wakes drifts from a wavelength of ~ 30 km at $133,200$ km radius to less than 10 km at $133,400$ km radius. The signature of Prometheus' 15:14 inner Lindblad resonance interior to $133,200$ km shows the sharp decrease in wavelength with radius characteristic of a spiral density wave. The dark vertical band at $133,420$ km radius is commonly associated with sharp features like the edge of the Encke Gap. Many oscillating functions with different wavelengths are needed to contribute to the representation of the sharp edge, up to wavelengths less than the width of the feature itself where the dark vertical band starts to taper off. The steep feature at $\sim 133,300$ km is the weak Atlas 21:20 inner Lindblad resonance, that isn't at

all obvious in the ring profile above. The wavelet brings it immediately to our attention, but it would otherwise go unidentified unless specifically searched for using an appropriately placed narrow window Fourier transform.

Appendix I: Copyright for Published Articles

I.1 Copyright for IOP Publishing

Quoted from IOP Publishing Permissions FAQs:

Question: "May I include the Final Published Version of the article in my research thesis or dissertation?"

Answer: "Upon transfer of copyright, IOP and/or the copyright owner grants back to authors a number of rights. **These include the right to include the Final Published Version of the article in your research thesis or dissertation. Please include citation details and, for online use, a link to the Version of Record.** IOP's permission will be required for commercial use of an article published as part of your thesis. IOP does not allow ProQuest to publish or sell the article as part of your dissertation."

Credit for Chapter 2: Chancia, R.O., Hedman, M.M. 2016 "Are there moonlets near the Uranian α and β rings?" The Astronomical Journal, 152, 211, reproduced by permission of the AAS.

Credit for Chapter 3: Chancia, R.O., Hedman, M.M., French, R.G. 2017 "Weighing Uranus' moon Cressida with the η ring" The Astronomical Journal, 154, 153, reproduced by permission of the AAS.

Links to publications:
Chapter 2: `https://doi.org/10.3847/0004-6256/152/6/211`
Chapter 3: `https://doi.org/10.3847/1538-3881/aa880e`

I.2 Copyright for Elsevier

Quoted from Elsevier Copyright Permissions FAQs:

Question: "Can I include/use my article in my thesis/dissertation?"

Answer: "Yes. Authors can include their articles in full or in part in a thesis or dissertation for non-commercial purposes."

Question: "Can I use material from my Elsevier journal article within my thesis/dissertation?"

Answer: "**As an Elsevier journal author, you have the right to Include the article in a thesis or dissertation** (provided that this is not to be published commercially) whether in full or in part, subject to proper acknowledgment; see the Copyright page for more information. **No written permission from Elsevier is necessary.**"

Credit for Chapter 4: Chancia, R.O., Hedman, M.M., Cowley, S.W.H., Provan, G., Ye, S.-Y. 2019 "Seasonal structures in Saturn's dusty Roche Division correspond to periodicities of the planet's magnetosphere" Icarus, vol. 330, pp. 230-255, reproduced with permission from Elsevier.

Link to publication:
Chapter 4: https://doi.org/10.1016/j.icarus.2019.04.012